Towards Robot-aided Gait Rehabilitation and Assistance via Characterization and Estimation of Human Locomotion

by

Seyed Mostafa Rezayat Sorkhabadi

A Dissertation Presented in Partial Fulfillment
of the Requirements for the Degree
Doctor of Philosophy

Approved November 2023 by the
Graduate Supervisory Committee:

Wenlong Zhang, Chair
Spring Berman
Hyunglae Lee
Hamid Marvi
Thomas Sugar

ARIZONA STATE UNIVERSITY

December 2023

ABSTRACT

Walking and mobility are essential aspects of our daily lives, enabling us to engage in various activities. Gait disorders and impaired mobility are widespread challenges faced by older adults and people with neurological injuries, as these conditions can significantly impact their quality of life, leading to a loss of independence and an increased risk of mortality. In response to these challenges, rehabilitation, and assistive robotics have emerged as promising alternatives to conventional gait therapy, offering potential solutions that are less labor-intensive and costly. Despite numerous advances in wearable lower-limb robotics, their current applicability remains confined to laboratory settings. To expand their utility to broader gait impairments and daily living conditions, there is a pressing need for more intelligent robot controllers.

In this dissertation, these challenges are tackled from two perspectives: First, to improve the robot's understanding of human motion and intentions which is crucial for assistive robot control, a robust human locomotion estimation technique is presented, focusing on measuring trunk motion. Employing an invariant extended Kalman filtering method that takes sensor misplacement into account, improved convergence properties over the existing methods for different locomotion modes are shown. Secondly, to enhance safe and effective robot-aided gait training, this dissertation proposes to directly learn from physical therapists' demonstrations of manual gait assistance in post-stroke rehabilitation. Lower-limb kinematics of patients and assistive force applied by therapists to the patient's leg are measured using a wearable sensing system which includes a custom-made force sensing array. The collected data is then used to characterize a therapist's strategies. Preliminary analysis indicates that knee extension and weight-shifting play pivotal roles in shaping a therapist's assistance strategies, which are then incorporated into a virtual impedance

model that effectively captures high-level therapist behaviors throughout a complete training session. Furthermore, to introduce safety constraints in the design of such controllers, a safety-critical learning framework is explored through theoretical analysis and simulations. A safety filter incorporating an online iterative learning component is introduced to bring robust safety guarantees for gait robotic assistance and training, addressing challenges such as stochasticity and the absence of a known prior dynamic model.

ACKNOWLEDGMENTS

"Gratitude is not only the greatest of virtues but the parent of all others." - Marcus Tullius Cicero

First and foremost, I would like to express my deepest gratitude to my family. My mom's unwavering love, support, and sacrifices were the driving force behind the creation of this dissertation. My dad, a beacon of inspiration, instilled in me a passion for science and research, providing invaluable guidance throughout. My sisters, Nasrin and Sara infused hope and motivation into even the most challenging days.

A special acknowledgment goes to my advisor, Dr. Wenlong Zhang. Not only did he provide insightful guidance but he also offered unwavering support and understanding throughout the entire process. I extend my gratitude to Zenan Zhu and Dr. Yan Gu, our research collaborators, whose contributions were indispensable in shaping this dissertation. I also want to express my thanks to my fellow co-authors, Mason Smith, and Roozbeh Khodambashi, for sharing their insights and talents, enriching the depth of this work.

Heartfelt appreciation to all my colleagues at the Rise Lab. Each one played a unique role in my journey, and I am grateful for their contributions. A special mention to Karishma Patnaik, whose support and companionship were a constant source of strength. I owe a debt of gratitude to Shatadal Mishra, from whom I learned invaluable lessons, and to Sunny Amatya, whose presence always brightened my mood.

I would like to extend my thanks to two dear friends, Mohamad Farhadi and Ramin Moradi, and my dear cousin, Morteza, whose positive presence during this work was a significant benefit to me.

I would like to acknowledge the National Science Foundation for supporting my dissertation work through Grants IIS-1756031 and CMMI-1944833.

In the end, I would like to say that I am profoundly grateful for the invaluable experience gained along this journey. With a sense of confidence and pride, I regard this dissertation as a testament to my identity as a researcher—a person who, through intelligence and determination, exerted a modest yet earnest effort to contribute to the advancement of knowledge and techniques for the betterment of humanity. It is my hope that the fruits of scientific endeavor will one day usher in a greater sense of happiness for people.

TABLE OF CONTENTS

CHAPTER Page

CHAPTER Page

CHAPTER Page

LIST OF TABLES

LIST OF FIGURES

Figure Page

Chapter 1

INTRODUCTION

The recent surge in robotic research and applications has undoubtedly opened doors to a world characterized by enhanced convenience and comfort, thanks to cutting-edge advancements in transportation, medicine, goods, and food industries, and sustainability efforts. Notably, rehabilitation and assistive robotics have garnered significant attention due to their ability to offer invaluable assistance with everyday human tasks, facilitating the recovery and improvement of physical abilities and motor functions (Laparidou et al. 2021; Zanatta et al. 2022; Maciejasz et al. 2014). This importance becomes even more apparent when we observe the prevailing global trend of an aging population.

According to the report from the U.S. Department of Commerce, the proportion of people over 65 has increased to 7% by 2000, and will keep rising to 16% by the end of 2050 Perry 2015. Aging can lead to reduced physical performance due to muscle deterioration, and a variety of neurological diseases such as stroke and Parkinson which cause impaired mobility (Duncan et al. 2005). As a result, many people face reduced physical capabilities and have difficulties performing their daily tasks.

Walking difficulties and impaired mobility are common among older adults and can result in loss of independence and increased mortality (Brach and VanSwearingen 2013). Thus, gait training and rehabilitation are required to help individuals with gait deficits improve their physical strength and restore their lost or impaired motion control. While manual rehabilitation and gait therapy have been effective, it is costly, physically demanding, and time-consuming. Therefore it is not accessible to everyone

or at every time. This motivates the the researchers in robotic community to be actively seeking the development of wearable sensors and robots that can provide a personalized remote system for gait training and augmentation.

One way to quantify human gait is to measure lower-limb joint mobility and muscle activity during different walking activities. The overall goals for joint movements and muscle activity are to achieve weight acceptance, single-limb support, and limb advancement. During the stance phase where the foot is in touch with the ground, the weight acceptance and single limb support are the priority tasks. On the other hand, the limb advancement shifts to the top requirement during the swing phase when the foot is off the ground (Perry, Davids, et al. 1992). The wearable gait assistive robots are to augment these motion and activities, during normal walking, or to apply walking rehabilitation treatment to patients. Although their application can extend to other daily activities like ascending/descending stairs, sit-to-stand transfer, and carrying heavy loads. Exoskeletons and orthoses are defined as mechanical devices that "are worn by an operator and fit closely to the body, and work in concert with the operator's movements" (Herr 2009). In general, exoskeletons are devices that augment the performance of the able-bodied user, while orthosis is typically used to describe a device that assists a person with a limb pathology (Herr 2009).

1.1 Control of Wearable Lower-limb Robotic Devices

Figure 1.1 shows the overall control framework of wearable lower-limb robotic devices (Tucker et al. 2015).

This dissertation centers on the high-level controller and sensing aspects of wearable lower-limb robotics. The high-level controller serves as the primary decision-making

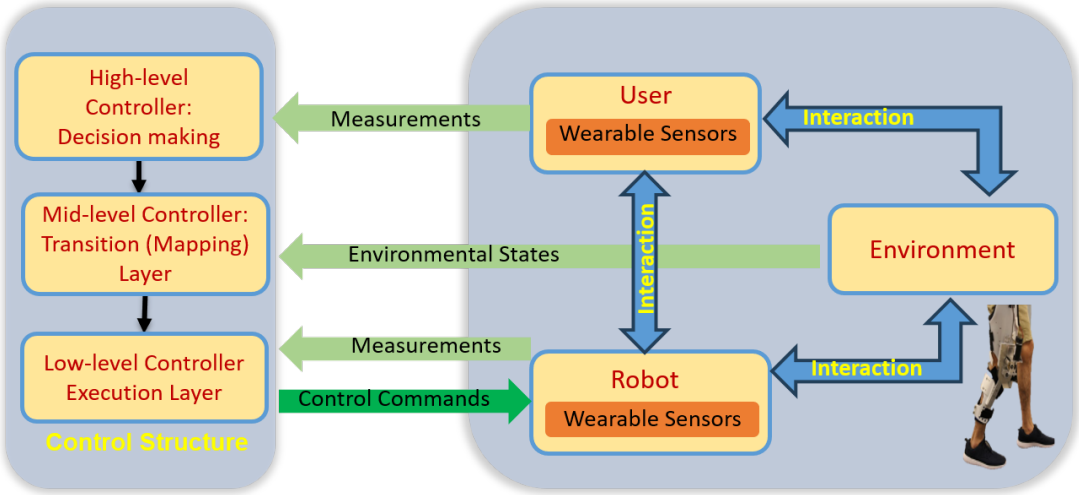

Figure 1.1. Overview of the control structure of wearable lower-limb robotic devices (Tucker et al. 2015). pHRI refers to physical human-robot interaction.

unit, receiving information from both the user and the robot through sensors that capture kinetic and kinematic states, as well as their interaction during locomotion.

In the realm of wearable lower-limb robotics, certain sensing methods are confined to controlled laboratory environments, while others, particularly wearable sensors, offer portability and adaptability for outdoor use. Various tools, including encoders, inertial sensors, and motion capture systems (Liu et al. 2011; Bamberg et al. 2008), are employed to analyze human motion. Additionally, force (Eilenberg, Geyer, and Herr 2010) and electromyography (EMG) (Rouse, Mooney, and Herr 2014) sensors are widely utilized to investigate ground reaction forces (GRFs) and muscle activities during walking.

The decision-making process generally includes two main sub-processes: 1) Intent/State Estimation, and 2) Torque/Motion planning, which will be detailed below.

1.1.1 Intent/State Estimation

It is necessary for the high-level controller to perceive the locomotion intent of the user to be able to provide proper assistance. The locomotion intents include the types of activity that the user is performing (e.g., walking, running, and stair climbing), as well as their environmental state (e.g., types of the train), which also can be categorized into the types of activity. The Locomotion intent can be estimated by knowing the user's state, which in this context refers to the pose (i.e. position and orientation) and velocity of desired limbs and body parts, as well as the status of user interaction with the robot and the environment. This information sometimes is directly provided by sensing mechanisms. However, in some cases (such as body center of mass) the critical information cannot be directly measured by sensors since it is impractical to implant sensors inside the human body. In this case, it is critical to define and estimate human states in various human-robot interactive tasks.

Activity mode recognition is generally approached via classification algorithms (Tucker et al. 2015). The periodic nature and long-term repeatability of human locomotion generate specific patterns that can be categorized into different modes. Continuous human states are often estimated by sensor fusion and regression models for improved accuracy. Such states that are of interest include the stance-foot position in the world, which can be used to represent a locomotor's global position in an environment(Ojeda and Borenstein 2007). The pose and velocity of the body (e.g., pelvis or chest) are also of particular interest in gait analysis and wearable robot controller design because they can be used to study postural balance and gait stability(Deane et al. 2021).

1.1.2 Motion/Torque Planning

Besides the locomotion intent of the user, the motion or torque planning strategy of robotic assistive exoskeletons and devices also depends on the specific and personalized gait impairment that needs to be addressed. Different assistive and rehabilitative strategies have been developed for different types of gait pathology and the level of impairment (Rodrıguez-Fernández, Lobo-Prat, and Font-Llagunes 2021). Phased-based and non-phased controllers (Tucker et al. 2015) have been proposed. In the Phased-based approach, the assistance is defined based on the gait phase. In this context, FSM-based controllers have been among the most popular ones (Rodrıguez-Fernández, Lobo-Prat, and Font-Llagunes 2021; Tucker et al. 2015), in which the level of assistance is defined based on discrete gait events. Motion planning controllers have been developed to reinforce healthy gait patterns for the users. However, these methods face several shortcomings such as sensitivity to disturbances, and not accommodating the variability in human gait trajectories. Impedance control, on the other hand, has received major attention in this field. Impedance controllers provide a level of compliance by mapping the motion errors to the torque output through virtual stiffness, damping, and inertia parameters. Therefore they can work with ill-defined reference trajectories.

1.2 Research Objectives and Contributions

The primary objective of this dissertation is to employ innovative methodologies encompassing state estimation, non-linear control methods, gait biomechanics, statistical optimization, and machine learning, to make significant contributions towards

the advancement of personalized and intelligent assistive and rehabilitation strategies. These advancements are crucial in progressing toward the practical implementation of wearable lower-limb assistive robots in clinical settings. The central focus lies in the development of intelligent robot controllers that facilitate efficient interaction and seamless coordination between the user and the robotic system. By integrating these sophisticated techniques, the dissertation seeks to pave the way for more effective and user-centric applications of assistive robotics in the field of lower-limb assistance and rehabilitation.

To achieve the stated objectives, a dual-pronged approach has been pursued. Firstly, the focus has been on comprehending essential pieces of information that are critical for the health monitoring and control of assistive robots. In one study we proposed a method for classifying human walking speed and slope using sEMG (surface electromyography) sensors and K-means clustering. Remarkably, this classification method achieved high accuracy in distinguishing different walking speeds and slopes, contributing to more precise and efficient human-robot interaction. Another work focused on estimating variables that cannot be directly or accurately measured using wearable sensors. A robust human locomotion estimation technique was introduced, which incorporates an invariant extended Kalman filtering method. This approach enables accurate tracking of human pose and velocity while accommodating sensor misplacement, resulting in improved convergence properties compared to existing methods for different types of human locomotion.

In the other aspect of this dissertation, the focus is put on designing high-level controllers for robotic exoskeletons, emphasizing their applications in assistance and rehabilitation. We explored the possibilities of integrating knowledge from conventional gait therapy into the development of robot controllers. To achieve this, a custom-made

wearable system, capable of measuring the interaction dynamics between physical therapists and patients during manual gait training sessions, is developed. Inspired by conventional rehabilitation methods, we devised a virtual impedance learning framework to model this therapist-patient interaction. The resulting model successfully captured and replicated the high-level behaviors of physical therapists throughout an entire training session. This contributes to a novel approach for controlling wearable robotics, as it directly encodes the decision-making process of physical therapists into a human-robot interaction framework.

The contribution of this thesis is summarized as follows:

- As a preliminary work, a robust classification approach with only two features derived from EMG signals is developed to recognize locomotion activities and detect changing speeds
- A new invariant extended Kalman filter design is developed that produces real-time and rapid error convergence for the estimation of the human body movement even in the presence of sensor misalignment and initial state estimation errors.
- A novel and custom-made wearable data collection system is developed to collect physical interaction dynamics and leg kinematics between the physical therapist and the post-stroke patient, during the gait training session. Patient impairment and PT assistance are characterized and were employed to develop a patient-specific LfD-based impedance model for gait robotic rehabilitation.
- A safety filter is designed for application in robotic gait assistance, to provide safety for LfD-based controller. It offers robust safety guarantees, addressing challenges such as stochasticity and the absence of a known prior dynamic model. The online iterative learning component ensures finding less conser-

vative controllers at each iteration and the performance is evaluated through simulations.

1.3 Outline

In Chapter 2, we discussed the prior and related work on human locomotion activity and motion estimation, as well as rehabilitation and assistive strategies for robot-aided gait training and assistance. Chapter 3 introduces a novel approach to using muscle activity for human locomotion activity and speed detection. In chapter 4 we present the InEKF design for estimating human motion during squat motion incorporating sensor imperfect placement. Chapter 5 discusses the importance of capturing human-human sensorimotor interaction during gait training, and presents an analysis and modeling of patient-therapist interaction that was collected using a custom-made wearable sensor system. Chapter 6 discusses a safety-critical framework for regulating nominal controllers to provide safety for human-robot interaction in gait applications. Chapter 7 concludes the thesis and points out possible future research directions that can be explored.

Chapter 2

RELATED WORK

2.1 Gait Intent and State Estimation

2.1.1 Activity Mode recognition

Activity mode recognition is generally approached via classification algorithms (Tucker et al. 2015). The periodic nature and long-term repeatability of human locomotion generate specific patterns that can be categorized into different modes. Heuristic rule-based classifiers such as finite state machine (FSM) (Sup, Varol, and Goldfarb 2010; Goršič et al. 2014; Kong and Tomizuka 2009) and decision trees (Jin et al. 2006; Li and Hsiao-Wecksler 2013) are effective classifiers in which the classification is based on rules that are defined manually or analytically based on sensed states. Automated pattern recognition (Tucker et al. 2015) on the other hand, uses generated decision-making boundaries by machine learning and statistical algorithms. These boundaries are usually generated during the training by inputting high-dimensional data from the user and its interaction with the robot and the environment. Such classifiers include Gaussian mixture models (GMM) (Kilicarslan et al. 2013), support vector machines (SVM) (Huang, Kuiken, Lipschutz, et al. 2009), and artificial neural network (ANN) (Gancet et al. 2011).

2.1.2 Activity Mode Recognition using Muscle Activity

EMG signals contain important information about muscle activities, and thereby, will be helpful in estimating human intentions. Multiple methods have been proposed to extract useful information from EMG signals to control assistive devices (Young and Ferris 2017). In hybrid assistive limb (HAL), a voluntary control strategy is developed to estimate the user's intentions based on the detection of muscle activities through EMG signals (Lee and Sankai 2002). In (Karavas et al. 2015), an intention estimation algorithm based on EMG signals was integrated into the high-level controller strategy of the knee exoskeleton. Although the aforementioned assistive devices exhibited fair performance in terms of providing appropriate assistance using EMG signals, there are certain limitations associated with a number of EMG sensors, types of locomotion activities, and generalization of the approach. Many human activity recognition (HAR) methods were proposed in the literature based on the features extracted from EMG signals (Xi et al. 2017). Some employed eight EMG sensors around the thigh and adopted a convolutional neural network (CNN) to perform walking activity classification (Md Alias et al. 2018). The combination of linear discriminant analysis (LDA) and a two-layered artificial neural network (ANN), was used to identify the locomotion activities with twelve EMG sensors (Huang, Kuiken, Lipschutz, et al. 2009). Finite state machines using EMG signals from six muscles were able to recognize level-walking, ramp ascent, and ramp descent (Islam and Hsiao-Wecksler 2016). There is a need to develop a human activity recognition algorithm with a minimal number of EMG sensors and to extract a smaller number of features to make the algorithm real-time and easily integrable to the assistive device.

The time domain and frequency domain features are the most commonly extracted

features from the time windows of EMG signals (Xi et al. 2017). Using sliding time window has been proven to be more robust compared to the fixed time window (Merlo, Farina, and Merletti 2003). The time domain features such as mean absolute value (MAV), root mean square (RMS), integrated EMG (iEMG), and zero crossing (ZC) are used in supervised learning (Ziegier, Gattringer, and Mueller 2018). Although time domain features are easy to compute, they yield less classification accuracy. However, RMS and MAV are proven to be intuitive in the classification of locomotion activities. Others used frequency domain features such as mean frequency (MF) and median frequency (MDF) (Joshi, Nakamura, and Hahn 2015). Some performed wavelet decomposition of the EMG signals to extract wavelet features to train the algorithm (Ivanenko, Poppele, and Lacquaniti 2004). The frequency and wavelet features generally require more computational effort than time domain features.

2.1.3 Human Motion Estimation

Continuous human states are often estimated by sensor fusion and regression models for improved accuracy. For example, a Gaussian process regression model was used to estimate human walking speeds based on wrist-worn IMUs (Zihajehzadeh and Park 2016). Real-time estimation of continuous human movement states has been extensively studied for common daily activities such as walking and squatting. One variable of particular interest in continuous state estimation is a person's stance-foot position in the world, which can be used to represent a locomotor's global position in an environment (Ojeda and Borenstein 2007). With an IMU attached to each toe, the dead reckoning method [12] obtains the toe velocity by integrating the accelerometer reading and removes the accumulated velocity errors due to the integration by resetting

the velocity to zero when the toe is static on the ground. The dead reckoning method has been applied to achieve real-time human localization (Van Nguyen and La 2016), and extended to further improve its accuracy through smoothing (Ruiz et al. 2011) or filtering (Ruiz et al. 2011).

Besides the stance-foot location, the pose (position and orientation) and velocity of the body (e.g., pelvis or chest) are also of particular interest in gait analysis and wearable robot controller design, because they can be used to study postural balance and gait stability (Deane et al. 2021). Body pose and velocity have been estimated through the nonlinear forward kinematics between the stance foot, which is obtained through accurate initialization and contact detection, and the body frame (Yuan and Chen 2013). This method assumes the leg kinematics is precisely known, and thus has been extended based on Kalman filtering (KF) to explicitly address uncertainties such as sensor noises (Yuan and Chen 2014). Recently, extended Kalman filtering (EKF) has been applied to further address the inaccuracy of the nonlinear kinematics chain, in addition to sensor imperfections, for real-time movement estimation under small initial estimation errors (Zhang, Chen, and Yi 2013; Y. Zhang et al. 2015). Yet, conventional EKF suffers a major weakness in that its design relies on the linearization of process and measurement models at the state estimates instead of the true states. Due to this weakness, the EKF cannot guarantee error convergence in the presence of large estimation errors.

Recently, invariant extended Kalman filtering (InEKF) has been introduced to ensure real-time, provable error convergence even in the presence of large initial estimation errors (Barrau and Bonnabel 2016). The InEKF exploits nonlinear state estimation errors that are invariant on the matrix Lie group and ensures that the dynamics of the logarithmic error are exactly linear and independent from the state

estimate if the process model meets the group affine condition and if the measurement model is in the invariant form. The filtering method has been applied to solve the real-time state estimation problem for aircraft (Barrau and Bonnabel 2016), legged robots (Hartley et al. 2019; Lin et al. 2021; Gao, Yuan, and Gu, 2021 (in press); Teng, Mueller, and Sreenath 2021), and underwater vehicles (Potokar, Norman, and Mangelson 2021).

While the InEKF method (Hartley et al. 2019) has achieved impressive estimation performance for robot locomotion, it has not been applied to solve some of the key challenges in the state estimation of continuous human movement state, such as the inaccurate kinematic parameters and imperfect sensor placement. One common solution to imperfect sensor placement is manual sensor calibration (Yuan and Chen 2013), which is often time-consuming and thus may not be suitable for real-world applications (e.g., daily movement monitoring) that could demand frequent re-calibration.

2.2 Gait Training Strategies for Wearable Lower-Limb Assistive Robots

Different assistive and rehabilitative strategies have been developed for different types of gait pathology and the level of impairment (Rodrıguez-Fernández, Lobo-Prat, and Font-Llagunes 2021). Phased-based and non-phased controllers (Tucker et al. 2015) have been proposed. In the Phased-based approach, the assistance is defined based on the gait phase. In this context, FSM-based controllers have been among the most popular ones (Rodrıguez-Fernández, Lobo-Prat, and Font-Llagunes 2021; Tucker et al. 2015), in which the level of assistance is defined based on discrete gait events. The impedance control framework has been proposed as a good solution due to the robust, low-gain, and compliant behavior (Buchli et al. 2011) that is

necessary for tightly coupled Human-Robot Interaction (HRI) scenarios. In contrast to traditional approaches that reject disturbances, impedance control accommodates them by defining the robot's force behavior as a spring-damper system (Khan et al. 2019). The stiffness and dampening are dynamically changed according to varying time-dependent stiffness and damping gains. One way of defining these gains is to learn them from human observations using a learning-from-demonstration (LfD) approach. Impedance control has generally been shown to be more effective than traditional control approaches like motion control, force control and hybrid position-force control (Marchal-Crespo and Reinkensmeyer 2009).

2.2.1 Robot-Aided Therapy using Human-Human Haptic Interaction

Despite considerable progress in sensor and robot-aided gait rehabilitation, the lack of intelligent control approaches prevents assistive robots from clinical deployment. Previous studies have suggested that modeling and identifying human-human sensorimotor interactions have led to the development of robots that physically interact and move with humans in an intuitive and efficient manner (Sawers and Ting 2014). Physical rehabilitation is a form of Human-Human haptic interaction in which the goal of PT is to train the patient to improve their motor performance. However, in the context of rehabilitation robotics, there is no widely accepted framework to define Human-Human interaction (HHI) (Sawers and Ting 2014). This is mainly because of the lack of enough studies that have collected and modeled the haptic interactions between PTs and patients to reveal how those forces should be applied to encourage motor skill learning.

There are limited studies in which the haptic interaction between the PT and

patients has been collected and used for learning HRI strategies, especially for gait training. Gal et. al (Galvez et al. 2005) collected the interaction force and leg kinematics during body-weight supported treadmill training for people with spinal cord injury, and showed that different PTs applied significantly different forces, resulting in different leg kinematics. However, no specific strategy on how the forces contributed to the task performance or modeling of the assistance, was proposed.

Fong et. al. (Fong, Rouhani, and Tavakoli 2019) targeted foot-dropping assistance during treadmill-based gait therapy and proposed an impedance-based LfD framework to implement that on a robotic arm. Despite the successful modeling and implementation, the experimental scenario did not include actual patients and PTs, and the haptic interaction did not resemble actual PT-patient interaction, therefore no insights for HRI could be extracted.

Chapter 3

PRELIMINARY WORK

This chapter presents a preliminary study by the author on using wearable sensors for locomotion activity mode detection and studying contextual and personalized factors on elderly gait patterns.

3.1 Human Locomotion Activity and Speed Recognition Using Electromyography Based Features

Human locomotion recognition methods based on electromyography (EMG) signals have not shown robust and accurate classification performance. This is due to the limitations of EMG signals such as their stochastic nature and sensitivity to placement of the sensors, as well as the number of sensors, feature extraction, and classification algorithms. In this work, a robust classification approach with only two features derived from EMG signals is developed to recognize locomotion activities and detect changing speeds. The root means square (RMS) and energy of the EMG signals are the features adopted in this method. The energy of the EMG signal is extracted using the energy kernel method. The proposed approach uses a low number of sensors and features, online unsupervised classification, and is generalizable to different lower-limb muscle groups.

3.1.1 Approach

The RMS and energy of the EMG signal are the two features proposed to perform the classification of locomotion speed and activities. The RMS of the EMG signal is attributed to the muscle force (Christie et al. 2009). The energy of the EMG signal is derived using the energy kernel method given in (Chen, Zeng, and Yin 2017). The energy kernel method is based on the assumption that the EMG signal governs a harmonic oscillator model. There is a physical intuition between energy and force/power of muscle explained in (Chen, Zeng, and Yin 2017). In this work, we hypothesize that the change in energy of the EMG signal per gait cycle with locomotion speed or activity follows the damped harmonic oscillator model. Therefore we should be able to classify different activities based on their energy level. In (Chen, Yin, and Fan 2014) it is suggested that the energy kernel method combines the advantages of both RMS and mean power frequency methods and provides better Physical intuition of EMG However, regarding the uncertainties associated with EMG signal, we believe that using the RMS and energy of EMG signal as two features for identifying the gait speed or activity change would lead to more accurate and robust prediction than using individually, and can be expanded to broader applications.

3.1.1.1 Damped Harmonic Oscillator Model of EMG

This model is inspired by the simple harmonic oscillator model of the EMG given in (Chen, Zeng, and Yin 2017). The behavior of the EMG signal can be recognized as an oscillator whose amplitude is featured by the reciprocating motions accompanied by

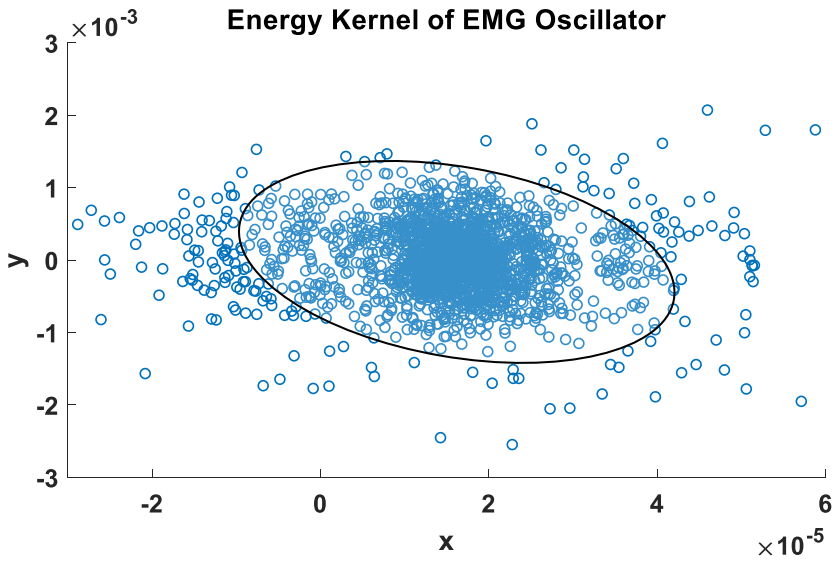

Figure 3.1. The energy kernel of the EMG signal of vastus laterialis

a noise, as it is a zero-averaged stochastic wave signal. The energy of simple harmonic oscillator with mass m, stiffness k is given as:

$$E_0 = \frac{1}{2}kx^2 + \frac{1}{2}my^2 \tag{3.1}$$

or in an elliptic form as:

$$\frac{x^2}{2E_0/k} + \frac{y^2}{2E_0/m} = 1 \tag{3.2}$$

The phase portrait of EMG signal of Vastus Laterialis (amplitude signal on x and derivative of the amplitude on y) for a segment is shown in Fig. 3.1. The length of the time window chosen for this portrait is equal to one gait cycle. Gait cycle events are obtained from force plate data.

This elliptic shape of the phase portrait given by (3.2), can be seen in Fig. 3.1 for the EMG signal per gait cycle. It is not possible to compute E_0 directly as k and m are unknown. However, the area of the ellipse will be useful in calculating the energy

of the harmonic oscillator. The area of the ellipse can be expressed as

$$S = \frac{2\pi}{\sqrt{km}}E \tag{3.3}$$

Equation (3.3) shows that the area of the ellipse is proportional to the energy of the harmonic oscillator. The ellipse of the phase portrait is referred to as the energy kernel (Chen, Zeng, and Yin 2017).

It is expected that during gait or any periodic locomotion activity, the energy of EMG per cycle, which is a representation of muscle activity, will stay at the same level, and will change when the activity changes. This change can be modeled by the harmonic damped oscillator. The energy of a damped harmonic oscillator with damping b is given as:

$$E = E_0 e^{-\frac{bt}{m}} \tag{3.4}$$

Here t is time, and E and E_0 are the energy of the damped harmonic oscillator and simple harmonic oscillator, respectively. The smaller value of b in (3.4) makes E to be approximated as E_0, the energy of the simple harmonic oscillator. We hypothesize that at a constant speed of a locomotion activity, the damping of the muscles exhibits a small value. Therefore, it can be approximated as a simple harmonic oscillator. However, the change in locomotion speed and activity will change the damping value to a higher positive or negative value causing decay or an increase in the muscular energy governed by the damped harmonic oscillator model. We want to validate this model in the experiments with locomotion speed or activity change and use the result to detect those changes.

3.1.2 Methods

To initially evaluate the generalization and performance of this method, it has been tested on a public dataset on which EMG data of participants are collected as they were walking on the treadmill in different slopes and speeds. Furthermore, an additional set of experiments and data collection are done, to evaluate the performance of this method on: 1) clustering if the walking speed changes online and 2) different muscle groups around the knee joint. The latter will examine the generalization of the proposed method to other muscle groups.

Public Data Set: The chosen dataset contains leg joint kinematics, kinetics, and EMG activity of able-bodied subjects walking on an instrumented treadmill in different combinations of slopes (-10 degrees to +10 degrees) and speeds (0.8 m/s to 1.2 m/s) in each trial. The study was done at the University of Texas at Dallas (Embry et al. 2018).

Among all the trials, four trials of five subjects have been considered for speed and activity change detection: level and uphill walking at speeds 0.8 and 1.2 m/s. Each trial contains EMG data of four muscle groups: rectus femoris (RF), biceps femoris (BF), tibialis anterior (TA), and gastrocnemius (GC). The EMG signals were collected with a sampling rate of 2000 Hz, and rectified and low-pass filtered (fc=40 Hz) with a zero-phase digital filter. The EMG data are broken down into individual gait cycles which begin and end at heel strikes. Each gait cycle contains 150 EMG data points which are used to extract the proposed features for each stride. As some issues with right-leg EMG sensors have been reported in this study, left-leg EMG sensors are chosen for all subjects.

Data Collection and Pre-processing: Two level walking experiments were

Table 3.1. Details of the healthy participants who joined the study.

ID	Gender	Age	Height (cm)	Weight (kg)
1	Male	21	175	94
2	Male	20	176	78

performed on two participants, as the treadmill speed changed online, and their EMG data were collected. For the vastus lateralis (VL) and vastus medialis (VM), one surface EMG (sEMG) wireless sensor (Delsys Trigno Avanti) were placed on each muscle group based on Seniam placement protocol (Hermens and Freriks 1997). The vastus lateralis sEMG was placed two-thirds along the line between the anterior spina iliaca superior to the lateral side of the patella, in the direction of the muscle fibers. The vastus medialis electrode was placed 80% along the line from the anterior spina iliaca superior to the joint space in front of the anterior border of the medial ligament, oriented perpendicularly to the line.

The sampling rate for both sEMG was 2000 Hz. The sensor's placement is shown in Fig. 3.2. This study has been done at Arizona State University (ASU) and has been approved by its Institutional Review Board (IRB).

Each participant walked on an instrumented dual belt treadmill with integrated force plates. Along with the EMG data, force plates data were collected to detect heel strike events. The collected raw EMG data were rectified and processed using a 4th-order Butterworth filter with a cut-off frequency of 40 Hz. The data were broken down into individual cycles based on heel strike events detected by the force plates.

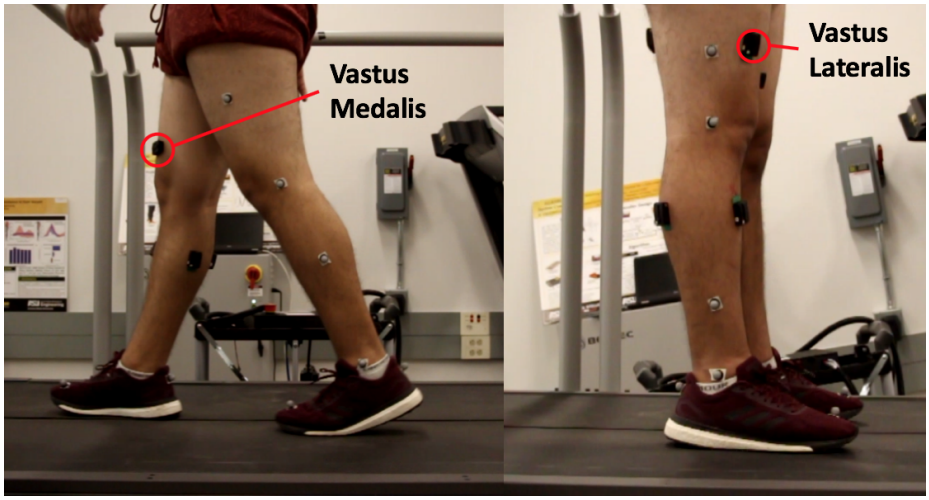

Figure 3.2. The sensor placement for EMG signal acquisition of VL and VM muscle groups during the speed change trials

3.1.3 Feature Extraction

The RMS and energy feature of EMG were calculated per gait cycle, from the collected and processed EMG for all trials. For a given number of data points, the RMS of the signal will be:

$$RMS = \sqrt{\frac{1}{n}\Sigma_{i=1}^{n} x_i^2} \tag{3.5}$$

where x represents the signal over the cycle and n is the number of data points within the cycle. The energy of the EMG signal at each gait cycle would be the area of the ellipsoid which was represented in section II. To calculate the area, the phase portrait of each cycle was extracted by taking the x as the amplitude of the signal and y as its derivative. A discrete box-counting method proposed in (Chen, Zeng, and Yin 2017) has been used to calculate the ellipsoid of the phase portrait. This method divides the rectangle enclosing all the data points of phase portrait in $n_1 \times n_2$ grids or boxes. The number of points inside each box (p_{ij}) will be counted, and if $p_{ij} > thr$, where

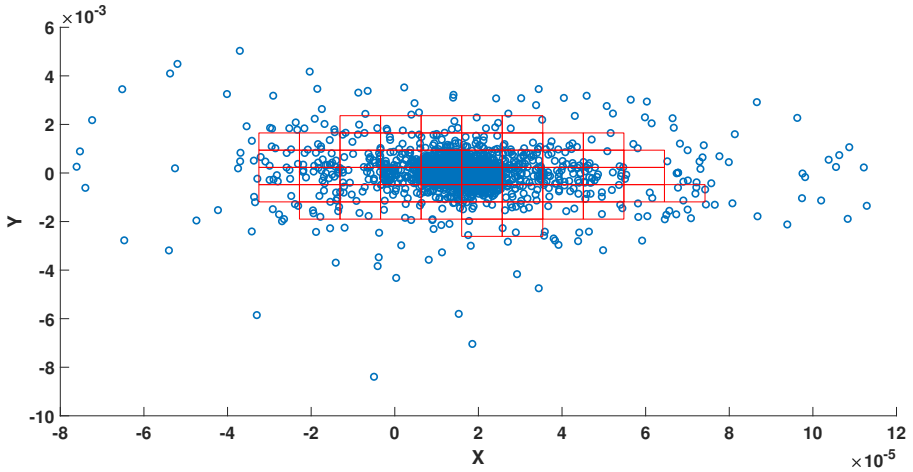

Figure 3.3. The discrete box-counting method to calculate the ellipsoid area of the EMG signal of the VM muscle groups for one gait cycle.

thr is a predefined threshold, the box will be included as the area of the ellipsoid. In order to make sure that boxes will cover a continuous area, a 2D moving average with one sliding window is performed on p_{ij} for smoothing the counted values of each box before comparing them to the threshold. It must be noted that the number of boxes ($n_1 \times n_2$) and the threshold *thr* depend on the total number of data points in the segment. By many trials and errors, we chose $n_1 = n_2 = 10$ and $thr = 0.5$ for the public data set which contains 150 points per cycle, and $n_1 = n_2 = 20$ and $thr = 2$ for the collected data as 2000 data points were considered for each cycle. Fig. 3.3 shows the area to calculate the energy kernel of one of the collected gait cycle data.

3.1.4 K-means Clustering Approach

K-means is a well-known unsupervised approach that can cluster n objects into k classes. K-means clustering minimizes the distortion measure, taking the total intra-cluster variance as a cost function. This method iteratively finds the cluster

centroids and then assigns the data according to the Euclidean distance to the cluster centroids until convergence. In our case, we hypothesize that the energy-RMS cluster of the EMG signal will be distinguishable for various locomotion speeds and activities.

3.1.5 Speed and Activity Change Identification in Separate Trials

The energy and RMS value of EMG signals during each gait cycle are calculated for five subjects in four different trials with different activities and speeds. The subject ID numbers are as given in the public dataset. Fig. 3.4 shows the RMS and energy of EMG signal of the four muscle groups, for two of the subjects. It can be seen that the RMS and energy values of some muscle groups show more clear distinction in the activities than the other ones. Based on our observation from these figures for all subjects, the muscle groups BF and GC are chosen to extract the features. Fig. 3.5 shows the 2D feature space (Energy-RMS) of these two EMG signals for gait speed change and activity change. By considering these 2D features for all four EMG sensors, it seems impossible to use only one EMG sensor to differentiate between speed and activity changes for all subjects. Using two EMG sensors makes the classification among the subjects more robust. The energy feature of EMG signal helps with increasing the distance between the clusters and making the classification more accurate, rather than using only the RMS feature.

As an unsupervised classification approach, K-means clustering has been used to classify the data based on the gait activity or speed change. This approach does not need any training and can group unlabeled data into certain clusters. The only input to this algorithm besides the features, is the number of clusters. Our assumption is

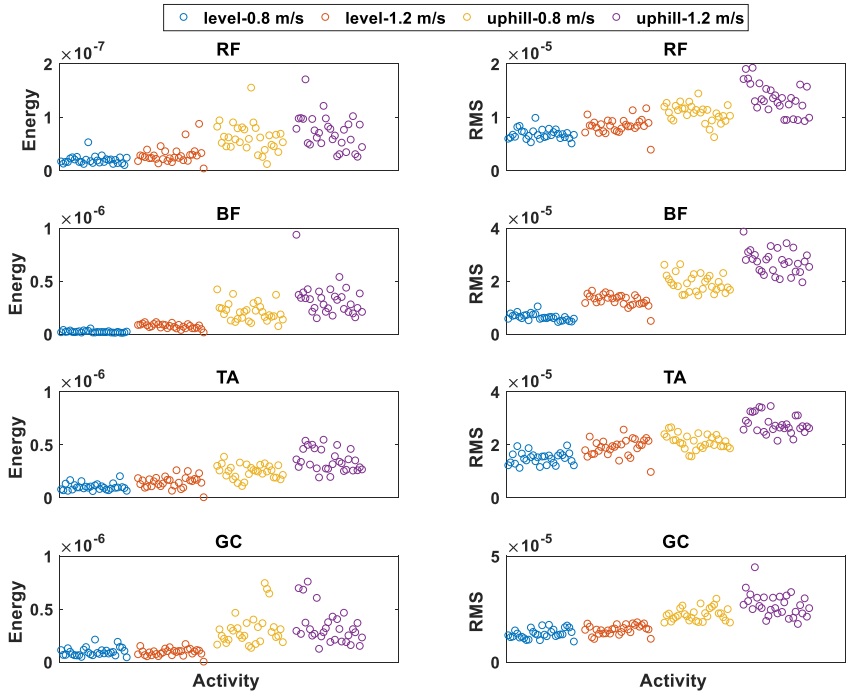

(a) Subject 03

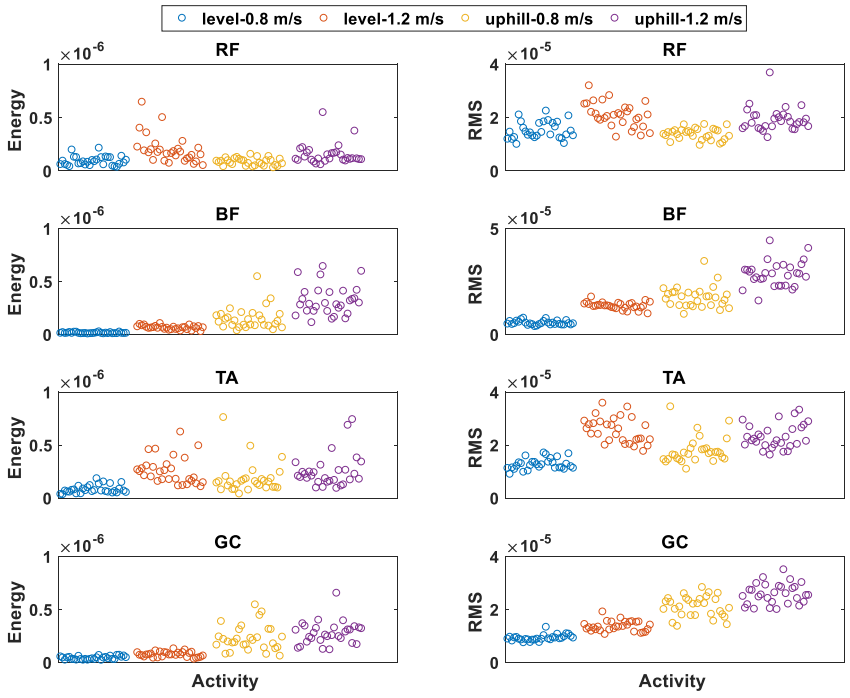

(b) Subject 06

Figure 3.4. The RMS and energy value of 4 muscle groups EMG signal for two subjects in 4 different walking trials: level walking at 0.8 m/s and 1.2 m/s, and uphill walking (10 deg inclined) at 0.8 m/s and 1.2 m/s.

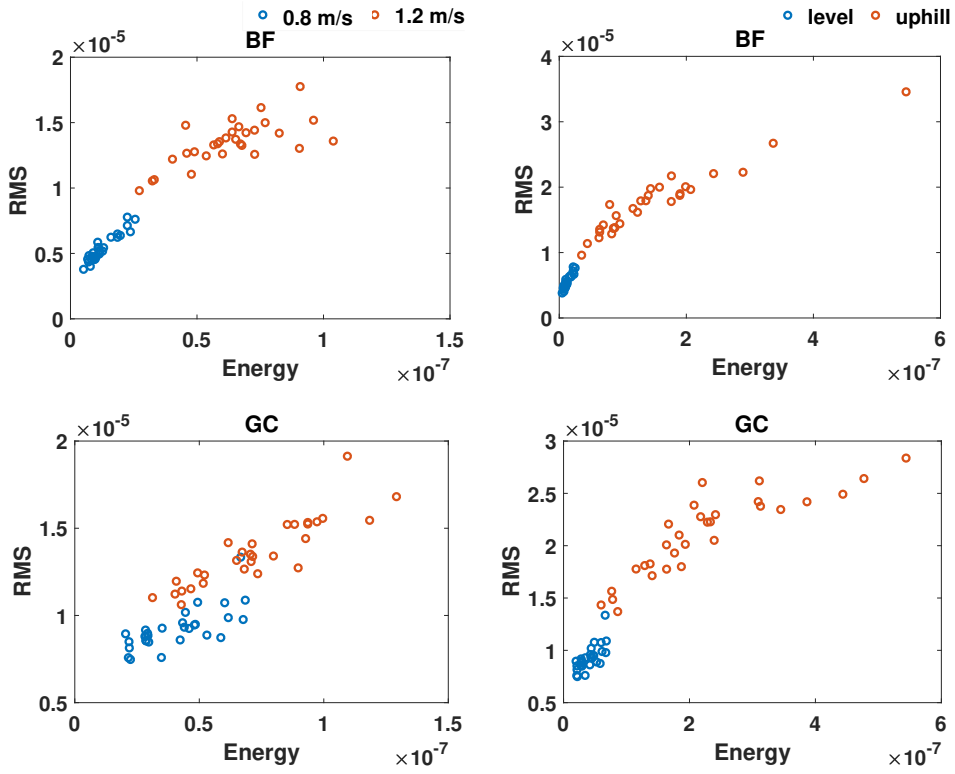

(a) Speed change (0.8 vs 1.2 m/s) (b) Activity change (level vs uphill)

Figure 3.5. The Energy-RMS plots of RF and GC EMG signals of one of the subjects for gait speed change (a) and activity change (b).

that the extracted features of the two EMG signals will remain at almost the same level, as far as the gait speed or activity has not changed, independent of subjects or other conditions. The K-means clustering would be ideal to test this assumption.

The RMS and energy of EMG signal of RF and GC muscle groups were considered as the four features of the K-means clustering. The classification is performed on 30 gait cycles of each trial. The level walking trials at speeds 0.8 and 1.2 m/s are considered together to classify the speed change, and level and uphill walking trials at 0.8 m/s are considered as activity change classifications. The accuracy of the two classifications for all subjects is represented in Fig. 3.6. For all cases, the accuracy of classification is greater than 90%. Depending on the subject, the accuracy of detecting

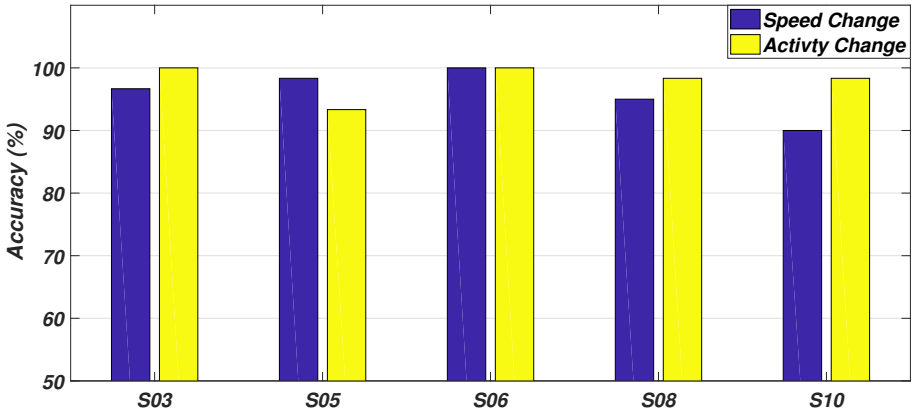

Figure 3.6. The accuracy of K-means classification algorithm to predict gait speed or activity change based on a 4 features space consisting of RMS and energy values of two EMG sensors (BF and GC) in the public dataset

activity or speed change is different, which is expected as different subjects' muscle groups might behave differently in those conditions.

3.1.6 Online Gait Speed Change Detection using Different Muscle Groups

In order to validate the performance of this method in the case that walking speed changes online in one trial, rather than in separate trials, the same analysis is performed on 2 subjects walking on a treadmill while the speed changes twice in the middle of the trial, from slow speed (0.5m/s) to normal speed (0.8 m/s), and then to fast speed (1.2 m/s). Here, EMG signals of VM and VL muscle groups are used to further examine the generalization of this approach. The 2D feature (RMS and energy) of each EMG signal are plotted in Fig. 3.7 for each subject. 15 gait cycles are considered for each speed (total 45 for each trial), and the transition points are not considered here. The reason is that transition points will make the classification and

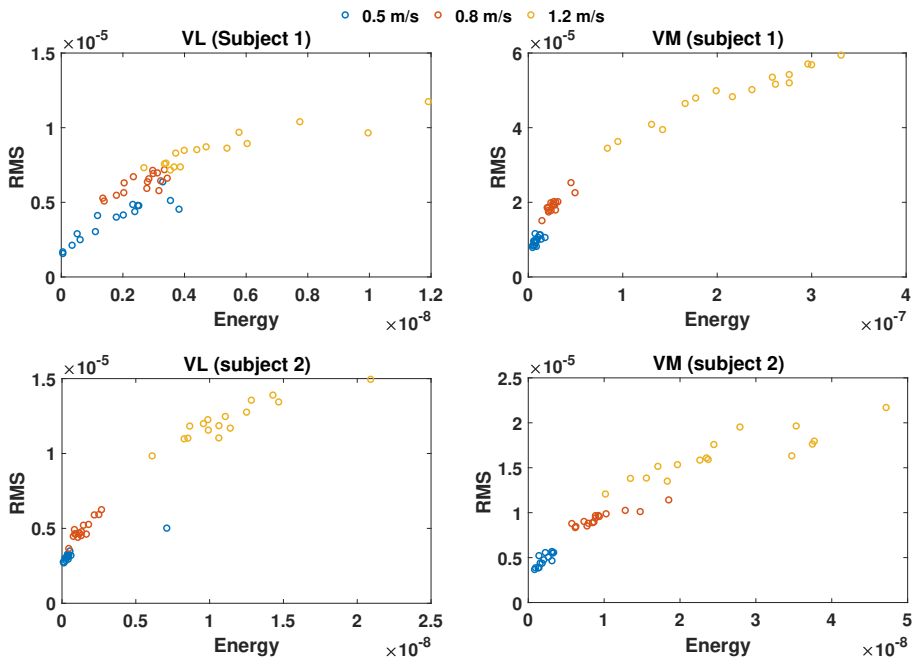

Figure 3.7. The energy-RMS of EMG signal plots for two subjects walking on the treadmill as the speed changes twice: From 0.5 m/s to 0.8 m/s and then to 1.2 m/s. The EMG signal are acquired from two muscle groups, VL and VM. The gait cycles in speed transitions are not considered.

distinction between clusters much more complicated and difficult, and for now, we only focus on speed change from slow walking to normal and fast walking.

From Fig. 3.7 it is observed that using these muscle groups and the proposed features, it is still possible to have separate clusters as the speed changes during walking. The K-means clustering method is performed on the extracted features of these two EMG signal, to classify three clusters for each experiment and the results are shown in table 3.2. As expected, the classification accuracy for all 4 trials is high (more than 97%).

Table 3.2. The speed Change Detection Accuracy for Subjects Walking on the Treadmill as its Speed Changes Two Times

Subject	Trial number	Accuracy
1	1	97.8%
	2	100%
2	1	97.8%
	2	97.8%

3.1.7 Discussion

Essentially RMS and energy of EMG signal are not completely independent features as they are both attributed to the muscle activation level. However, regarding the noisy and stochastic nature of EMG signal, each of them might behave differently, and our result showed that having them as two different features would lead to better classification accuracy.

Based on the results showed in Fig. 3.6, the energy kernel of EMG per gait cycle for lower-limb muscles will remain in certain level or cluster during constant gait activity or speed, and will go to different clusters if the speed or activity changes. Therefore the energy kernel of each gait cycle, during the gait activity or speed change, can be described by damped harmonic oscillators rather than mass-spring model.

The robustness of the proposed method to detect gait speed or activity changes is tested in three ways: across different subjects, across different experimental and data acquisition conditions (two different data set and separate trials), and across two groups of different muscle groups (VM-VL, and BF-GC). We obtained high classification accuracies for all those conditions, suggesting a robust performance of the purposed method. It must be noted that EMG based classification methods are not usually robust, regarding the stochastic and noisy nature of EMG signal, and its sensitivity to the experiment and data acquisition condition. Further experiments can

be performed to address the effects of human physiological change such as muscle fatigue, to examine the robustness of this EMG classification method, in more details.

This method has the potential to be implemented in real time. Both features can be extracted in real time and an online unsupervised classification algorithm can use the proposed 2D feature space to identify changes in the gait. Although the update rate might not be very fast (at least one gait cycle), this method can possibly be used for gait assistive robot applications. Given its accuracy, robustness, few sensors, and applicability to different muscle groups, it can be used to detect any changes in the muscle activation level, and the robotic exoskeleton would alter its policy or level of assistance accordingly.

Chapter 4

HUMAN MOTION ESTIMATION USING INVARIANT EXTENDED KALMAN FILTERING

For human locomotion, both continuous and discrete states have been introduced to quantity and differentiate various motion patterns and intents. Continuous human states are often estimated by sensor fusion and regression models for improved accuracy. The pose (position and orientation) and velocity of the body (e.g., pelvis or chest) are of particular interest in gait analysis and wearable robot controller design because they can be used to study postural balance and gait stability, as well as gait mode analysis.

This chapter proposes an augmented InEKF design that considers the misalignment of the inertial sensor at the trunk as part of the states and preserves the group affine property for the process model. Personalized lower-extremity forward kinematic models are built and employed as the measurement model for the augmented InEKF. Observability analysis for the new InEKF design is presented. The filter is evaluated with three subjects in squatting, rolling-foot walking, and ladder-climbing motions. Experimental results validate the superior performance of the proposed InEKF over the state-of-the-art InEKF. Improved accuracy and faster convergence in estimating the velocity and orientation of humans, in all three motions, are achieved despite the significant initial estimation errors and the uncertainties associated with the forward kinematic measurement model. Although the measurement model is imperfect (i.e., it does not possess an invariant form) and thus its linearization relies on the state estimate, experimental results demonstrate fast convergence of the proposed filter.

4.1 Problem Formulation

In this section, we will introduce an InEKF to estimate the states of the body (e.g., pelvis or chest) and the IMU placement offset, by using an IMU placed on the body to form the process model and by exploiting the stance leg's forward kinematic velocity to build a measurement model. The human forward kinematic model provides the contact point position in the measurement frame (as shown in Fig. 4.1). Thus there are some orientation and positional offsets between the measurement frame, which is considered in human forward kinematic model, and where IMU is placed. The "perfect" placement of the IMU would allow the exact alignment between the IMU and the measurement frame. Yet, such a placement is difficult to achieve in real-world applications without resorting to careful and often time-consuming manual calibration. Here, to address the "imperfect" alignment between frames, we include the (orientation and positional) placement offset as part of the state estimation to make the connection between the process model (IMU) and the measurement more accurate. This will lead to more accurate estimation of the body pose, and eliminate the need for accurate calibration between the IMU and the measurement frames.

4.1.1 Process Model

Since the filtering objective is to estimate the body movement, we choose the state variables of the filter system to be the position $\mathbf{p} \in \mathbb{R}^3$, velocity $\mathbf{v} \in \mathbb{R}^3$, and orientation $\mathbf{R} \in SO(3)$ of the IMU, which is placed on the body, expressed in the world frame. In addition, to explicitly treat the IMU placement offsets, the state variables also include

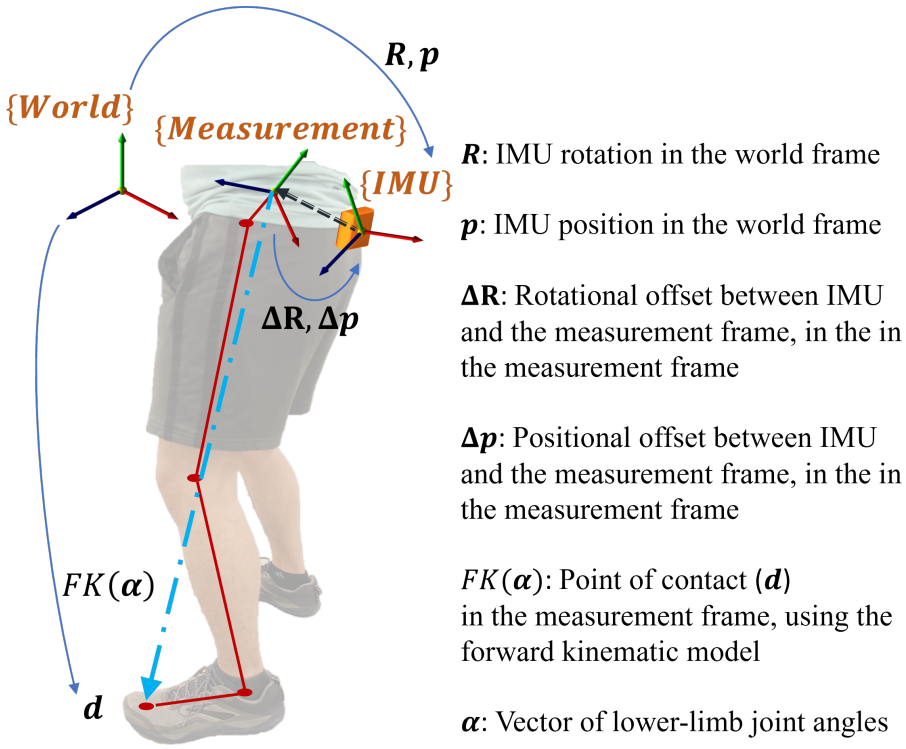

Figure 4.1. Measured and estimated variables in the proposed human body movement estimation. $\{World\}$ represents the world frame and $\{Measurement\}$ is the frame at which the measurements are provided. For the leg forward kinematic measurements, the measurement frame is defined at the center of pelvis. $\{IMU\}$ is the frame attached to the IMU. This figure illustrates the rotational and positional offset between the measurement and IMU frames, as well as the forward kinematics chain.

the positional offset $\Delta\mathbf{p} \in \mathbb{R}^3$ and orientation offset $\Delta\mathbf{R} \in SO(3)$ of the IMU frame, represented in the measurement frame.

The process model is based on the IMU characteristics. The IMU measures the linear acceleration $\mathbf{a} \in \mathbb{R}^3$ and angular velocity $\boldsymbol{\omega} \in \mathbb{R}^3$ in the IMU frame. These sensor readings are corrupted by white Gaussian noise:

$$\tilde{\mathbf{a}} = \mathbf{a} + \mathbf{w}_a, \quad \tilde{\boldsymbol{\omega}} = \boldsymbol{\omega} + \mathbf{w}_\omega. \tag{4.1}$$

Considering these measurements as the input of the IMU motion dynamics, the

process model becomes:

$$\frac{d}{dt}\mathbf{R} = \mathbf{R}(\tilde{\boldsymbol{\omega}} - \mathbf{w}_\omega)_\times, \ \frac{d}{dt}\mathbf{p} = \mathbf{v}, \ \frac{d}{dt}\mathbf{v} = \mathbf{R}(\tilde{\mathbf{a}} - \mathbf{w}_a) + \mathbf{g}, \tag{4.2}$$

where $(.)_\times$ denotes a skew-symmetric matrix and $\mathbf{g}$ is the gravitational acceleration vector.

As the IMU placement offsets are typically constant, we model their dynamics as zero plus small white Gaussian noise $\mathbf{w}_{\Delta p}$ and $\mathbf{w}_{\Delta R}$:

$$\frac{d}{dt}\Delta\mathbf{p} = \mathbf{w}_{\Delta p}, \quad \frac{d}{dt}\Delta\mathbf{R} = \Delta\mathbf{R}(\mathbf{w}_{\Delta R})_\times. \tag{4.3}$$

4.1.2 Measurement model

4.1.2.1 Forward kinematics based measurement

During mobility tasks (e.g., squatting, walking, and stair climbing), when the stance foot has static, secured contact with the ground, the pose of the measurement frame can be obtained through the leg kinematic chain that connects the foot and measurement frames. Note that the joint angles along the kinematic chain are measured by the motion capture system. The kinematic chain is built based on the Vicon lower-body Plug-in-Gait model , in which 3D joint angles (hip, knee, and ankle), along with subject lower-body segment length measurements, were used to obtain the desired 3D vector.

Let $\boldsymbol{\alpha}_t \in \mathbb{R}^k$ be the joint angles of the stance leg with k the number of joint angles. Then the measured joint angle $\tilde{\boldsymbol{\alpha}}_t$ can be expressed as $\tilde{\boldsymbol{\alpha}}_t = \boldsymbol{\alpha}_t + \mathbf{w}_{\alpha_t}$ with $\mathbf{w}_{\alpha_t} \in \mathbb{R}^k$ the zero-mean white Gaussian noise.

Let ${}^{M}\mathbf{d}_t^{MF}$ denote the 3-D position vector pointing from the measurement to the foot frame expressed in the measurement frame. For brevity, we denote it as $\mathbf{d}_t^M$. Let the function h_F be the forward kinematics representing $\mathbf{d}_t^M$; that is, $\mathbf{d}_t^M = h_F(\boldsymbol{\alpha}_t)$.

Given that $\mathbf{d}_t^M = (\Delta\mathbf{R}_t)\mathbf{R}_t^T(\mathbf{d}_t - \mathbf{p}_t) - \Delta\mathbf{p}_t$, we have $\mathbf{d}_t - \mathbf{p}_t = \mathbf{R}_t\Delta\mathbf{R}_t^T(\Delta\mathbf{p}_t + h_F(\boldsymbol{\alpha}_t))$. Taking the first derivative with respect to time t on both sides of this equation, we obtain:

$$\begin{aligned}\frac{d}{dt}(\mathbf{d}_t - \mathbf{p}_t) &= \mathbf{R}_t\Delta\mathbf{R}_t^T(\mathbf{w}_{\Delta p_t} + J(\boldsymbol{\alpha}_t)(\dot{\boldsymbol{\alpha}}_t + \mathbf{w}_{\dot{\alpha}_t})) \\ &+ \left(\mathbf{R}_t(\boldsymbol{\omega}_t + \mathbf{w}_{\omega_t})_\times\Delta\mathbf{R}_t^T + \mathbf{R}_t(\Delta\mathbf{R}_t(\mathbf{w}_{\Delta\mathbf{R}_t})_\times)^T\right)(h_F(\boldsymbol{\alpha}_t) + \Delta\mathbf{p}_t),\end{aligned} \tag{4.4}$$

where $J(\boldsymbol{\alpha}) \triangleq \frac{\partial h_F(\boldsymbol{\alpha})}{\partial \boldsymbol{\alpha}}$ is the forward kinematic Jacobian and $\mathbf{w}_{\dot{\alpha}_t}$ is the joint velocity measurement noise.

Note that $\dot{\mathbf{d}}_t = \mathbf{0}$ due to the stationary contact point. Also, $\dot{\mathbf{p}}_t = \mathbf{v}_t$ holds. Thus, the measurement model in (4.4) can be compactly rewritten as:

$$\mathbf{y} = h(\mathbf{X}_t) + \mathbf{n}_t, \tag{4.5}$$

where $\mathbf{y} = -J(\tilde{\boldsymbol{\alpha}}_t)\dot{\tilde{\boldsymbol{\alpha}}}_t$, $h(\mathbf{X}_t) = (\Delta\mathbf{R}_t)\mathbf{R}_t^T\mathbf{v}_t - (\Delta\mathbf{p}_t)_\times\Delta\mathbf{R}_t\tilde{\boldsymbol{\omega}}_t - (h_F(\tilde{\boldsymbol{\alpha}}_t))_\times\Delta\mathbf{R}_t\tilde{\boldsymbol{\omega}}_t$, and $\mathbf{n}_t = (\Delta\mathbf{p}_t + h_F(\tilde{\boldsymbol{\alpha}}_t)_\times\Delta\mathbf{R}_t(\mathbf{w}_{\Delta R_t} + \mathbf{w}_{\omega_t}) + \mathbf{w}_{\Delta p_t} - J(\tilde{\boldsymbol{\alpha}}_t)\mathbf{w}_{\dot{\alpha}_t}$. For simplicity, $\mathbf{n}_t$ is treated as white, Gaussian, zero-mean noise in this study.

4.1.2.2 3-D vector-based measurement model

To compare the filtering performance under different kinematics measurements formed based on data returned by motion capture systems, we introduce a simplified measurement obtained based on the 3-D position vector between the measurement and foot frame. Both forward kinematics-based and 3-D position vector-based measurements return the relative position and velocity between the measurement and

foot frames. Note that the 3-D position vector-based measurement will have higher accuracy than the forward kinematics measurements.

Let $\mathbf{v}_t^M$ denote the 3-D velocity vector pointing from the measurement to the foot frame expressed in the measurement frame, which is the time derivative of $\mathbf{d}_t^M$. Then the measured 3-D velocity vector $\tilde{\mathbf{v}}_t^M$ is expressed as $\tilde{\mathbf{v}}_t^M = \mathbf{v}^M + \mathbf{w}_{v_t^M}$, with $\mathbf{w}_{v_t^M}$ the noise associated with the 3-D velocity vector measurement.

Given that $\mathbf{d}_t^M = (\Delta\mathbf{R}_t)\mathbf{R}_t^T(\mathbf{d}_t - \mathbf{p}_t) - \Delta\mathbf{p}_t$, we have $\mathbf{d}_t - \mathbf{p}_t = \mathbf{R}_t\Delta\mathbf{R}_t^T(\Delta\mathbf{p}_t + \mathbf{d}_t^M))$. Taking the time derivative on both sides of this equation, we obtain:

$$\begin{aligned}\frac{d}{dt}(\mathbf{d}_t - \mathbf{p}_t) &= \mathbf{R}_t\Delta\mathbf{R}_t^T(\mathbf{w}_{\Delta\mathbf{p}_t} + (\mathbf{v}^M + \mathbf{w}_{v^M})) \\ &+ \left(\mathbf{R}_t(\boldsymbol{\omega})_\times\Delta\mathbf{R}_t^T + \mathbf{R}_t(\Delta\mathbf{R}_t(\mathbf{w}_{\Delta\mathbf{R}_t})_\times)^T\right)(\mathbf{d}_t^M + \Delta\mathbf{p}_t).\end{aligned} \tag{4.6}$$

Assume the contact foot velocity is zero due to the stationary contact point. Then the measurement model (4.6) becomes:

$$\mathbf{y} = h(\mathbf{X}_t) + \mathbf{n}_t \tag{4.7}$$

where $\mathbf{y} = -\tilde{\mathbf{v}}^M$, $h(\mathbf{X}_t) = \Delta\mathbf{R}_t\mathbf{R}_t^T\mathbf{v}_t - (\Delta\mathbf{p}_t)_\times\Delta\mathbf{R}_t\boldsymbol{\omega}_t - (\mathbf{d}_t^M)_\times\Delta\mathbf{R}_t\boldsymbol{\omega}_t + \mathbf{n}_t$, and the vector $\mathbf{n}_t$ is the lumped measurement noise term.

Remark 1: The two measurement models in (4.5) and (4.7) do not satisfy the right-invariant observation form (i.e., $\mathbf{y} = \mathbf{X}^{-1}\mathbf{b}$ for some known vector $\mathbf{b}$) as defined in the theory of InEKF(Barrau and Bonnabel 2016). This is because with the state defined in (4.8) and our measurements in (4.5) and (4.7), a vector $\mathbf{b}$ that is known and satisfies $\mathbf{y} = \mathbf{X}^{-1}\mathbf{b}$ does not exist. Then, by the theory of invariant filtering (Proposition 2 in Barrau and Bonnabel 2016), the error dynamics during the measurement update is not independent of state trajectories.

4.1.3 State Representation and Propagation (Predication)

The first step to designing an InEKF is to define the states on a matrix Lie group G (Howe 1983; Sola, Deray, and Atchuthan 2018), with its associated Lie algebra $\mathfrak{g}$. Here the variables we wish to estimate (introduced in Sec. 4.1.1) are represented on a matrix Lie group:

$$\mathbf{X} = \begin{bmatrix} \mathbf{R} & \mathbf{v} & \mathbf{p} & \mathbf{0}_{3,3} & \mathbf{0}_{3,1} \\ \mathbf{0}_{1,3} & 1 & 0 & \mathbf{0}_{1,3} & \mathbf{0}_{3,1} \\ \mathbf{0}_{1,3} & 0 & 1 & \mathbf{0}_{1,3} & \mathbf{0}_{3,1} \\ \mathbf{0}_{3,1} & \mathbf{0}_{3,1} & \mathbf{0}_{3,1} & \Delta\mathbf{R} & \Delta\mathbf{p} \\ \mathbf{0}_{1,3} & 0 & 0 & \mathbf{0}_{1,3} & 1 \end{bmatrix} \in G, \tag{4.8}$$

where the matrix Lie group G is an extension of the special Euclidean group $SE(3)$, and $\mathbf{0}_{n,m}$ represents an $n \times m$ matrix with all elements being zero. The proof that G is a matrix Lie group is given in the appendix.

The core idea of the InEKF is the invariant error definition. The right-invariant error between the true and estimation value is denoted as:

$$\boldsymbol{\eta} = \bar{\mathbf{X}}\mathbf{X}^{-1} \in G, \tag{4.9}$$

where $\overline{(.)}$ denotes the estimated value of the variable $(.)$.

The tangent space $\mathfrak{g}$ (defined at the identity element $\mathbf{E} \in G$) is a vector space that can also be represented by vectors in the Cartesian space $\mathbb{R}^{dim\mathfrak{g}}$. This transformation is a linear map that we define as $(.)^\wedge : \mathbb{R}^{dim\mathfrak{g}} \to \mathfrak{g}$. Therefore for the vector $\boldsymbol{\zeta} = \text{vec}(\boldsymbol{\zeta}_R, \boldsymbol{\zeta}_v, \boldsymbol{\zeta}_p, \boldsymbol{\zeta}_{\Delta R}, \boldsymbol{\zeta}_{\Delta p}) \in \mathbb{R}^{dim\mathfrak{g}}$, this linear map has the form (Sola, Deray, and

Atchuthan 2018,Hartley et al. 2019):

$$\boldsymbol{\zeta}^{\wedge} = \begin{bmatrix} (\boldsymbol{\zeta}_R)_{\times} & \boldsymbol{\zeta}_v & \boldsymbol{\zeta}_p & \mathbf{0}_{3,3} & \mathbf{0}_{3,1} \\ \mathbf{0}_{1,3} & 0 & 0 & \mathbf{0}_{1,3} & \mathbf{0}_{3,1} \\ \mathbf{0}_{1,3} & 0 & 0 & \mathbf{0}_{1,3} & \mathbf{0}_{3,1} \\ \mathbf{0}_{3,3} & \mathbf{0}_{3,1} & \mathbf{0}_{3,1} & (\boldsymbol{\zeta}_{\Delta R})_{\times} & \boldsymbol{\zeta}_{\Delta p} \\ \mathbf{0}_{1,3} & 0 & 0 & \mathbf{0}_{1,3} & 0 \end{bmatrix} \in \mathfrak{g}. \tag{4.10}$$

Now we can define the exponential map of our Lie group, $\boldsymbol{\eta}_t = \exp(\boldsymbol{\zeta})$. The exponential map takes $\forall \boldsymbol{\zeta} \in \mathbb{R}^n$ to the corresponding matrix representation in G as:

$$\exp(.) : \mathbb{R}^{dim\mathfrak{g}} \to G, \quad \exp(\boldsymbol{\zeta}) = \exp_m(\boldsymbol{\zeta}^{\wedge}), \tag{4.11}$$

where $\exp_m(.)$ is the matrix exponential.

The dynamics of the system can be written using (4.1)-(4.3):

$$\begin{aligned} \frac{d}{dt}\mathbf{X}_t = & \begin{bmatrix} \mathbf{R}_t(\tilde{\boldsymbol{\omega}}_t)_{\times} & \mathbf{R}_t\tilde{\mathbf{a}}_t + \mathbf{g} & \mathbf{v}_t & \mathbf{0}_{3,3} & \mathbf{0}_{3,1} \\ \mathbf{0}_{1,3} & 0 & 0 & \mathbf{0}_{1,3} & \mathbf{0}_{3,1} \\ \mathbf{0}_{1,3} & 0 & 0 & \mathbf{0}_{1,3} & \mathbf{0}_{3,1} \\ \mathbf{0}_{3,3} & \mathbf{0}_{3,1} & \mathbf{0}_{3,1} & \mathbf{0}_{3,3} & \mathbf{0}_{3,1} \\ \mathbf{0}_{1,3} & 0 & 0 & \mathbf{0}_{1,3} & 0 \end{bmatrix} \\ & - \mathbf{X}_t \begin{bmatrix} (\mathbf{w}_{\omega_t})_{\times} & \mathbf{w}_{a_t} & \mathbf{0}_{3,1} & \mathbf{0}_{3,3} & \mathbf{0}_{3,1} \\ \mathbf{0}_{1,3} & 0 & 0 & \mathbf{0}_{1,3} & \mathbf{0}_{3,1} \\ \mathbf{0}_{1,3} & 0 & 0 & \mathbf{0}_{1,3} & \mathbf{0}_{3,1} \\ \mathbf{0}_{3,3} & \mathbf{0}_{3,3} & \mathbf{0}_{3,3} & (\mathbf{w}_{\Delta R_t})_{\times} & \mathbf{w}_{\Delta p_t} \\ \mathbf{0}_{1,3} & 0 & 0 & \mathbf{0}_{1,3} & 0 \end{bmatrix} \\ & \triangleq f_{u_t}(\mathbf{X}_t) - \mathbf{X}_t\mathbf{w}_t^{\wedge}, \end{aligned} \tag{4.12}$$

where $(\cdot)_t$ denotes the values of the variable $(\cdot)$ at time instant t. Here the noise vector $\mathbf{w}_t$ is defined as $\mathbf{w}_t \triangleq \text{vec}(\mathbf{w}_{\omega_t}, \mathbf{w}_{a_t}, \mathbf{0}_{3,1}, \mathbf{w}_{\Delta R_t}, \mathbf{w}_{\Delta p_t})$.

It can be shown that the deterministic dynamics $f_{u_t}(.)$ meets the following group affine condition (Barrau and Bonnabel 2016) (see Appendix for proof):

$$f_{u_t}(\mathbf{X}_1\mathbf{X}_2) = f_{u_t}(\mathbf{X}_1)\mathbf{X}_2 + \mathbf{X}_1 f_{u_t}(\mathbf{X}_2) - \mathbf{X}_1 f_{u_t}(\mathbf{E})\mathbf{X}_2. \tag{4.13}$$

Therefore, according to (Barrau and Bonnabel 2016), the right-invariant error has deterministic autonomous dynamics (that are independent of state) as below:

$$\frac{d}{dt}\boldsymbol{\eta}_t = g_{u_t}(\boldsymbol{\eta}_t), \quad g_{u_t}(\boldsymbol{\eta}_t) = f_{u_t}(\boldsymbol{\eta}_t) - \boldsymbol{\eta}_t f_{u_t}(\mathbf{E}), \tag{4.14}$$

and if we consider the noise in the system we will have:

$$\frac{d}{dt}\boldsymbol{\eta}_t = f_{u_t}(\boldsymbol{\eta}_t) - \boldsymbol{\eta}_t f_{u_t}(\mathbf{E}) + Ad_{\bar{\mathbf{X}}_t}\mathbf{w}_t^{\wedge} \triangleq g_{u_t}(\boldsymbol{\eta}_t) + \bar{\mathbf{w}}_t^{\wedge}, \tag{4.15}$$

Here, for any $\mathbf{X}_t \in G$, the adjoint map $Ad_{\mathbf{X}_t} : \mathfrak{g} \to \mathfrak{g}$ is the linear mapping from the local tangent space (defined at $\mathbf{X}_t$) to the global tangent space (defined at the identity element $\mathbf{E}$) in the Lie algebra: $Ad_{\mathbf{X}_t}(.)^{\wedge} \triangleq \mathbf{X}_t(.)^{\wedge}\mathbf{X}_t^{-1}$. Therefore, the adjoint matrix representation for $\mathbf{X}_t$ can be obtained as:

$$Ad_{\mathbf{X}_t} = \begin{bmatrix} \mathbf{R}_t & \mathbf{0}_{3,3} & \mathbf{0}_{3,3} & \mathbf{0}_{3,3} & \mathbf{0}_{3,3} \\ (\mathbf{v}_t)_{\times}\mathbf{R}_t & \mathbf{R}_t & \mathbf{0}_{3,3} & \mathbf{0}_{3,3} & \mathbf{0}_{3,3} \\ (\mathbf{p}_t)_{\times}\mathbf{R}_t & \mathbf{0}_{3,3} & \mathbf{R}_t & \mathbf{0}_{3,3} & \mathbf{0}_{3,3} \\ \mathbf{0}_{3,3} & \mathbf{0}_{3,3} & \mathbf{0}_{3,3} & \Delta\mathbf{R}_t & \mathbf{0}_{3,3} \\ \mathbf{0}_{3,3} & \mathbf{0}_{3,3} & \mathbf{0}_{3,3} & (\Delta\mathbf{p}_t)_{\times}\Delta\mathbf{R}_t & \Delta\mathbf{R}_t \end{bmatrix}. \tag{4.16}$$

Moreover, we can obtain a log-linear error equation using the first-order approximation of the exponential map and (4.15). Specifically, by the definition of exp, we have $\boldsymbol{\eta}_t = \exp(\boldsymbol{\zeta}_t) \approx \mathbf{E} + \boldsymbol{\zeta}_t^{\wedge}$. Also, by the theory of invariant filtering (Barrau and Bonnabel

2016), we can obtain the Jacobian $\mathbf{A}_t$ of deterministic part of (4.15):

$$g_{u_t}(\exp(\boldsymbol{\zeta}_t)) = (\mathbf{A}_t\boldsymbol{\zeta}_t)^\wedge + \text{h.o.t.}(\|\boldsymbol{\zeta}_t\|) \approx (\mathbf{A}_t\boldsymbol{\zeta}_t)^\wedge, \tag{4.17}$$

where h.o.t. represents the higher-order terms. Then, from (4.14), we obtain the log-linear error equation:

$$\frac{d}{dt}\boldsymbol{\zeta}_t = \mathbf{A}_t\boldsymbol{\zeta}_t. \tag{4.18}$$

Therefore, for given initial right-invariant error $\boldsymbol{\eta}_0 = \exp(\boldsymbol{\zeta}_0)$, $\boldsymbol{\eta}_t$ can be recovered using (4.18). This results in linear right-invariant error propagation (predication) in the filter, which is exact for the deterministic case. With the process noise considered, the linear error equation in $\boldsymbol{\zeta}_t$ becomes $\frac{d}{dt}\boldsymbol{\zeta}_t = \mathbf{A}_t\boldsymbol{\zeta}_t + \bar{\mathbf{w}}_t$.

We are now ready to derive the expression of $\mathbf{A}_t$ defined in (4.17), by substituting the first-order approximation of the right-invariant error into the definition of g_{u_t} in

(4.15):

$$
\begin{aligned}
& g_{u_t}(\exp(\boldsymbol{\eta}_t)) \approx g_{u_t}(\mathbf{E} + \boldsymbol{\zeta}_t^{\wedge}) \\
&= \begin{bmatrix}
(\mathbf{I}_3 + (\boldsymbol{\zeta}_{R_t})_\times)(\tilde{\boldsymbol{\omega}}_t)_\times & (\mathbf{I}_3 + (\boldsymbol{\zeta}_{R_t})_\times)\tilde{\mathbf{a}}_t + \mathbf{g} & \boldsymbol{\zeta}_{v_t} & 0_{3,4} \\
\mathbf{0}_{1,3} & 0 & 0 & \mathbf{0}_{1,4} \\
\mathbf{0}_{1,3} & 0 & 0 & \mathbf{0}_{1,4} \\
\mathbf{0}_{3,3} & \mathbf{0}_{3,1} & \mathbf{0}_{3,1} & \mathbf{0}_{3,4} \\
\mathbf{0}_{1,3} & 0 & 0 & \mathbf{0}_{1,4}
\end{bmatrix} \\
&- \begin{bmatrix}
\mathbf{I}_3 + (\boldsymbol{\zeta}_{R_t})_\times & \boldsymbol{\zeta}_{v_t} & \boldsymbol{\zeta}_{p_t} & \mathbf{0}_{3,3} & 0 \\
\mathbf{0}_{1,3} & 0 & 0 & \mathbf{0}_{1,3} & 0 \\
\mathbf{0}_{1,3} & 0 & 0 & \mathbf{0}_{1,3} & 0 \\
\mathbf{0}_{3,3} & \mathbf{0}_{3,1} & \mathbf{0}_{3,1} & (\boldsymbol{\zeta}_{\Delta R_t})_\times & \boldsymbol{\zeta}_{\Delta p_t} \\
\mathbf{0}_{1,3} & 0 & 0 & \mathbf{0}_{1,3} & 0
\end{bmatrix}
\begin{bmatrix}
(\tilde{\boldsymbol{\omega}}_t)_\times & \tilde{\mathbf{a}}_t + \mathbf{g} & \mathbf{0}_{3,5} \\
\mathbf{0}_{1,3} & 0 & \mathbf{0}_{1,5} \\
\mathbf{0}_{1,3} & 0 & \mathbf{0}_{1,5} \\
\mathbf{0}_{3,3} & \mathbf{0}_{3,1} & \mathbf{0}_{3,5} \\
\mathbf{0}_{1,3} & 0 & \mathbf{0}_{1,5}
\end{bmatrix} \\
&= \begin{bmatrix}
\mathbf{0}_{3,3} & (\mathbf{g})_\times \boldsymbol{\zeta}_{R_t} & \boldsymbol{\zeta}_{v_t} & \mathbf{0}_{3,4} \\
\mathbf{0}_{1,3} & 0 & 0 & \mathbf{0}_{1,4} \\
\mathbf{0}_{1,3} & 0 & 0 & \mathbf{0}_{1,4} \\
\mathbf{0}_{3,3} & \mathbf{0}_{3,1} & \mathbf{0}_{3,1} & \mathbf{0}_{3,4} \\
\mathbf{0}_{1,3} & 0 & 0 & \mathbf{0}_{1,4}
\end{bmatrix} = \begin{bmatrix}
\mathbf{0}_{3,1} \\
(\mathbf{g})_\times \\
\boldsymbol{\zeta}_{v_t} \\
\mathbf{0}_{3,1} \\
\mathbf{0}_{3,1}
\end{bmatrix}^{\wedge},
\end{aligned}
\tag{4.19}
$$

which yields

$$
\mathbf{A}_t = \begin{bmatrix}
\mathbf{0}_{3,3} & \mathbf{0}_{3,3} & \mathbf{0}_{3,3} & \mathbf{0}_{3,3} & \mathbf{0}_{3,3} \\
(\mathbf{g})_\times & \mathbf{0}_{3,3} & \mathbf{0}_{3,3} & \mathbf{0}_{3,3} & \mathbf{0}_{3,3} \\
\mathbf{0}_{3,3} & \mathbf{I}_3 & \mathbf{0}_{3,3} & \mathbf{0}_{3,3} & \mathbf{0}_{3,3} \\
\mathbf{0}_{3,3} & \mathbf{0}_{3,3} & \mathbf{0}_{3,3} & \mathbf{0}_{3,3} & \mathbf{0}_{3,3} \\
\mathbf{0}_{3,3} & \mathbf{0}_{3,3} & \mathbf{0}_{3,3} & \mathbf{0}_{3,3} & \mathbf{0}_{3,3}
\end{bmatrix},
\tag{4.20}
$$

where $\mathbf{I}_3$ is the 3×3 identity matrix.

Now we can write down the predication step of our InEKF, which consists of the propagation of the state estimate $\bar{\mathbf{X}}_t$ through the process model as well as the

propagation of the covariance matrix $\mathbf{P}_t$ through the Riccati equation (Maybeck 1982):

$$\frac{d}{dt}\bar{\mathbf{X}}_t = f_{u_t}(\bar{\mathbf{X}}_t), \quad \frac{d}{dt}\mathbf{P}_t = \mathbf{A}_t\mathbf{P}_t + \mathbf{P}_t\mathbf{A}_t^T + \bar{\mathbf{Q}}_t, \tag{4.21}$$

where $\bar{\mathbf{Q}}_t$ is the process noise covariance defined as $\bar{\mathbf{Q}}_t \triangleq \mathrm{Cov}(\bar{\mathbf{w}}_t) = Ad_{\bar{\mathbf{X}}_t}\mathrm{Cov}(\mathbf{w}_t)Ad_{\bar{\mathbf{X}}_t}$.

In order to implement the filter in discrete time, Euler integration has been performed. The discrete filter propagation equations are given in the appendix.

4.1.4 Measurement update

The nonlinear measurement model (4.5) does not follow the right-invariant form, so we use a first-order approximation to find the innovation as:

$$\mathbf{H}_t\boldsymbol{\zeta}_t + \text{h.o.t}(\boldsymbol{\zeta}_t) \triangleq h(\bar{\mathbf{X}}_t) - h(\mathbf{X}_t). \tag{4.22}$$

Since $\boldsymbol{\eta}_t \approx \bar{\mathbf{X}}_t\mathbf{X}_t^{-1} \approx \mathbf{I} + \boldsymbol{\zeta}_t^{\wedge}$, we can derive the following relationships between the true and estimated states with $\boldsymbol{\zeta}_t$:

$$\begin{aligned}
&\Rightarrow \mathbf{R}_t^T \approx \bar{\mathbf{R}}_t^T(\mathbf{I} + (\boldsymbol{\zeta}_{R_t})_\times),\ \Delta\mathbf{R}_t^T \approx \Delta\bar{\mathbf{R}}_t^T(\mathbf{I} + (\boldsymbol{\zeta}_{\Delta R_t})_\times) \\
&\quad \mathbf{v}_t \approx (\mathbf{I} - (\boldsymbol{\zeta}_{R_t})_\times)(\bar{\mathbf{v}}_t - \boldsymbol{\zeta}_{v_t}),\ \Delta\mathbf{p}_t \approx (\mathbf{I} - (\boldsymbol{\zeta}_{\Delta R_t})_\times)(\overline{\Delta\mathbf{p}}_t - \boldsymbol{\zeta}_{\Delta p_t}).
\end{aligned}$$

Now $\mathbf{H}_t$ can be computed by differentiating (4.22) after dropping the nonlinear terms:

$$\begin{aligned}
\mathbf{H}_t =& \big[\mathbf{0}_{3,3},\ \Delta\bar{\mathbf{R}}_t\bar{\mathbf{R}}_t^T,\ \mathbf{0}_{3,3},\ \mathbf{h}_4,\ (\Delta\bar{\mathbf{R}}_t\boldsymbol{\omega}_t)_\times\big], \\
\mathbf{h}_4 =& -(\Delta\bar{\mathbf{R}}_t\bar{\mathbf{R}}_t^T\bar{\mathbf{v}}_t)_\times - (\Delta\bar{\mathbf{R}}_t\boldsymbol{\omega}_t)_\times(\overline{\Delta\mathbf{p}}_t)_\times \\
&+ (\overline{\Delta\mathbf{p}}_t)_\times(\Delta\bar{\mathbf{R}}_t\boldsymbol{\omega}_t)_\times + (h_F(\boldsymbol{\alpha}_t))_\times(\Delta\bar{\mathbf{R}}_t\boldsymbol{\omega}_t)_\times.
\end{aligned} \tag{4.23}$$

For 3-D position based measurement model, the element $\mathbf{h}_4$ of the matrix $\mathbf{H}_t$ is slightly different from (4.23). The $h_F(\boldsymbol{\alpha}_t))$ needs to be replaced as $\mathbf{d}_t^M$:

$$\begin{aligned}\mathbf{H}_t =&[\mathbf{0}_{3,3},\ \Delta\bar{\mathbf{R}}_t\bar{\mathbf{R}}_t^T,\ \mathbf{0}_{3,3},\ \mathbf{h}_4,\ (\Delta\bar{\mathbf{R}}_t\boldsymbol{\omega}_t)_\times],\\ \mathbf{h}_4 =& -(\Delta\bar{\mathbf{R}}_t\bar{\mathbf{R}}_t^T\bar{\mathbf{v}}_t)_\times - (\Delta\bar{\mathbf{R}}_t\boldsymbol{\omega}_t)_\times(\overline{\Delta\mathbf{p}}_t)_\times\\ &+ (\overline{\Delta\mathbf{p}}_t)_\times(\Delta\bar{\mathbf{R}}_t\boldsymbol{\omega}_t)_\times + (\mathbf{d}_t^M)_\times(\Delta\bar{\mathbf{R}}_t\boldsymbol{\omega}_t)_\times.\end{aligned} \tag{4.24}$$

Now we can express the update equation for our InEKF based on the InEKF methodology (Barrau and Bonnabel 2016):

$$\begin{aligned}\bar{\mathbf{X}}_t^+ &= \exp(\mathbf{K}_t(\mathbf{y}_t - h(\bar{\mathbf{X}}_t)))\bar{\mathbf{X}}_t,\\ \mathbf{P}_t^+ &= (\mathbf{I} - \mathbf{K}_t\mathbf{H}_t)\mathbf{P}_t^-(\mathbf{I} - \mathbf{K}_t\mathbf{H}_t)^T + \mathbf{K}_t\mathbf{N}_t\mathbf{K}_t^T,\end{aligned} \tag{4.25}$$

where $\bar{\mathbf{X}}_t^+$ and $\mathbf{P}_t^+$ are the updated values. Here, the Kalman gain $\mathbf{K}_t$ and measurement noise covariance $\mathbf{N}_t$ are defined as: $\mathbf{K}_t = \mathbf{P}_t\mathbf{H}_t^T\mathbf{S}_t^{-1}$, $\mathbf{S}_t = \mathbf{H}_t\mathbf{P}_t^-\mathbf{H}_t^T + \mathbf{N}_t$, and $\mathbf{N}_t = \bar{\mathbf{R}}_t\Delta\bar{\mathbf{R}}_t^T\mathrm{Cov}(\mathbf{n}_t)\Delta\bar{\mathbf{R}}_t\bar{\mathbf{R}}_t^T$.

4.2 OBSERVABILITY ANALYSIS

By introducing the new states and measurement model, we need to analyze the observability of the whole system. Here we only include the linear observability analysis, and leave the nonlinear observability analysis for future work. Similar to Huang, Mourikis, and Roumeliotis 2010, we analyze the observability around the operating point, which is the latest estimated value that the system is linearized about.

Algorithm 1 Proposed InEKF design

Initialize $\bar{\mathbf{X}} \in G$ and $\mathbf{P} = \mathbf{P}^T > 0$
for iteration=$1, 2, \ldots$ **do**
  if foot contact is detected **then**
    Propagation step:
    $\frac{d}{dt}\bar{\mathbf{X}}_t = f_{u_t}(\bar{\mathbf{X}}_t)$, $\frac{d}{dt}\mathbf{P}_t = \mathbf{A}_t\mathbf{P}_t + \mathbf{P}_t\mathbf{A}_t^T + \bar{\mathbf{Q}}_t$
    Measurement update step:
    $\mathbf{K}_t = \mathbf{P}_t\mathbf{H}_t^T\mathbf{S}_t^{-1}$, $\mathbf{S}_t = \mathbf{H}_t\mathbf{P}_t^-\mathbf{H}_t^T + \mathbf{N}_t$,
    $\mathbf{N}_t = \bar{\mathbf{R}}_t\Delta\bar{\mathbf{R}}_t^T \mathrm{Cov}(\mathbf{n}_t)\Delta\bar{\mathbf{R}}_t\bar{\mathbf{R}}_t^T$
    if using forward kinematics-based measurement **then**
      $\mathbf{y} = -J(\tilde{\boldsymbol{\alpha}}_t)\dot{\tilde{\boldsymbol{\alpha}}}_t$
    else if using 3-D vector-based measurement **then**
      $\mathbf{y} = -\tilde{\mathbf{v}}_t^M$
    end if
    $\bar{\mathbf{X}}_t^+ = \exp(\mathbf{K}_t(\mathbf{y}_t - h(\bar{\mathbf{X}}_t^-)))\bar{\mathbf{X}}_t^-$
    $\mathbf{P}_t^+ = (\mathbf{I} - \mathbf{K}_t\mathbf{H}_t)\mathbf{P}_t^-(\mathbf{I} - \mathbf{K}_t\mathbf{H}_t)^T + \mathbf{K}_t\mathbf{N}_t\mathbf{K}_t^T$
  end if
end for

The discrete filter is described as:

$$\mathbf{X}_{k+1} = \boldsymbol{\Phi}_k\mathbf{X}_k, \quad \mathbf{y}_k = \mathbf{H}_k\mathbf{X}_k, \quad \boldsymbol{\Phi}_k = \exp_m(\mathbf{A}_k\Delta t), \tag{4.26}$$

where $\Delta t = t_{k+1} - t_k$, and $\boldsymbol{\Phi}_k$ is the discrete-time state transition matrix, which can be computed as:

$$\boldsymbol{\Phi}_k = \exp_m(\mathbf{A}_k\Delta t) = \begin{bmatrix} \mathbf{I}_3 & \mathbf{0}_{3,3} & \mathbf{0}_{3,3} & \mathbf{0}_{3,3} & \mathbf{0}_{3,3} \\ (\mathbf{g})_\times\Delta t & \mathbf{I}_3 & \mathbf{0}_{3,3} & \mathbf{0}_{3,3} & \mathbf{0}_{3,3} \\ \frac{1}{2}(\mathbf{g})_\times\Delta t^2 & \mathbf{I}_3\Delta t & \mathbf{I}_3 & \mathbf{0}_{3,3} & \mathbf{0}_{3,3} \\ \mathbf{0}_{3,3} & \mathbf{0}_{3,3} & \mathbf{0}_{3,3} & \mathbf{I}_3 & 0_{3,3} \\ \mathbf{0}_{3,3} & \mathbf{0}_{3,3} & \mathbf{0}_{3,3} & \mathbf{0}_{3,3} & \mathbf{I}_3 \end{bmatrix}. \tag{4.27}$$

Then the observability matrix $\mathbf{O}$ can be computed as:

$$\mathbf{O} = \begin{bmatrix} \mathbf{H}_k^- \\ \mathbf{H}_{k+1}^- \mathbf{\Phi}_k^+ \\ \mathbf{H}_{k+2}^- \mathbf{\Phi}_{k+1}^+ \mathbf{\Phi}_k^+ \\ \vdots \end{bmatrix} = \begin{bmatrix} \mathbf{0}_{3,3} & \Delta\mathbf{R}_k^- \mathbf{R}_k^{-T} & \mathbf{0}_{3,3} & o_{0,4} & (\Delta\mathbf{R}_k^- \boldsymbol{\omega}_k)_\times \\ o_{1,1} & o_{1,2} & \mathbf{0}_{3,3} & o_{1,4} & o_{1,5} \\ \vdots & \vdots & \vdots & \vdots & \vdots \\ o_{4,1} & o_{4,2} & \mathbf{0}_{3,3} & o_{4,4} & o_{4,5} \\ \vdots & \vdots & \vdots & \vdots & \vdots \end{bmatrix} \tag{4.28}$$

where $(.)_k^+$ denotes the updated estimated state at time t_k, $(.)_k^-$ is the estimated state at time t_k after the propagation step. Here the terms $o_{i,1}$, $o_{i,2}$, $o_{i,4}$, and $o_{i,5}$ $(i \in \mathbb{N}^+)$ are defined as:

$$\begin{aligned} o_{i,1} =& i(\Delta\mathbf{R}_{k+i}^- \mathbf{R}_{k+1}^{-T} (\mathbf{g})_\times \Delta t); \quad o_{i,2} = \Delta\mathbf{R}_{k+i}^- \mathbf{R}_{k+1}^{-T}; \\ o_{i,4} =& -(\Delta\mathbf{R}_{k+i}^- \mathbf{R}_{k+1}^{-T} \mathbf{v}_{k+i}^-)_\times - (\Delta\mathbf{R}_{k+i}^- \omega_{k+i})_\times (\Delta\mathbf{p}_{k+i}^-)_\times \\ & + (\Delta\mathbf{p}_{k+i}^-)_\times (\Delta\mathbf{R}_{k+i}^- \boldsymbol{\omega}_{k+i})_\times + (FK(\boldsymbol{\alpha}_{k+i}))_\times (\Delta\mathbf{R}_{k+i}^- \boldsymbol{\omega}_{k+i})_\times; \\ o_{i,5} =& (\Delta\mathbf{R}_{k+i}^- \boldsymbol{\omega}_{k+1})_\times. \end{aligned}$$

To analyze the observability for each variable of interest, we need to see if the corresponding column vectors in $\mathbf{O}$ are linearly independent. From the observability matrix $\mathbf{O}$, it can be seen that the position of the IMU in the world frame is completely non-observable. The yaw angle of the IMU is also non-observable as the third column of the matrix $\mathbf{g}_\times$ is always zero. These results are similar to what was reported in Hartley et al. 2019. The observability of $\Delta\mathbf{p}$ and $\Delta\mathbf{R}$ depends on the rotational movement. For example, if the human is completely stationary $(\boldsymbol{\omega}, \mathbf{v} = \mathbf{0})$, both $\Delta\mathbf{p}$ and $\Delta\mathbf{R}$ are completely unobservable, as all corresponding columns in $\mathbf{O}$ are zero. If $\boldsymbol{\omega} = \mathbf{0}, \mathbf{v} \neq 0$, then $\Delta\mathbf{p}$ is completely non-observable, while it can be shown at least one of the components of $\Delta\mathbf{R}$ is observable. In general, if the direction of $\boldsymbol{\omega}$ is constant, then $\Delta\mathbf{p}$ will be non-observable in at least one direction (see Appendix).

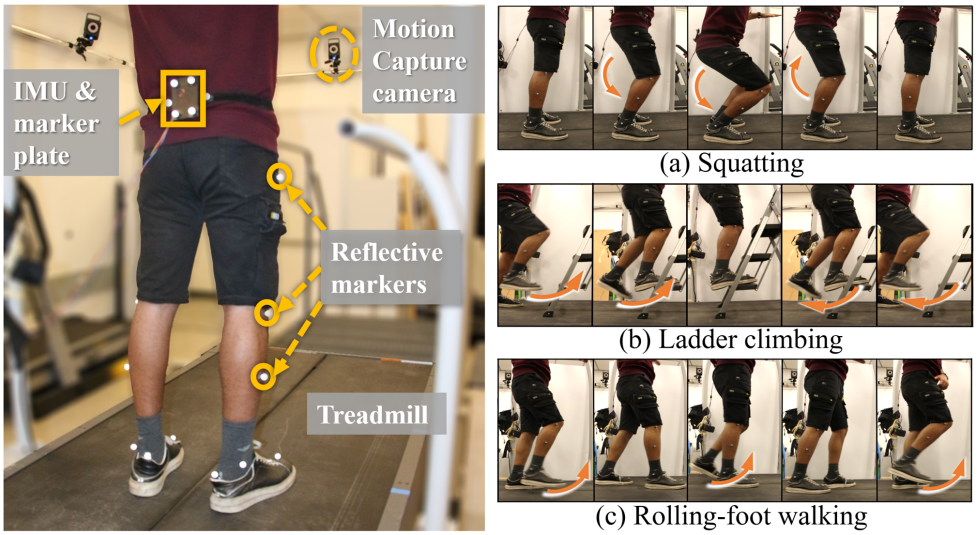

Figure 4.2. The left figure shows the experimental setup used to collect the ground truth of the estimated state variables and the sensor data needed by the proposed filter. The right figure shows time-lapse figures of the three motion types. The arrows in the subplots indicate the direction of the pelvis movement (in subplot (a)) and swing foot movement (subplots (b) and (c)).

4.3 Experimental Results

4.3.1 Experimental setup and protocol

Experiments were performed in a motion capture laboratory at Arizona State University (ASU) with 3 participants (two males and one female, 27 ± 3 years old, $174 \pm 17cm$, $77 \pm 17kg$). The study was approved by the institutional review board at ASU (STUDY00011266) and the University of Massachusetts Lowell (20-057-YAN-XPD).

Sensor setup. Twelve IR motion capture cameras (Vicon, Oxford, UK) and sixteen reflective markers were used to build a lower-limb model for each subject via Vicon Nexus 2.8. Using this model, 3-D joint angles (hip, knee, and ankle) and pelvic position and orientation were estimated. Four extra markers were attached to a plate that rigidly houses the IMU, which is used to build a rigid body model in Nexus to

Table 4.1. Noise characteristics

Measurement type	Noise SD (proposed InEKF)	Noise SD (existing InEKF)
Linear acceleration	0.2 m/s^2	0.2 m/s^2
Angular velocity	0.05 rad/s	0.05 rad/s
Kinematics measurement	0.5 m/s	0.1 m
Placement offset ($\Delta\mathbf{p}$, $\Delta\mathbf{R}$)	(0.05 m, 0.05 rad)	NA
Contact velocity	NA	0.05 m/s

acquire the ground-truth pose of the IMU/body frame. The IMU (BNO085, New York, NY) was placed on the back of the subject close to the pelvis. The accelerometer and gyroscope data were recorded using a data acquisition board (Arduino UNO, Boston, MA). The data were later synchronized with the motion-captured data using a trigger signal from the Vicon system. The experiments were done on an instrumented dual-belt treadmill equipped with force plates (Bertec Corp., Columbus, OH) that record ground contact forces.

Movement types. Each participant was asked to perform three types of motion: squatting, ladder climbing, and rolling-foot walking (see the right figure of Fig. 4.2). Two trials were performed for each motion type, each for 1.5 minutes.

4.3.2 Data Processing

Filters compared. The proposed filter is compared with a state-of-the-art InEKF (Hartley et al. 2020). The existing InEKF was originally designed for a Cassie series bipedal robot. In the existing filter, the IMU and measurement frames are well aligned. The state variables of the existing filter are the IMU orientation, velocity, position, and the contact foot position, all expressed in the world frame. The kinematic measurements of the existing filter are the contact foot positions with respect to the

measurement frame expressed in the measurement frame. Unlike the proposed filter, the measurement model of the existing filter has an invariant observation form, which, in combination with the exponential form of the measurement update, renders the deterministic error update equation to be independent of state trajectories (Barrau and Bonnabel 2016). Also, the kinematic measurements of the existing filter have smaller noises since the Cassie series bipedal robot uses highly accurate leg encoders to formulate the forward kinematics chain. With a human subject, however, the IMU and measurement frames are not aligned, and the kinematics measurements have relatively large noises.

Covariance settings. The noise characteristics for both filters are shown in Table 4.1. The noise standard deviations of the linear acceleration and angular velocity are obtained from the IMU specifications provided by the manufacturer. To reach the better performance of both filters, these two noise standard deviations are slightly tuned around the nominal values. Note that covariance tuning is also reported in other InEKF designs (Brossard, Barrau, and Bonnabel 2020). It should also be noted that since the two filters use different measurement models ($\mathbf{d}^M$ is used as the measurement in Hartley et al. 2020), different noise covariance values are used for the two filters. Moreover, the proposed filter considers the noise of the IMU angular velocity in the kinematics measurement noise term, while the same covariances are used for the common parameters of the two filters (linear acceleration and angular velocity). During the tuning process, it was observed that the performance of the proposed filter does not vary significantly within a relatively wide range of parameters (e.g., the covariances matrices). Yet, the estimation performance degrades when the covariances are far from the optimal values. The placement offset noises are only used in the proposed filter. Given that the placement offsets are relatively constant, the

noise standard deviations of the placement offsets are set as small values. The contact velocity noise is only accounted for in the existing filter, which is induced by contact foot slippage.

Initial estimation errors. To demonstrate the accuracy and convergence rate of both filters under large estimation errors, a relatively wide range of initial estimation errors of the IMU/body velocity and orientation are used. They are respectively chosen to be uniformly within $[-1, 1]$ m/s and $[-20, 20]$ degrees across 50 trials.

Filter performance indicators. To evaluate the filter performance, we choose to use three common indicators (Barrau and Bonnabel 2016; Hartley et al. 2020; Teng, Mueller, and Sreenath 2021): (a) computation time (for assessing the filter's capability in real-time implementation); (b) convergence rate (for evaluating how rapidly the estimation error reaches the steady state); and (c) estimation accuracy (for testing the accuracy during transient and steady-state periods).

4.3.3 Results

To illustrate the accuracy of the forward kinematics-based measurement (4.5), Fig. 4.3 compares it with its reference obtained from the motion capture system. As noted in Sec. 1, the measurement associated with a given leg is fed into the update step of the filter only when the leg is in contact with the ground (highlighted by yellow shaded areas in Fig. 4.3) .

Table 4.2 displays the average root mean square error (RMSE) values of different motions and different kinematics measurements for all three subjects. During the initial period, subjects are standing still, and the estimation algorithms just start.

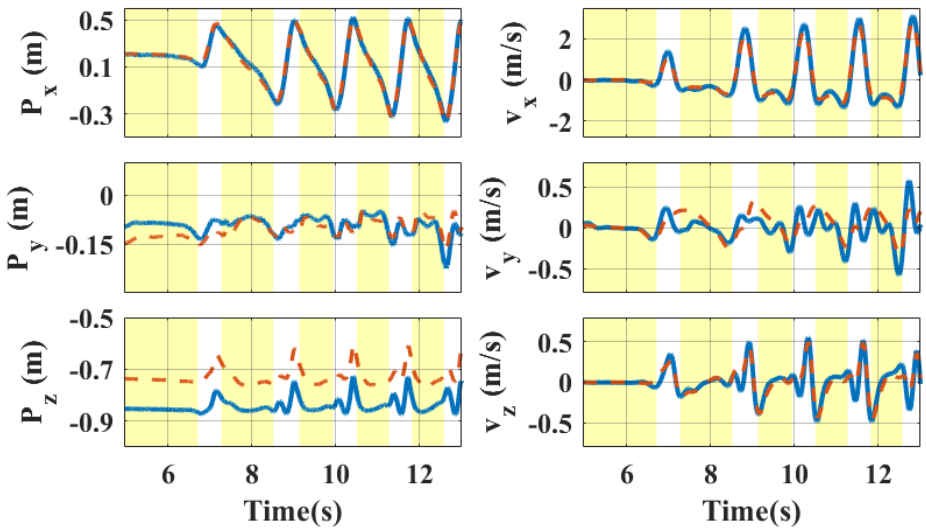

Figure 4.3. Relative position (left) and velocity (right) of the right toe in the measurement/pelvis frame during one of the rolling-foot walking trials, obtained by using joint angle readings and forward kinematics (blue, solid line) and by using the marker positions of the toe and measurement plate returned by motion capture system (red, dashed line). The yellow shaded areas indicate the periods during which the right foot contacts the ground.

During the steady-state motion period, subjects are doing continuous movements with different motion types. The average RMSE values of the variable "V" are obtained from the estimated IMU velocity of all three axes for all subjects with the same motion type, while the average RMSE values of the variable "O" are obtained from the estimated IMU orientation of roll and pitch angles for all subjects with the same motion type. The "FK" portion shows the RMSE values of the estimation results with the forward kinematics measurements in (4.5), and the "3-D vector" part indicates the RMSE values of the estimation results under the 3-D vector kinematics measurements in (4.7).

Figure 4.4 shows the comparison of the IMU velocity and orientation estimation results of one subject with forward kinematics measurement under different motions and filters but the same sensor data set. The grey-shaded and white backgrounds indicate the initial period and steady-state motion period, respectively.

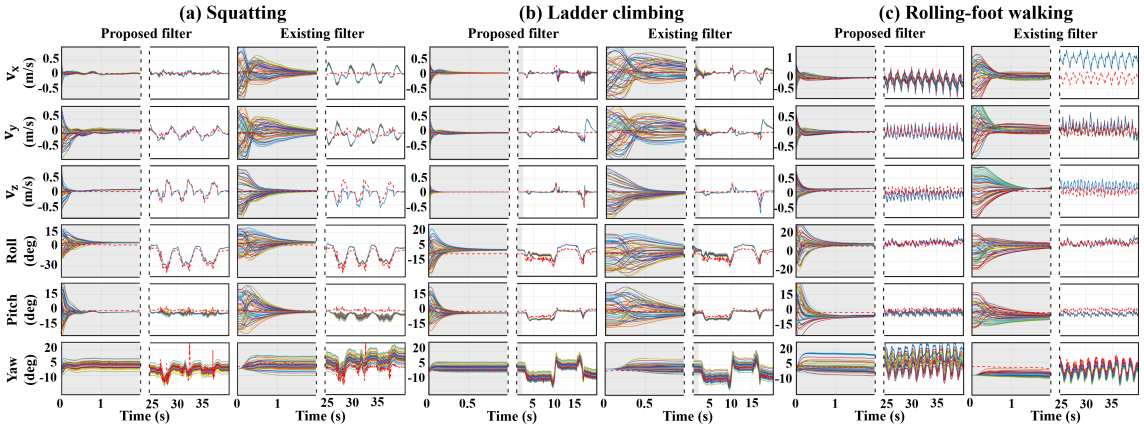

Figure 4.4. Estimation results of the velocity and orientation of subject 2's body/IMU frame during (a) squatting motion, (b) ladder climbing, and (c) rolling-foot walking under the proposed and existing filters. The same sensor data set is used, including the raw data returned by the IMU at the trunk and the leg joint angle data provided by the motion caption system. The solid lines are the state estimates corresponding to different initial errors. The red, dashed lines are the ground truth. The gray and white backgrounds indicate the periods of initial and steady-state movement, respectively. The x-, y-, and z-directions are the lateral, forward and vertical directions, respectively.

Computational time. MATLAB R2020b was used to process the experimental data sets with both filters. The average computational time for one filter loop of the proposed filter is about 0.6 ms, and the average computational time for one filter loop of the existing filter is about 3 ms. Both are sufficiently fast for typical human movement monitoring.

Convergence rate. By investigating the initial period of the estimation results figure (Fig. 4.4) and the RMSEs table (Table 4.2), it is obvious that the proposed filter converges faster than the existing filter, driving the estimation error close to the ground truth within 0.6 s.

Estimation accuracy. The results during the steady-state periods in both Fig. 4.4 and Table 4.2 indicate that under both filters the estimated roll and pitch angles of the IMU converge to a small neighborhood around their ground truth. Yet, the yaw angle of the IMU is not observable under both filters. Also, the overall accuracy of the IMU velocity estimation under the proposed filter is better than the existing filter.

Table 4.2. Average RMSE values for the three participants and motions. V and O refer to the body/IMU velocity and orientation.

Time period	Motion type	Variable	FK		3-D vector	
			Proposed InEKF	Existing InEKF	Proposed InEKF	Existing InEKF
Initial	Stand	V (m/s)	0.062	0.226	0.063	0.210
		O (deg)	4.484	6.616	4.737	6.643
Steady state	Squat	V (m/s)	0.067	0.147	0.041	0.152
		O (deg)	4.745	4.909	4.832	4.727
	Roll.-foot	V (m/s)	0.237	0.467	0.103	0.442
		O (deg)	2.909	2.984	2.685	2.838
	Ladder climb.	V (m/s)	0.072	0.135	0.047	0.14
		O (deg)	3.13	3.11	3.12	3.199

4.3.4 Discussion

This subsection discusses the performance of the proposed InEKF with respect to the existing InEKF.

Forward kinematics vs. 3-D vector measurement. Incorporating forward kinematics measurement (i.e., (4.5)) introduces considerable uncertainties to the filtering system for human motion estimation (as depicted in Fig. 4.3). The uncertainties in the forward kinematics measurement could be induced by various sources, such as imperfect marker placement, shift of markers on skin or garment, inaccurate parameters (e.g., body segment lengths) and structure of human kinematics chain. These factors lead to the less accurate estimation of both body velocity and orientation compared to directly using the 3-D vector measurement, for the proposed InEKF, as shown in Table 4.2. Yet, the proposed filter with forward kinematics measurement has a better overall performance compared with the existing filter. This highlights the importance

of modeling the sensor placement offset in ensuring effective filtering under relatively less accurate forward kinematics measurement.

Convergence rate. As discussed in Sec. 4.3.2, the process and measurement covariance matrices were well-tuned for both filters. While the higher convergence rate can be a result of the explicit treatment of sensor placement offset in the proposed filter, additional human studies are needed to confirm that covariance matrices used in the two filters match the actual sensor characteristics and ensure a fair comparison.

Steady-state estimation. From the average RMSE results in Table 4.2, we can see that the proposed filter reaches a higher steady-state accuracy in the velocity estimation compared with the existing filter while they achieve similar accuracy in orientation estimation, given properly tuned noise covariance (and kinematics parameters for the forward kinematics based measurement model). During the tuning process, it was observed that both filters had better performance with relatively small angular velocity noise covariance. This indicates that orientation estimation relied more on the process model for the steady-state period during which the large initial errors have already been corrected using the measurement model. Therefore, both the proposed and existing InEKFs show almost similar performance in orientation estimation during the steady-state period. Nonetheless, velocity estimation is relatively more dependent on the measurements. Therefore, the proposed filter has a superior performance in steady-state velocity estimation as it benefits from more accurate measurement updates thanks to its offset treatment.

Different motion estimation. From Table. 4.2, it is evident that RMSE of the velocity estimations in rolling-foot walking is higher compared to the other two motion types. Walking is a more dynamic task compared to the other two, making the estimation more challenging. The static-foot assumption is more likely to be

violated (**gronqvist1995mechanisms**) during foot-rolling. Specifically, in rolling-foot walking, we observed relatively high errors in the y-direction of forward kinematic measurement. When large errors are introduced in the measurement, it can also impact the offset estimation, weakening the advantage of the proposed InEKF with respect to the existing one. Since the existing filter does not consider the placement offsets, its velocity estimates have large final errors as shown in Fig. 4.4.

Limitations. One notable limitation of this work is the modeling of the IMU offset dynamics. It is assumed that the IMU offset has a slowly time-varying dynamics, which can be valid under some activities such as slow walking and stair climbing. However, under more aggressive movements such as running, the IMU might have large and sudden shifts relative to the body, which will violate this assumption. Other limitations include the practical difficulty in obtaining accurate joint angles for the forward kinematic model and the validity of the assumption of the static foot-ground contact point (which was discussed through our results).

4.4 Conclusion

This paper introduced a right-invariant extended Kalman filter that explicitly considered the offsets between the IMU frame and the measurement frame. The proposed filter design is an "imperfect" invariant extended Kalman filter since the process model satisfied the group affine property but the measurement model does not have the right-invariant observation form. As demonstrated by experimental results among different subjects and motion types, the proposed filter has a low computational cost, and with properly tuned parameters (e.g., noise covariance and leg kinematics), it improves the convergence rate and estimation accuracy of the

IMU velocity estimation compared with the existing filter. This is largely because the IMU offset is treated as a noise source in the original filter while the proposed filter explicitly models and estimates it. The observability analysis shows that the IMU positions and the rotation about the gravity vector were not observable whereas the IMU velocities and the rotations about the other two axes were observable. The observability analysis matched with the experimental results.

In future work, a more accurate forward kinematics model (e.g., obtained based on online estimation of limb lengths and other kinematics parameters) and explicitly treating IMU biases are needed to improve the filter performance. Also, it is time-consuming to tune the process and measurement covariances for different subjects and motion types. A data-driven learning algorithm may be useful for solving this issue. Finally, the forward kinematics measurement in this study assumes a fixed contact point on the foot, which may not be valid for movements involving a nonstationary contact point (e.g., during rolling-foot walking) and thus needs to be relaxed for a more realistic forward kinematics model.

Chapter 5

LEARNING POST-STROKE GAIT TRAINING STRATEGIES BY MODELING PATIENT-THERAPIST INTERACTION

Each year, among stroke survivors in the US, about 200,000 people are affected by lower-extremity hemiparesis, which results in impaired walking (Benjamin et al. 2018; Kelly-Hayes et al. 2003). Walking deficits are common in more than 80% of stroke survivors (Duncan et al. 2005).

Studies have shown that knee muscle strength is a moderate to strong predictor of the quality of walking in individuals with chronic mild to moderate post-stroke hemiparesis (Flansbjer, Downham, and Lexell 2006). Knee instability (buckling) and hyper-extension are among the common gait disorders in stroke patients (O'Connor et al. 2016; Jaffer et al. 2011). It is correlated with the weakness of the quadriceps which leads to the loss of control of the knee extensors during the stance phase and puts the knee at risk of collapsing under weight (Gillen 2015). To help post-stroke individuals regain their normal walking ability, gait rehabilitative therapy is currently provided by physical therapists. Successful rehabilitation of patients with a neurological injury includes recovery of normal movement using the concepts of motor learning (Lazaro, Reina-Guerra, and Quiben 2019). The overall goal of therapeutic intervention during gait is to facilitate normal kinematics and muscle activation throughout each phase of the cycle. This one-to-one physical therapy is effective but is time-consuming, costly, and physically demanding. In order to make gait therapy easily accessible and more affordable to patients for longer periods of time, worldwide effort has been put into developing robot-aided therapy.

Despite considerable progress in sensor and robot-aided gait rehabilitation, the lack of intelligent control approaches prevents assistive robots from clinical deployment. Previous studies have suggested that modeling and identifying human-human sensorimotor interactions have led to the development of robots that physically interact and move with humans in an intuitive and efficient manner (Sawers and Ting 2014). Physical rehabilitation is a form of Human-Human haptic interaction in which the goal of PT is to train the patient to improve their motor performance. However, in the context of rehabilitation robotics, there is no widely accepted framework to define Human-Human interaction (HHI) (Sawers and Ting 2014). This is mainly because of the lack of enough studies that have collected and modeled the haptic interactions between PTs and patients to reveal how those forces should be applied to encourage motor skill learning. By capturing and analyzing the assistance from physical therapists, which is based on their clinical experience and patient's gait observation, we can improve robot-aided gait training and rehabilitation.

In this work, a custom-made wearable sensor system is developed to measure the interaction forces and leg kinematics during post-stroke gait training of hemiparetic patients with moderate weakness in their quadriceps muscles. The collected data is then used to characterize the patient's gait patterns and the corresponding assistive torques applied by the PTs. The results offer important insights into how gait rehabilitation principles when used in tandem with clinical experience and patient gait observations, can lead to better timing and magnitude of assistance. To achieve this, an learning from demonstration (LfD)-based approach to virtual impedance control is selected as the mechanism for reproducing PT assistance and incorporating these clinical insights.

5.1 Background: Hemi-paretic Post-stroke Rehabilitation: Knee Stability and Weight-Shifting Facilitation

Patients with hemiparesis often present with a slow, asymmetrical gait pattern which may be due to knee instability and inadequate weight shifting. During the assessment, knee instability is often suspected when weakness in the hamstring or quadricep muscles and/or proprioceptive deficits are identified (Gillen 2015). Knee instability is confirmed when the therapist evaluates the patient in standing and performs a comprehensive gait assessment. This assessment commonly includes manual muscle testing (MMT) and the Modified Ashworth scale (MAS) of the lower extremity. Hemi-paretic gait deviations are typically observed in patients who present with decreased lower extremity strength and possible proprioceptive deficits. Knee hyperextension may be observed during initial loading due to the lack of control of the quadriceps muscles. At mid-stance, overall muscle weakness can cause increased hip and knee flexion which may be observed as knee buckling or hyper-extension. During terminal stance, knee hyperextension may occur if the hamstrings are too weak to counteract the quadriceps to slow down knee extension and the knee may quickly hyper-extend.

Patients with hemiparesis may compensate for weakness at different joints during the gait cycle to increase stability. During the stance phase, two common compensations to prevent knee hyperextension or buckling are limiting stance time by decreasing the weight shifting on the involved extremity or maintaining excessive knee flexion. These gait compensations often result in an asymmetrical gait pattern with decreased step length on the contralateral side and altered joint kinematics throughout the lower extremity (Gillen 2015; Li, Francisco, and Zhou 2018). Over time, compensatory

movement patterns may reinforce abnormal tone and movement of the involved side (Lennon 2001).

When gait training a hemiparetic patient, the stance phase is key to facilitating a symmetrical gait pattern since increased stance time on the involved side allows the patient time to take a normal step with the non-involved lower extremity. Functional stance is achieved when appropriate weight is shifted onto the involved lower extremity while stabilizing the knee which may require manual support and facilitation of quadriceps or hamstrings. Timing is critical and facilitation at the pelvis, hip, and knee is performed as needed to achieve proper joint kinematics during each phase of the stance. Repetition of proper gait mechanics is needed for motor learning to occur which is important as learning is required for neural adaptation (Lazaro, Reina-Guerra, and Quiben 2019).

5.2 Methods

5.2.1 Data Collection System

To capture the interaction dynamics between the physical therapist (PT) and the patient, we designed a wearable sensor system to record the following data: Exerted force by the PT (haptic interaction), knee joint kinematics, and ground reaction forces at the affected side.

During our gait therapy sessions, the PT touches and exerts a force on different areas of the body. However to stabilize the knee motion during weight-shifting and prevent knee buckling, the assistive forces are mostly focused on two areas: anterior upper and lower knee (where the force sensors are placed in Fig. 5.1). Therefore we

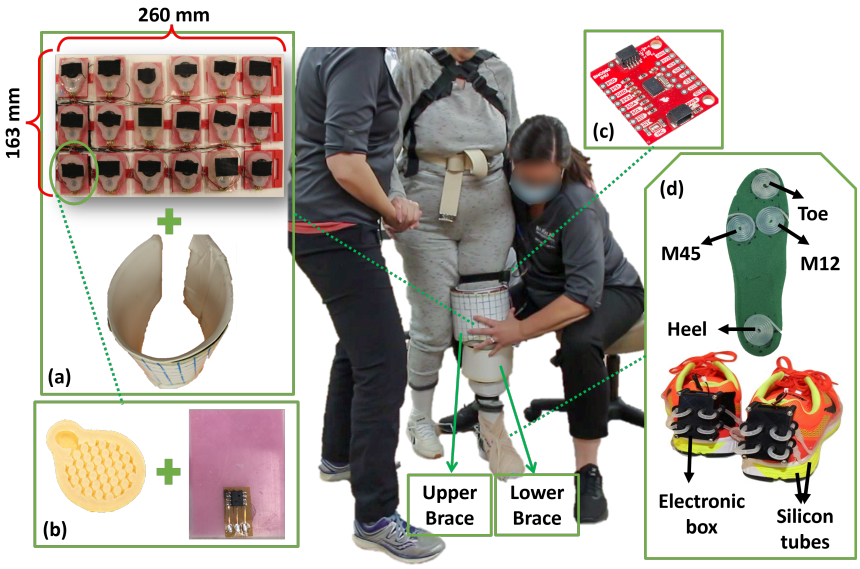

Figure 5.1. The custom-designed wearable sensor system during a gait therapy session. (a) Components of the soft force sensor (upper and lower) braces, consisting of an array of pressure sensing elements held by the flexible 3D printed TPU part (top), connected to the soft curved outer shell (bottom), making it easy to fit a patient leg with different sizes (the two sensor braces weigh about 900 g in total). (b) Components of the pressure sensing unit, air-filled silicon pad (left), enclosing the absolute pressure sensor (right). (C) IMU sensors are placed at the shank and thigh. (d) Smart Shoes consist of coiled silicon tubes placed at four points of contact in the insole (top) and the electronic box containing the pressure sensors, microcontroller, and WiFi module (bottom).

designed two separate soft force sensor braces for each part, intending to capture both the magnitude and distribution of the force with acceptable resolution and accuracy in a non-intrusive way to both the patient's and PT's movements. Each brace embodies a flexible pressure sensor matrix consisting of arrays (3×6 and 2×5 for the upper and lower knee, respectively) of air pressure sensors enclosed by air-filled silicon pads with an elastomeric pillar array (Fig.5.1-b), inspired by (Kim, Shin, and Kong 2018). The force is measured by the increase in the air pressure caused by pillar compression. This design allows for a compact structure by introducing a high measured force-to-volume ratio and is shown to have a linear and repeatable pressure-force behavior (Kim, Shin, and Kong 2018). Each sensor is calibrated separately using an Instron machine, and a linear model is considered between measured force (N) and sensor output, mV.

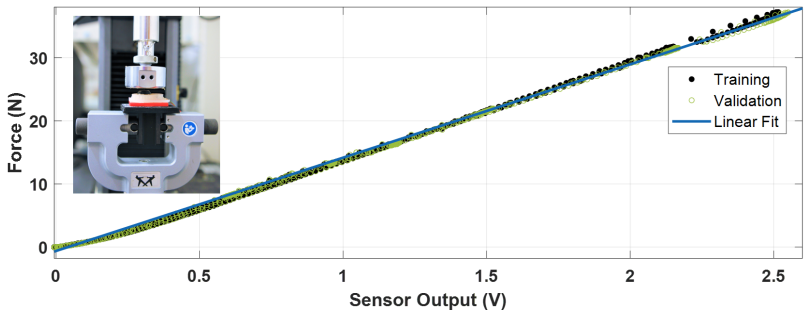

Figure 5.2. Calibration results for one of the cells of the force sensor array. This linear fit model has been obtained and validated with the training and validation sets separately during two full cycles of loading and unloading at the rate of 1.5 N/s.

Figure 5.2 Shows the force sensor calibration process for one cell of the sensor array using a universal testing machine (Instron 5944, Instron Corp., UK). A linear fit model has been obtained for each sensor separately, similar to Figure 5.2. The average RMSE of validation sets for all the sensors was 0.92 N. The maximum error among all sensor cells was 1.91 N.

In Fig. 5.3 we are showing a sample of the raw data for all the cells of the soft force sensor array (upper brace) during one of the patient's gait training sessions (PT1-P6). The raw measurements are voltage changes caused by the change of the pressure inside each chamber due to the applied force by the PT. These measurements were filtered using a second-order Butterworth low-pass filter with a 10 Hz cut-off frequency. It can be observed that the PT's force was mostly applied on the middle part (sensors 3, 9, and 16 in Fig. 5.3). The negative values show the decrease of air pressure in the chamber, which corresponds to the sensors getting pulled as the other sensors are pressed. These negative values are neglected and considered to be zero. This data was then converted to force values using the linear model obtained in the calibration process for each cell of the sensor array (as discussed in Fig. 5.2).

The knee joint kinematics were captured using the BNO085 IMU sensor (SparkFun

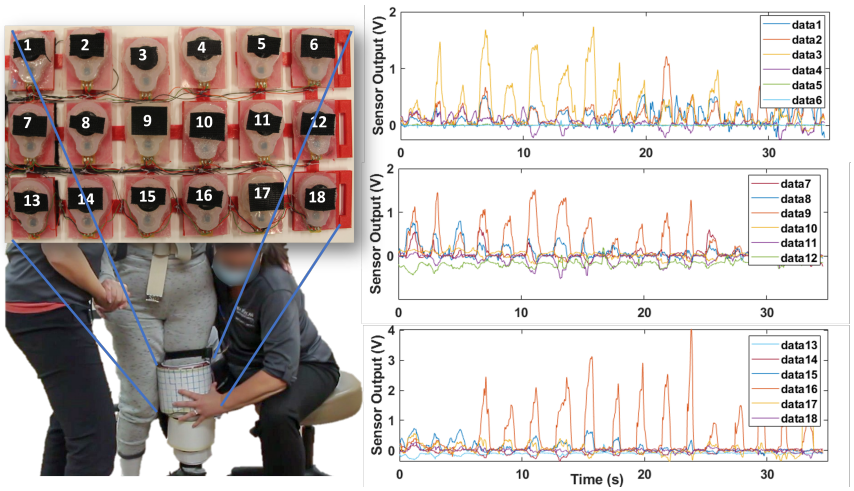

Figure 5.3. A sample data of the raw measurements of the 18 cells of the soft force sensor array (upper brace) in the PT1-P6 session. Each plot is corresponding to one of the rows, and each line represents one of the cells, as labeled. The projection (location) of the sensors on the patient's leg is depicted.

Electronics, CO). The Smart-shoe (Zhang, Tomizuka, and Byl 2016) was used to capture the ground reaction forces (GRFs) of the affected side, in real-time (Fig.5.1). All the data were collected by a host microcontroller (Intel Edison UP Board, CA), which along with a $12V$ battery and PCB boards were embodied on a backpack worn by the patient. The backpack weighed less than $500g$.

The real-time feedback (rating) of PTs on each gait cycle was also collected. While one of the PTs is facilitating the patient, she would give the vocal rating in terms of "Good", "ok" and "bad" for each gait cycle, and the other PT would push the button associated with that rating, which is being collected by the host micro-controller. Based on the time index that the data was collected, we could attribute each rating to the corresponding gait cycle.

5.2.2 Experimental Procedure

5.2.2.1 Patient Recruitment

Post-stroke patients with hemiparetic gait, specifically with weakness in the quadriceps leading to knee instability, were recruited at Barrow Neurological Institute (BNI) in Phoenix, Arizona. Participants had to be able to ambulate with minimal assistance or less for up to 5 minutes with or without the use of a single-point cane and/or ankle foot orthosis (AFO). Participants with manual muscle testing (MMT) scores of knee flexion/extension less than 2+ were excluded from the study. Participants with modified Ashworth of hemiparetic lower extremity less than or equal to 1+, and with flexion contracture that cannot extend the knee beyond 10° were also excluded from the study. These criteria was set to allow for recruiting patients with less impairment, so the PTs' assistance would focus on correcting certain gait abnormalities related to knee instability. Before enrollment, a series of physical assessments were performed by the PTs to ensure that all the criteria were met. The protocol of the study was reviewed and approved by the institutional review board at BNI (protocol number 19-500-271-70-19).

Initially, seven patients were recruited, out of which four patients' data are used in this study. Data from two patients were discarded as the PT assistance was not significant due to their relatively functional and independent gait. Thus the inclusion/exclusion criteria was adjusted accordingly to recruit patients with higher impairment levels. Another patient's data collection was unsuccessful because of technical difficulties with the wearable sensor system during the gait training session.

Anthropomorphic information and the knee and hip flexion/extension MMT scores of the four final patients are given in Table 5.1.

5.2.2.2 Experimental Procedure

The BNI team conducted participant enrollment after which a two-hour data collection session was scheduled with participants that consented. Each data collection session consisted of three sub-sessions: 1) no training (NT), 2) training by the first PT (PT1), and 3) training by the second PT (PT2). We collected two PTs' data in each session to study the similarities and differences in their gait training strategies.

At the beginning of each session, patients first put on the wearable sensors with the help of the PTs. If the patient wore an AFO, it was removed and replaced by an ace wrap to prevent foot drop. In the first NT sub-session, the patients walked by themselves for three minutes, with minimal assistance from the PT only when needed for safety. Minimal assistance in this context is defined as assisting with less than 25% of the weight support and balancing, through pelvis and upper-body assistance. After the first sub-session was completed, the patient rested for at least five minutes depending on patient readiness. Next, the training with the PT1 began, in which the PT, sitting on a wheeled stool, facilitated the upper knee motion of the paretic side to support weight-shifting and knee stability. These two sub-sessions also lasted for three minutes each and consisted of multiple 10-15 meter laps, at the end of which each patient would turn, and stay steady and straight for 10 seconds (to help with initializing IMUs and the force sensor). Real-time feedback for the quality of each gait cycle from PTs was collected. After resting for at least five minutes, the other training sub-session was performed by PT2, similar to the previous sub-session. To assess if

Table 5.1. Patient Anthropometric and MMT Data

	Patient ID (P#)			
Patient Information	3	5	6	7
MW Group	HMW	LMW	HMW	LMW
Anthropometry				
Gender	F	F	F	F
Age	27	44	68	28
Weight (kg)	64	76	83	53
Height (cm)	160	170	150	160
Paretic Side	R	L	L	R
MMT				
Knee Flexion	2+	4-	3+	4+
Knee Extension	4	4-	4-	4
Hip Flexion	4	4-	3	4
Hip Extension	2+	4	3+	4

the data collection system interfered with patient kinematics or PT assistance, which would invalidate the data, both the patient and PT filled out a survey expressing their opinion on the training session and data collection system. None of the trials indicated significant interference from the system.

5.2.3 Initial Data Processing

All sensor data were captured on the host PC. Initially, data were collected with different frequencies. In the post-processing, all data were synchronized and re-sampled to 75 Hz. Next, each sub-session data was segmented into laps. For each lap, the following variables were extracted:

5.2.3.1 Gait sub-phases and percentage

using the four readings from Smart-shoe, it is possible to segment the gait into six sub-phases: heel-strike (HS), loading-response (LR), mid-stance (MS), terminal stance (TS) or heel-rise, pre-swing (PS) or toe-off, and swing. The first five sub-phases are the stance phase. This segmenting is based on which insole sensors are activated, based on a Fuzzy rule base for gait analysis developed in (Kong and Tomizuka 2009). By employing these sub-phases we can segment the data into individual gait cycles, and also time-normalize each cycle into separate gait (or stance phase) percentages. Therefore stance time and stance phase % of each cycle can be extracted.

5.2.3.2 Vertical GRFs (Weight-shift)

Combining the four sensor readings of the Smart-shoes, we can get the total vertical GRFs. Normalizing this value by the weight of each patient, the % of weight shifted on the paretic side can be calculated at each time step. Although the values are not directly weight shift, they are representative

5.2.3.3 Joint Kinematics

The thigh and limb kinematics were calculated using the quaternion values q retrieved from the BNO080 IMUs that were attached to their respective limbs. Before each lap, the therapist was instructed to place the knee on the paretic side at full extension for a reference frame q_0 that compensated for IMU sensor drift, initial attachment, and shifting throughout the session. The rotation of the thigh and shank

were calculated as a rotational displacement Δq from these initial reference frames by applying the inverse quaternion of the reference frame to the raw quaternion values retrieved $\Delta q = q q_0^{-1}$. The joint angles were then calculated by applying the rotation Δq to the unit vector $v_0 = [1, 0, 0]$ and projecting the rotated vector onto the sagittal plane.

The resulting angular displacement in the sagittal plane mitigates any prolonged sensor drift or shifting and is invariant of initial attachment orientation. The main limitation of this approach is establishing the reference frame. When instructed to place the patient's knee in full extension, it was assumed that the patient's knee was at 0° flexion. However, the therapist could have placed the knee in hyperextension or been unable to induce full extension for whatever reason. Therefore, the limb and joint rotations may have an error of $\epsilon = \pm 5°$.

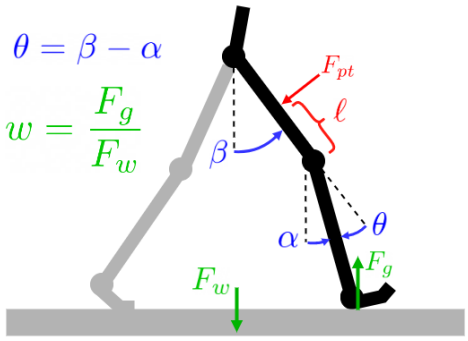

Figure 5.4. The kinematics diagram shows the relevant kinematic variables for knee x^K, shank x^{Sh}, and thigh x^{Th} angle displacements. It also shows the sagittal force applied by the therapist F_{pt}. The ground reaction force F_g is applied at the foot (paretic side) and is used to calculate percent weight-shift x^{WS} by scaling F_g by the patient's weight F_w.

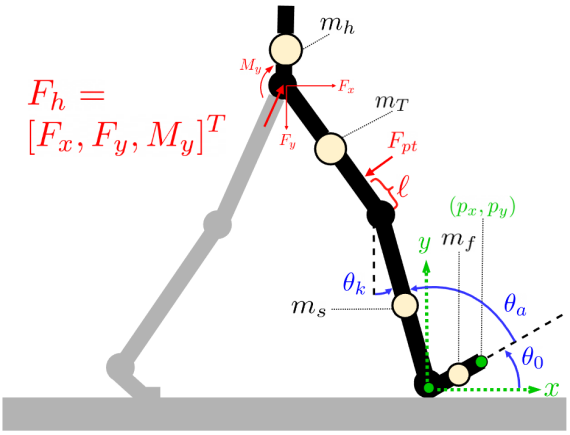

Figure 5.5. The biped model used for modeling human gait dynamics. m_f, m_s, m_t, and m_h represent foot, shank, thigh, and torso lumped masses. θ_0 is the foot angle with the ground, (p_x, p_y) are the coordinate of the toe in the IRF, and θ_a and θ_k are the ankle angle and knee angle, respectively. In this model, the torso and hip are lumped together as a single mass (i.e., only one hip joint) for simplicity, which will not affect the torque calculation.

5.2.3.4 Assistive Knee Torque

Here, we aim to calculate the external actuation torque components that can be applied at the joints so we will have an equivalent human dynamic system with the one where the only external actuation is the therapists force F_{pt} (Fig. 5.5). We show that we only need external knee and ankle joint torque components, where the external knee torque component can be calculated as $\tau = \ell|F_{pt}|$, and the ankle torque component τ_a is coupled with the knee torque through kinematic parameters and can be calculated given τ, ankle and knee angles, and the shank length.

We follow the similar comprehensive biped model in (Lv 2018), which originated at (Gregg et al. 2014). We model the patient paretic side in the stance phase as a kinematic chain with respect to an inertial reference frame (IRF) defined at the stance heel or stance toe, depending on the phase of the stance. The dynamics of the system

with therapist actuation can be written as:

$$\begin{aligned} M(q)\ddot{q} + C(q,\dot{q})\dot{q} + N(q) + A(q)^T\lambda = \\ B(q)v + J_l(q)^T F_{pt} + J_h(q)^T F_h \end{aligned} \tag{5.1}$$

where $q = (p_x, p_y, \theta_0, \theta_a, \theta_k)$ are the variables defining the full configuration the leg. It must be noted that the hip is considered as a 1-DoF joint, and the other leg is replaced by the interaction force (and torque) F_h. The actuation of the hip is included within this interaction force. $M(q)$, $C(q,\dot{q})$, $N(q)$ are the inertial/mass, Coriolis/centrifugal, and gravitational force matrices, respectively. $J_l(q)^T$ and $J_h(q)^T$ are the body Jacobian matrices mapping the F_h and F_{pt} to the body dynamics. Note since F_{pt} is a 2D force (no torque component), J_l is the translational Jacobian (2×5 matrix). v is the human joint input (torque) vector (ankle and knee), and $B(q)$ is $[0_{2\times3}\ I_{2\times2}]^T$ is the matrix mapping the human joint torques to the body dynamics. $A(q)$ is the matrix modeling the contact constraints (three different contact conditions: heel contact, foot-flat, and toe contact). λ is the Lagrange multiplier used to calculate the contact forces. For more details see (Lv 2018).

Now consider the same body, with therapist force being replaced by mass-less actuators at the knee and ankle joints (represented by the vector $u_e = \begin{bmatrix} \tau_a & \tau \end{bmatrix}^T$):

$$\begin{aligned} M(q)\ddot{q} + C(q,\dot{q})\dot{q} + N(q) + A(q)^T\lambda_e = \\ B(q)v + B(q)u_e + J_h(q)^T F_h \end{aligned} \tag{5.2}$$

It must be noted that we want the same kinematics and dynamics for the human under both actuation in (5.1) and (5.2), therefore we consider the same joint kinematics, human joint inputs, and the same interaction forces/torques from the other leg

(composed of 2D forces F_x and F_y, and the normal toque component M_y). λ_e is the corresponding ground reaction force vector to the new actuation. For our matching condition to be met, the following must hold true:

$$B(q)u_e - A(q)^T\lambda_e = J_l(q)^T F_{pt} - A(q)^T\lambda. \tag{5.3}$$

According to (Lv 2018), the ground reaction vector can be written as:

$$\begin{aligned}
&\lambda = \hat{\lambda} + \tilde{\lambda}\tau, \\
&\hat{\lambda} = W\dot{A}\dot{q} - AM^{-1}(C\dot{q} + N), \\
&\tilde{\lambda} = WAM^{-1}B, \text{ where } W = (AM^{-1}A^T)^{-1}.
\end{aligned}$$

Here, τ is the vector of total inputs to the system. It can be seen that $\hat{\lambda}$ and $\tilde{\lambda}$ is similar for both systems (Lv 2018). Having the same human inputs, (5.3) can be simplified to:

$$(-\tilde{\lambda} + I_{5\times5})Bu_e = (-\tilde{\lambda} + I)J_l(q)^T F_{pt} \tag{5.4}$$

It must be noted that in the heel contact and toe contact phase, the human biped model in (5.2) is underactuated (Lv 2018), therefore it is not possible to make (5.4) hold true. However, it was observed that the majority of therapist force is applied during the foot-flat (loading response + mid-stance) phase. Therefore, we only consider the foot-flat phase, where regarding the one additional holonomic constraint of the foot is flat, the system in (5.2) can be considered as fully actuated and (5.4) will be

true. It can be shown that $-\tilde{\lambda} + I$ will have the form:

$$A_{foot-flat} = [I_{3\times3},\ 0_{3\times2}] \Longrightarrow \tilde{\lambda} = \begin{bmatrix} 0_{3\times3} & -\tilde{\lambda}_k \\ 0_{2\times3} & I_{2\times2}, \end{bmatrix} \tag{5.5}$$

where $\tilde{\lambda}_k$ is the 3×2 sub-matrix that depends on the inertia/mass matrix M and its inverse. Plugging (5.5) into (5.4) will yield:

$$\begin{bmatrix} -\tilde{\lambda}_k u_e \\ u_e \end{bmatrix} = \begin{bmatrix} -\tilde{\lambda}_k [J_l^T F_{pt}]_{4:5} \\ [J_l^T F_{pt}]_{4:5} \end{bmatrix} \tag{5.6}$$

where $[\cdot]_{4:5}$ refers to the 4th and 5th elements of the column vector $[\cdot]$. Therefore, we need $u_e = [J_l^T F_{pt}]_{4:5}$ to hold. As we know, F_{pt} is always perpendicular to the thigh so it has the form $F_{pt} = |F_{pt}| \begin{bmatrix} -cos(\theta_{pt}) & -sin(\theta_{pt}) \end{bmatrix}^T$, where $\theta_{pt} = \theta_k + \theta_a + \theta_0 - \pi/2$. Computing this Jacobian using the standard methods, we can compute the actuator's input u_e that will replicate the PT input to the system. Considering that at flat-foot $\theta_0 = 0$, we have:

$$\begin{aligned} u_e &= \begin{bmatrix} \tau \\ \tau_a \end{bmatrix} = [J_l^T F_{pt}]_{4:5} \implies \\ u_e &= \begin{bmatrix} |F_{pt}|l \\ |F_{pt}|l + |F_{pt}|l_s(sin(\theta_a)sin(\theta_{ak}) + cos(\theta_a)cos(\theta_{ak})) \end{bmatrix} \end{aligned} \tag{5.7}$$

where $\theta_{ak} = \theta_a + \theta_k$. It is clear that by learning and modeling τ, we can also reproduce τ_a given θ_a, θ_k, l_s and l.

Remarks: i) As shown, in order to actuate the leg similarly to the therapist,

there is no need to directly actuate the hip when knee and ankle joint actuation can suffice. ii) Even if we consider the hip and torso as separate joints (2D hip joint), the structure of J_l will remain the same and the same conclusions can be drawn. iii) When considering the ace wrap that connects the patients' foot to the heel, the foot rotation in heel contact and toe contact phases are restricted and we can assume the model is not underactuated in these phases anymore, therefore the same result in (5.7) can be applied to heel contact and toe contact in cases where we have considerable force from the PT in these phases.

During the gait therapy sessions, there were very few instances that the PTs were exerting force on the lower-knee force sensor. Therefore we only considered the forces on the upper-knee force sensor. Using the sensor matrices, we are able to calculate both the magnitude and CoP of the exerted force. Knowing approximately where the sensor is located from the knee joint, we can calculate the Anterior-Posterior component of the interaction torque applied to the knee joint. It is assumed the measured force is always perpendicular to the thigh, and the curvature of the brace equals to the curvature of the patient's thigh and is constant throughout the brace.

5.2.4 Ratings

During the gait training sessions, most cycles were rated in real-time by the PTs as "good", "ok" and "bad". After segmenting the time series into individual cycles, we labeled each by their rating, based on the time index that rating was recorded. "Good" cycles were the ones that PTs believed were successful in terms of facilitation, which generally consisted of more than 70% of the cycles. We only considered good cycles for all the analysis and learning throughout the paper.

5.3 Biomechanical characterization and Data Analysis

In this section, using the collected data, including the forms and recorded videos, we are going to characterize patient impairments, along with PTs facilitation strategies during the gait training sessions. As discussed in Sec.5.1, according to literature and the PTs, we can summarize our patient's impairments on the paretic side into three main features: 1) Knee hyperextension during initial loading due to the lack of control of the quadriceps muscles, 2) knee buckling/hyperextension in mid-stance, 3) knee hyper-extension at terminal stance if the hamstrings are also too weak. It must be noted that patients might not have all these three features together, depending on their impairment level and biomechanical features.

Patients with these types of impairments usually try to compensate for them (to prevent knee hyperextension and buckling) by limiting stance time and decreasing the weight-shifting on the paretic side and maintaining excessive knee flexion during mid-stance. These compensations often result in decreased step length on the non-paretic side, and altered lower-limb joint kinematics.

Consequently, what PTs mainly try to achieve during gait training sessions are increasing the stance time on the paretic side, to allow for enough time for the non-paretic side to take a normal step while stabilizing the knee on the paretic side during the weight-shifting. This is usually achieved by manual supporting of the quadriceps/hamstrings muscles during the stance phase.

For the rest of this section, we are looking into characterizing the patient impairments and gait training features described above through visualizations and quantification of the collected data.

5.3.1 Characterization of Patients' Gait

We use the MMT test results (in Table 5.1) to characterize the impairment levels of the four patients. MMT scores range from 0 to 5, with 0 being no contractions (on the muscles), and 5 being full range of motion against significant resistance (Ciesla et al. 2011). Therefore, we can conclude that P7 has the healthiest gait among other patients. P3 has the lowest scores on knee flexion and hip extension. Based on MMT results, we can group the patients into lower and higher muscular weakness (LMW and HMW) groups. As shown in Table 5.1, P7 and P5 are in LMW, and P6 and P3 are in HMW. Figure 5.6 shows the knee angles and weight-shift of the patients, as well as the assistive torque for analyzing the PT strategies corresponding to abnormal gait patterns. This figure includes the data for P6 and P7, each representing one muscular weakness group. To provide a reference for comparison, We also included a knee angle pattern of over-ground walking of healthy individuals in their natural speed, by averaging over 50 subjects data using the public dataset in (Lencioni et al. 2019). Overall, we did not observe any case of severe knee buckling and hyperextensions in the NT sessions, as our patients all had MMT scores > 2+ and were evaluated by the PTs to be able to ambulate with minimal assistance or less. Nevertheless, for P7 we observe excessive knee flexion angle in early mid-stance and at maximum weight-acceptance (as labeled in the knee angle plot for P7 in Fig. 5.6), which can be associated with the weakness of knee extensors (Li, Francisco, and Zhou 2018). On the other hand, we observe small or no knee flexion when entering mid-stance for P6 (as labeled in the knee angle plot for P6 in Fig. 5.6), which is another compensation strategy to stabilize the knee with weakness of knee extensors at mid-stance (Li, Francisco, and Zhou

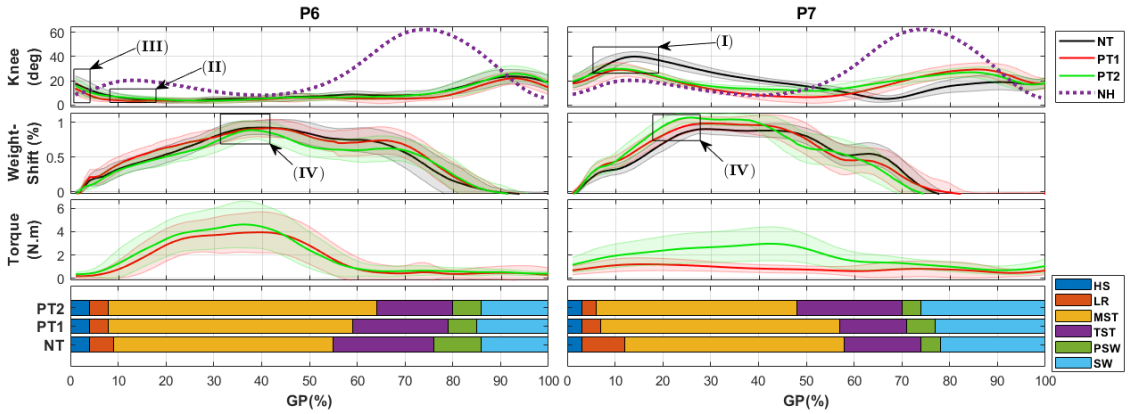

Figure 5.6. Visualization of the collected data for two patients. The solid lines represent the mean gait cycle of the particular data, while the shaded region shows the ± one standard deviation. NH (dotted line) refers to the standard knee angle trajectory of healthy individuals in over-ground walking at their natural speed. For generating this result and the rest of the paper, 55±8, 44±18, and 35±4 (averaged among the patients) cycles are used for NT, PT1, and PT2 sessions, respectively. Bar plots show the gait phases for each session. GP stands for gait phase. Annotations indicate (I) excessive knee flexion in early MST and maximum load, (II) small or no flexion entering MST, (III) knee extension at HS, and (IV) first peak (maximum load).

2018). Knee extension at heel-strike as a compensatory mechanism for the weakness of planter-flexor muscles (Li, Francisco, and Zhou 2018) is also observed in P6.

All patients showed similar irregular GRF patterns. The first peak, which represents the total weight acceptance, happens relatively late at the mid-stance, and the second peak, which is expected to be observed at terminal-stance/pre-swing, is blended into the first one and decreased in magnitude, shown in Fig. 5.6 (second row). Similar patterns were also seen in previous studies of post-stroke patients (Lauziere et al. 2014). This can be explained partly by the lack of proper heel-strike and push-off due to ankle dorsiflexion and plantarflexion weakness.

5.3.2 Gait Training (PT Strategy) Characterization

Here, we examine the outcome of each gait training session, highlighting the similarities and differences between the strategies employed by the PTs. According to the assistive torque plot in Fig. 5.6 (third row), generally lower magnitude torque is exerted for LMW patients, as expected. Peak torque is mostly located at 25% to 50% gait cycle, near where the maximum weight-acceptance in mid-stance takes place. This observation demonstrates an assistance strategy where the PT facilitates weight shifting onto the paretic side while stabilizing the knee to prevent buckling.

One goal of the PT is to increase stance time on the paretic side. As seen in Table 5.2, the stance time is increased in the training sessions. This increase is less frequently observed for P7, which could be related to the low impairment level of this patient compared to the others. More specific outcomes can also be observed for other patients. For example, P7's excessive knee flexion in mid-stance is corrected in the training sessions. It should be noted that motor skill acquisition through manual gait training is gradual and requires multiple sessions for the patient's joint kinematics to have a significant shift towards healthier gait patterns.

Table 5.2. Patient Stance Times

	Session		
Patient ID (P)	NT	PT1	PT2
3	1.17 ±0.13	1.29 ±0.22	1.50 ±0.46
5	1.51 ±0.34	2.33 ±0.68	2.13 ±0.78
6	2.08 ±0.46	2.48 ±0.57	2.94 ±0.45
7	1.28 ±0.16	1.32 ±0.21	1.38 ±0.13

5.4 Learning Gait Training Strategy: Virtual Impedance Learning

In this section, we propose an LfD framework for learning the gait training strategies from PTs, while considering the insights from rehabilitation and gait training literature, and the outcomes from biomechanical characterization in the previous section.

Impedance control framework has been a popular approach for robot-aided gait training due to the robust, low-gain, and compliant behavior (Buchli et al. 2011) that is necessary for tightly coupled Human-Robot Interaction (HRI) scenarios. In contrast to traditional approaches that reject disturbances, impedance control accommodates them by defining the robot's force behavior as a spring-damper system (Khan et al. 2019). The stiffness and dampening are dynamically changed according to varying time-dependent stiffness and damping gains. One way of defining these gains is to learn them from human observations using a learning-from-demonstration approach. Modeling the interaction force using the Virtual Impedance Modelapproach allows for avoiding large impact force in an unstructured environment and for cases where the demonstration and execution are different (Abu-Dakka and Saveriano 2020). Safe and stable interaction force can be achieved by concepts such as passivity and constraining variable impedance matrices (Abu-Dakka and Saveriano 2020). Therefore, providing safe and compliant interaction through a variable impedance framework is in line with the gait training policy.

5.4.1 Gait Training Insight Integration

The final goal of the impedance learning algorithm is to capture therapist strategies while exploiting the compliant behavior of impedance control. To that end, the

predictors for the impedance behavior (e.i. reproduced therapist assistance behavior) used in the learning algorithm should directly address the goals and strategies of the PT in a way that reflects the gait rehabilitation literature. For convenience, the key strategies that were identified in the bio-mechanical characterization of collected data are as follows:

- *S.1 Facilitate proper timing of joint kinematics* to compensate for altered lower limb kinematics especially excessive knee flexion during mid-stance.
- *S.2 Facilitate lateral weight shift onto paratic side* to prevent decreased weight shift to paratic side.
- *S.3 Maintain knee stability during mid-stance* to prevent the knee from buckling under additional weight acceptance.
- *S.4 Increase total stance time on paretic side* to prevent asymmetric gait and decreased step length on non-paratic side.

The most common feature describing gait was selected as the first predictor of therapist assistance. Knee angle x^K can be used to describe relevant joint kinematics at proper gait cycle intervals (*S.1*). Strategy *S.3* can also be addressed with x^K by capturing observations of knee buckling presented as hyper knee flexion during mid-stance.

However, *S.1* concerns more than just knee kinematics. First, unobserved joint kinematics, such as ankle and hip flexion, are necessary for fulfilling the objective of *S.1*. To address this, x^K was divided into shank x^{Sh} and thigh x^{Th} angles which capture half of the unobserved kinematics without the loss of information due to the x^K being deterministic of two resulting features. An added benefit of this division is that it addressed issues of characterizing impedance around intersections of state and attractor trajectories under attractor definition. Second, all joint kinematics must be

properly associated with the correct timing of any given state. Percent progression through the stance phase SP was selected as the reference due to the time-invariant needed due to differences in walking speed between patients. Therefore, features SP, x^{Th} and x^{Sh} were selected as predictors to capture PT assistance strategies *S.1* and *S.3*, Facilitation of weight shift (*S.3*) could explicitly be observed in this case. It was characterized by the percent of total force shifted to the paratic side x^{WS}. This feature was the strongest predictor for assistance. The strength of this predictor highlighted the focus of the therapist to facilitate the acceptance of additional weight onto the affected limb.

5.4.2 Formulation

5.4.2.1 Interaction Model

The interaction model for therapist assistance is defined as a virtual spring-damping system:

$$\tau_t = \mathbf{K}_t^{\mathcal{P}}(\mathbf{x}_t - \mathbf{y}_t) + \mathbf{K}_t^{\mathcal{V}}\dot{\mathbf{x}}_t \tag{5.8}$$

where $\mathbf{K}_t^{\mathcal{P}}$ and $\mathbf{K}_t^{\mathcal{V}}$ are the variable stiffness and damping values, τ_t observed assistance torque applied by the therapist around the patient's knee, $\mathbf{x}_t$ is the state(s) of the virtual impedance system, and $\mathbf{y}_t$ is the virtual attractor state(s). The attractor, under any definition, will drive the robot's force behaviour according to the interaction model Equation 5.8. The objective of the Virtual Impedance Modelis then to learn the attractor along with the stiffness and damping gains which will shape the compliant behaviour of the robot.

5.4.2.2 Attractor Definition

Impedance learning methods that calculate an arbitrary attractor through inverse dynamics require initial stiffness and damping values to be defined. These initial parameters usually are manually tuned or optimized to produce the best performance within the sample. A weakness of this approach is that when the attractor is defined with the inverse dynamics model, only one state can be used within a single reference frame as an attractor. This is due to the ambiguity introduced by the undetermined solution for the sum of the attractors equaling the observed torque. Alternatively, defining the attractor of the system to be a non-impaired gait trajectory makes strong assumptions. Patients' "healthy" gait trajectory is not consistent across individuals.

Integrating a more insightful approach to impedance learning may help resolve these challenges. The core assumption here is that a therapist will apply assistance in order to produce the patient's a future state. Our approach exploits the fact that we have access to the future trajectory of the states in our virtual impedance system during training and that these states can be accurately predicted with a past states due to the periodic nature of the gait cycle. Therefore, the attractor is both explicitly observed from the data and described by representative of states used by therapists in their decision-making model.

Two attractors were used to reproduce PT assistance during gait training, where the first will be used as a baseline to represent the typical attractor in the impedance learning literature:

A.1 Attractor 1 will be the attractor that is most common in the impedance learning literature. This trajectory will be calculated from the inverse dynamics found in Equation 5.9 using the most significant feature; x^{WS}. This reproduction

algorithm that uses the inverse dynamics of the virtual impedance system to calculate the attractor will be referred to as A_1.

$$\mathbf{y}_t = (\mathbf{K}_0^{\mathcal{V}} x^{\dot{WS}} - \tau_t)(\mathbf{K}_0^{\mathcal{P}})^{-1} + x^{WS} \tag{5.9}$$

where $\mathbf{K}_0^{\mathcal{P}}$ and $\mathbf{K}_0^{\mathcal{V}}$ are initial stiffness and damping values that are experimentally tuned to optimize performance.

A.2 Attractor 2 will be defined as the vector of the most relevant states that are consistent predictors across all patients; x^{WS}, x^{Sh}, and x^{Th}. The reproduction algorithm that uses this future-state attractor will be referred to as A_2.

$$\mathbf{y}_t = [x_{t+t_f}^{WS}, x_{t+t_f}^{Sh}, x_{t+t_f}^{Th}]^T$$

where t_f is the future time-offset, in percent stance phase, of the current state at time-step t.

5.4.2.3 Training

Given a set of demonstrations, the first step is to encode the relevant features into a Gaussian Mixture Model (GMM). GMM is a model-free learning algorithm that provides a probabilistic and robust framework that allows for the exploitation of the posterior probabilities later in the algorithm.

Inspired from (Glackin et al. 2015), the GMM encodes the state at the current time step $\mathbf{x}_t$ along with states from two previous time steps spaced uniformly with respective delays of t_p. The attractor is then appended to this array to define the

training data that will be encoded into the GMM.

$$\xi = [\mathbf{x}_{SP}, \mathbf{x}_{SP-t_p}, \mathbf{x}_{SP-2t_p}, \mathbf{y}_t]$$

With the training data defined, we can learn the model parameters for the GMM through maximizing the log-likelihood of the observed trajectories ξ by implementing the *expectation minimization* (EM) algorithm initialized by a *k-means* clustering procedure (Rozo et al. 2016). The number of Gaussian components k can be selected by using a model selection criterion. Here, we apply the Bayesian information criterion (BIC) (Akaike 1998) as the selection objective.

Impedance values for each GMM are learned by optimizing $\mathbf{K}_i^{\mathcal{P}}$ and $\mathbf{K}_i^{\mathcal{V}}$ to minimize the residual $\mathbf{r}_t$ between the reproduced torque $\hat{\tau}_t$, calculated using the interaction model and the observed torque τ_t.

The residual term for the modified interaction model then becomes $\mathbf{r}_{t,i} = \mathbf{K}_i^{\mathcal{P}}(\mu_i^y - \mathbf{x}_t) - \mathbf{K}_i^{\mathcal{V}}(\dot{\mathbf{x}}_t) - \tau_t$. This provides a level of abstraction that captures the underlying impedance for each Gaussian component's region within the state space. Consequently, this leads to a model that can more easily generalize the learned skill to new contexts.

5.4.2.4 Reproduction

The end of the training step results in the parameterized GMM in the form of $\mathcal{N}(\mu_i, \mathbf{\Sigma}_i)$, the mixing coefficients π_i and vector of impedance values for each state $\{\mathbf{K}_i^{\mathcal{P}}, \mathbf{K}_i^{\mathcal{V}}\}$ defined for every ith Gaussian component. Knowing this, we can then predict the time series attractor $\hat{\mathbf{y}}_t$ using Gaussian Mixture Regression (GMR) (Rozo et al. 2016). GMR is performed by creating a segmented GMM where the center and covariance matrices are decomposed into input $\mathcal{I}$ and output $\mathcal{O}$ spaces. The

dimensions of the input space correlate to the dimensions that represent the observable data during reproduction $\xi_t^{\mathcal{I}}$ while the output space correlates to the attractor we wish to predict $\xi_t^{\mathcal{O}}$. The posterior probabilities $\hat{h}_{t,i}$ for each Gaussian component can then be calculated using the decomposed GMM along the input space.

$$\hat{h}_{t,i}(\xi_t^{\mathcal{I}}) = \mathcal{P}(i|\mathcal{N}(\mu_i, \mathbf{\Sigma}_i)^{\mathcal{I}}) \tag{5.10}$$

5.4.3 Analysis

Reproduction behavior will be analyzed in three ways: magnitude, timing, and adaptivity of assistance. Additionally, algorithm performance will be compared using standard regression metrics for the coefficient of determination r^2 and root mean squared error $RMSE$. The metrics for behavioral analysis is as follows:

5.4.3.1 Magnitude

Here, the magnitude of assistance is captured by both the mean peak torque τ_p or impulse J which equates to the total amount of torque applied over the duration of the stride. These values are then calculated for each jth stride where the mean values are as follows

$$\tau_p = \frac{1}{N_s} \sum_{j \in N_s}^{j} \max(\tau_{j,t}) \tag{5.11}$$

$$J = \frac{1}{N_s} \sum_{j \in N_s}^{j} \int \tau_{j,t} d(t) \tag{5.12}$$

5.4.3.2 Timing

The timing of the reproduced assistance profiles was compared using a dynamic time warping (DTW) algorithm (Paliwal, Agarwal, and Sinha 1982) that minimizes the euclidean distance between the normalized observed and reproduced torques by stretching the SP indexes of each signal. The difference between the stretched time indexes was then calculated and rescaled to be $\Delta SP \in [0, 100]$. This provides a continuous measurement of delay in reproduced torque that is invariant of the magnitude of the assistance.

5.4.3.3 Adaptivity

Adaptivity can be approached from two perspectives. First, the PT may change their assistance behavior as the session progresses to match the evolving needs of the patient (fatigue, improvement, increased familiarity, ect...). To evaluate this time-series adaptivity, ΔJ, peak torque $\Delta \tau_p$ and stance duration on paratic side Δt_{stance} will be calculated for each stride j and fitted to a 1-st order least-squares regression in the form of $y = mx + b$. The slopes m will then be normalized using the maximum value of each feature in their respective sessions. This will result in a slope that describes the percent change m_p for each feature. Normalizing the slope in this way does introduce some limitations for the hMW groupthat will be discussed when the results are presented.

The second perspective for adaptivity considered that the variation in assistance between strides is stochastic but intentional. A therapist may apply pseudo-random perturbations in order to gauge the current status of the unassisted gait. Additionally,

random perturbations may be applied to keep the patient actively engaged in the training to prevent overreliance on the PT or automation of the task which has been shown to decrease rehabilitation outcomes (Cai et al. 2006). The algorithms will be evaluated on how well their variance σ matches the PTs' in three previously mentioned features. Here, we are only concerned with the total variance throughout the course of a full session and not how well the reproduced assistance matches the observed assistance.

5.4.3.4 Training Results

Attractor prediction was better for A_2 with a mean r^2 = 0.83 and $RMSE$ = 0.8 compared to with r^2 = 0.50 and $RMSE$ = −0.41. This shows that the GMR prediction of the attractor state(s) is sufficiently accurate for predicting future states but struggles in predicting an arbitrary attractor. The increased performance of A_2 is thought to be caused by the periodic nature of the data and the predictor space of the GMR being the past state.

The optimization step resulted in mean residuals of $9.70e^{-}5$ and 0.07 for A_1 and A_2 respectively.The training was able to finish in a mean training time of 4.6 seconds and a mean reproduction time of 0.0085 seconds. Therefore, the algorithm is efficient to train and extremely efficient during online reproduction due to the light GMR prediction and torque calculation. The reproduced assistance is shown in Figure 5.7. The full reproduction summary can be found in Table 5.4 and Table 5.3.

5.4.3.5 Magnitude Results

As expected from the separability analysis, the peak torques and stride impulses tended to normalize for both algorithms. This caused them to not be able to consistently capture the magnitude of assistance from stride-to-stride. The shaded region in Figure 5.7 shows the low performance for both algorithms to capture the full variance in the data. However, when considering the session as a whole, the reproduction algorithms have similar performances of $\Delta\tau_p = 0.06, 0.3$ and $\Delta J = 0, -0.50$ for A_1 and A_2 respectively in the lMW group. For the hMW group, $\Delta\tau_p = 0.09, 0.73$ and $\Delta J = 0, 09, 1.13$. Differences in magnitude reproduction performance was more evident in the hMW group but A_1 performed consistently better. Both algorithms tended to under-actuate but A_1 is able to very accurately reproduce the impulse done by the PT.

5.4.3.6 Timing Results

The full-time series delay can be found in Figure 5.8. There tends to be a higher delay in loading and unloading response than during peak. The average time offset of the course of the full stride showed a nominal difference with between the two algorithms.

5.4.3.7 Residual Estimation

The model was able to explain the majority of the observed torque with the modified interaction model during optimization. A mean residual of $\bar{\mathbf{r}}_i = 0.08N.m$

was found for all sessions with the exception of P6, an outlier, that had $\bar{\mathbf{r}}_i = 0.53N.m$. This is still believed to be sufficiently accurate with 11% of the observed peak torque being unexplained. Fig. 5.7 shows the residual torque component $\mathbf{r}_t$ (dashed, red line) included in the final reproduction of $\hat{\tau}_t$. Observations of $\mathbf{r}_t$ in Fig. 5.7 support the assumption that it is reproducing unmodeled assistance strategies like knee bracing. When present, $\mathbf{r}_t$ occurs most significantly during periods of maximum weight acceptance which requires a higher magnitude of assistance from the PT. The timing of increased $\mathbf{r}_t$ aligns with what we would expect from these strategies since the higher requirement for assistance also applies to these unmodeled strategies. Further evidence supporting that $\mathbf{r}_t$ represents these strategies is given by the absence of significant $\mathbf{r}_t$ in some patients, particularly those in the LMW group. This suggests that $\mathbf{r}_t$ is caused by a systemic perturbation from PT-P interaction and not by the sensing system, otherwise, we would likely observe this increased $\mathbf{r}_t$ throughout all sessions.

5.4.3.8 Adaptivity Results

Significant adaptation trends were mainly observed in P3 for both PTs and P7 for PT1. These sessions had an approximate 21% change in peak torque and impulse from start to finish of the session. Also, P5 showed an approximate change of 11% for both PTs. It should be noted that the adaptation for the hMW group was normalized with a low magnitude of assistance and it is possible that the PT is not able to apply such a fine time-series control over their assistance with a maximum of $m_J = -0.25\frac{N.m.s}{strode}$ and a maximum $m_{\tau_p} = 0.4\frac{N.m}{stride}$. Nonetheless, an interesting observation is that all for all sessions concerning impulse adaptation trends, the therapists showed approximately

Table 5.3. Adaptation Trends

	Δp^J		Δp^{τ_p}		$\Delta p^{t_{stance}}$	
P	PT1	PT2	PT1	PT2	PT1	PT2
3	20.82	19.79	27.10	-20.62	11.05	-1.83
5	4.53	10.33	-9.6	12.97	-22.72	2.89
6	6.16	2.42	-7.98	6.51	-4.66	-0.53
7	25.77	1.01	21.57	-0.61	-8.35	-7.70

the same magnitude of percent adaptation but in opposite directions. The sign of the adaptation slopes were evenly distributed between the PTs making it difficult to extract individual PT preferences for adaptation beyond the opposing relationship. Additionally, the low sample size as well as the no clear pattern was observed for between-patient adaptation trend for each PT does not enable a relationship to patient fatigue or improvement performance within a session to be made.

The second perspective considers adaptation as a stochastic and intentional perturbation to the assistance. As observed from the variation in the peak and impulse of assistance in 5.4, all algorithms had some trouble consistently reproducing the observed magnitude of assistance. There was a tendency to regularize the magnitude of assistance is partly expected due to the results of discriminate analysis which yielded low separability of the magnitude of assistance features. However, both algorithms were able to reproduce the difference in variation between the lMW and hMW groups.

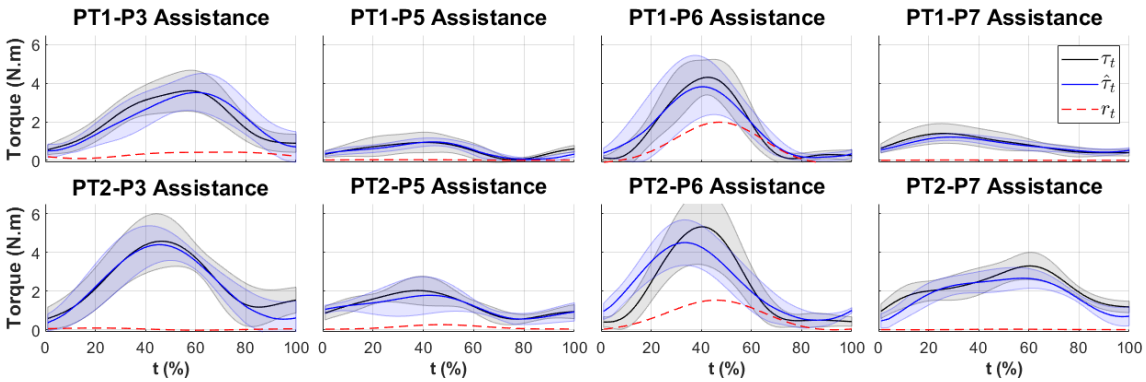

Figure 5.7. Reproduction results showing the observed torque from the PT τ_t (black) and the assistance reproduced by the impedance learning algorithm $\hat{\tau}_t$ (blue). The solid lines show the mean assistance while the shaded region shows the ± one standard deviation of the data. The dashed red line shows torque modeled by predicting the residual term $\mathbf{r}_t$ added to the interaction model.

Table 5.4. Reproduction Summary

MMT	Source	r^2	RMSE	ρ	ΔSP	τ_p	t_{τ_p}	σ_{τ_p}	J	σ_J
high	PT	-	-	-	-	4.51	50	1.94	*3.24	*2.83
high	A_1	0.65	0.83	$5e^{-129}$	0.90	4.42	47	1.15	*3.13	*2.62
high	A_2	0.67	0.82	$4e^{-203}$	1.78	3.78	47	0.88	*2.84	*1.70
low	PT	-	-	-	-	1.93	44	1.03	*1.22	*1.76
low	A_1	0.46	0.37	$4e^{-57}$	-2.27	1.87	36	0.58	*1.22	*0.81
low	A_2	0.36	0.44	$2e^{-38}$	0.23	1.63	41	0.63	*1.81	*1.43

5.5 Discussion

In this chapter, significant effort was invested into creating an insight-driven and data-informed foundation for learning PT assistance behaviors. The analysis in Sec. IV showed that a unique and diverse set of gait behaviors and assistive responses emerged from patients that would generally be considered to have the same level of impairment. Although the presentation of impairment was unique for each patient, most observations aligned with insights from previous post-stroke rehabilitation studies, such as excessive knee flexion during mid-stance or episodes of knee hyperextension. This observation shows the importance of learning assistance strategies from physical therapist-patient (PT-P) interactions.

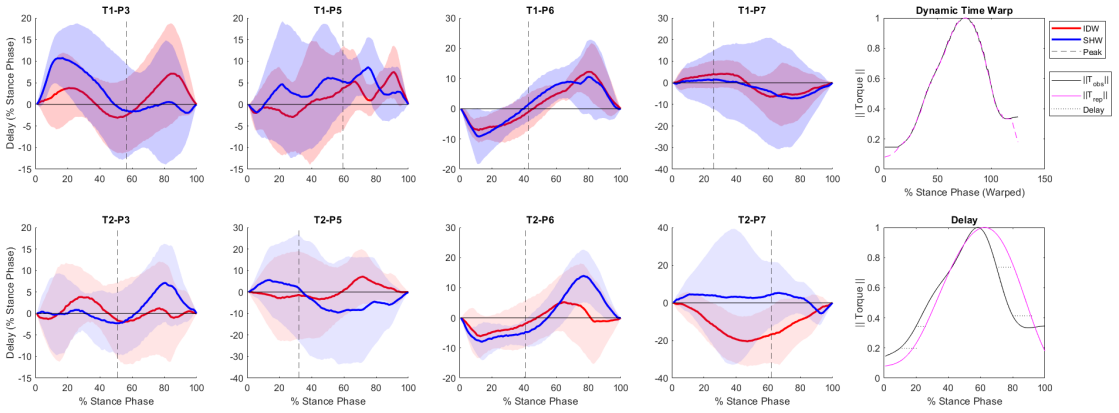

Figure 5.8. The last column in the figure shows how the observed and reproduced torque are transformed using DTW (top) and a black dotted line that represents the calculated delay at as an example (bottom). The rest of the figure describes the results of the continuous-time delay, in the percent stance phase, calculated using a dynamic time-warping function. The solid colored line represents the mean delay for each P-T pair while the shaded region encompasses one standard deviation for the A_1 (blue) and A_2 (red) algorithms. The vertical black line represents the mean timing of the peak torque.

The proposed approach includes the feature of weight-shift to emulate qualities of the PT. While weight shift is generally an important and well-studied phenomenon in gait training of post-stroke patients (Mauritz 2002; Andersson and Franzén 2015), it has received far less attention when developing wearable robots. We use weight-shift in conjunction with a future-state attractor and more common kinematic features (thigh and shank), to generate positive results that match the magnitude and timing of PT assistance. Timing of the assistance is especially critical for effective rehabilitation and reduction of metabolic cost (Bryan et al. 2021). Success in these areas implies that a lower-limb exoskeleton would be able to provide the appropriate assistance to the patient.

However, the algorithm showed some challenges in reproducing the nuances in stride-to-stride assistance variation. This observation is likely due to a combination of three factors: 1) the PT may be unable to assist in a perfectly consistent way due to stochasticity of human-human interaction and the associated challenges with

manual gait training, 2) inherent limitations in the sensing system may cause variation in observed data, and 3) the abstraction of high variance torques to a cumulative model of behavior during Gaussian mixture model (GMM) encoding causes loss of information describing variation between strides in an attempt to be robust against over-fitting and noise.

Alternatively, the model may be missing the deterministic feature(s) that explain stride-to-stride variations such as adaptive PT assistance as the patient fatigues or improves. However, we must be cautious when adding additional features to balance the trade-off between 1) a low-dimensional and generalizable model, 2) adding cumbersome sensors that interfere with patient rehabilitation, and 3) possible introduction of noisy inputs.

5.5.1 Implications

The proposed algorithm functions as a high-level decision framework that generates a continuous control input (reproduced torque) in a way that emulates assistive PT behaviors. Any arbitrary low-level controller (i.e. PID) can then use this control input to actuate a 1-DoF lower-limb knee exoskeleton to provide assistive knee torques. Specifically, this work shows how additional expert PT knowledge and clinical insights can be identified and integrated into a high-level decision model. Done successfully, this implies that a more robust, effective, and personalized robotic assistance can be generated. Furthermore, the characterization of discrete impedance strategies in response to classes of gait behaviors reduces the learning problem from encoding the assistive response for every possible continuous-state combination to one that is tractable, computationally efficient, and more robust against over-fitting. Opportunity

for generalizing to new patients is also present given the fairly safe assumption that assistance strategies do not significantly change between patients with similar gait behaviors. Therefore, once a sufficient amount of data is collected to characterize common gait patterns, the trained model will require little to no additional training when being used to assist a new patient.

5.6 Limitations and Future Work

5.6.1 Data Collection/Biomechanical Characterization

Several limitations were present in this study; the most prominent of which concerns data collection. Access to a sizable patient pool for rehabilitation is challenging. Collecting data from more patients in the future will allow this study to strengthen the proposed conclusions as well as resolve inconclusive results due to the sample size. In addition to the number of data collection sessions we could obtain, the data collection system provided several challenges in obtaining quality data. Although the effects were mitigated during data processing, the wearable sensors used are subject to errors caused by attachment inconsistencies and shifting during the session. Additionally, the wearable data collection system must maintain a minimum level of intrusiveness to not interfere with the patient's rehabilitation. This prevents challenges in capturing additional dynamics and force interactions on other body parts.

5.6.2 Algorithm

The virtual impedance modeling algorithm also presents several opportunities to be improved. Mainly, additional insights can be included by dynamically defining the future time offset during attractor generation or by condition the prior of the GMM such that the Gaussian means to target specific impairment characteristics that change how a PT would assist. Both approaches to making this framework more supervised will be explored in the future to further increase the practical consideration of gait training principles for a generalizable algorithm. Demonstrating the ability to generalize in this way will be done as an extension of this work along with stability analysis to demonstrate the compliant capabilities of the algorithm.

Chapter 6

SAFETY FILTERING FOR GAIT ASSISTANCE AND REHABILITATION

6.1 Introduction

In Chapter 5, we explored the learning of a virtual impedance controller, drawing insights from therapist-patient interactions to encode high-level gait training strategies derived from manual physical therapy. A crucial consideration that emerges is how to effectively apply such controllers, learned from limited demonstrations to diverse patients exhibiting similar gait disorders.

A primary challenge in this application lies in ensuring the safety of the controller when deployed with patients whose gait and lower-limb dynamics deviate from those on which the controller was initially trained. The safety and stability of robotic assistance become paramount, particularly in autonomous operation, catering to patients and individuals with gait disorders.

This challenge extends to a broader perspective: how to guarantee the safety of lower-limb interaction assistance when controllers are learned from data gathered in interactions with a limited number of individuals. The inherent variance and stochastic nature in human dynamics and kinematics, including gait trajectories and joint torques, are not fully addressed in such controllers. The intricate nature of the human motor system and the diversity among individuals can result in unique responses to the same robotic device (Berger et al. 2019).

Human-in-the-loop optimization frameworks have recently gained considerable attention (Q. Zhang et al. 2022; J. Zhang et al. 2017; Slade et al. 2022), aiming

to achieve personalized assistance and adaptation while optimizing an objective function based on real-time interaction with individuals. However, the challenge of imposing safety when interacting with the user to learn new controllers has not been systematically addressed.

6.1.1 Litrature Review: Safety Filtering and its Application to Robotic Gait Assistance

As stated above, the main challenges of applying safety filters in our application are unknown and uncertain interaction dynamics with the human, as well as limited robot inputs (compared to human inputs) and under-actuation. Thus here we look into the state-of-the-art in active safety filtering with minimum assumptions on model parameters and disturbances to the system, with a specific focus on safety guarantees in lower-limb human-robot interaction.

One popular approach for enforcing safety with a nominal controller is reachability analysis (Brunke et al. 2022). In (Akametalu et al. 2014) reachability analysis has been used to guarantee dynamic safety constraints by using Gaussian Process and its error confidence to extend the set of exploration for uncertainty in the system. Such approaches are very useful when a good approximate dynamic model is available, with a bounded disturbance assumption.

One of the most recent popular approaches in safety filtering is control barrier functions (Ames et al. 2019) where active set invariance methods have been employed to find the minimally invasive controller (in relation to a nominal controller).

In the realm of safety and gait robotic assistance, Tucker, Li, and Ames 2023 proposed a robust discrete control barrier function for trajectory generation for a

full lower-body exoskeleton using Poincare maps. In another work a scalable control barrier function (implicit control barrier function) was applied on a full-lower body exoskeleton to provide variable assistance based on a virtual guide filter Gurriet et al. 2019. In implicit safety filters, a baseline safe controller and a known safe set are employed to enforce safety without considering full-model dynamics. In both of these works, practical and rigorous methods have been proposed to treat uncertainty and stochasticity in the human-robot interaction. However, they still rely on a known dynamic model, and more importantly, the robot is fully actuated and can overpower human input (joint torques). Therefore human input has only been considered as a disturbance and is assumed to be treated through the robustness of the safety controller.

6.2 Problem Formulation

In light of the current challenges of applying safety in gait assistive and rehabilitation devices, our goal is to impose safety guarantees for given (nominal) controllers that are learned based on interaction with the users, with the least possible knowledge and assumptions on the human gait model parameters and inputs (i.e. joint torques). Therefore this problem can be formulated as an active safety filtering of the nominal controller, with probabilistic safety guarantees.

Here we propose to develop a framework based on implicit safety filtering using control barrier functions (Gurriet et al. 2020). This method is based on realizing control invariant sets by online prediction of the closed-loop system for a finite time horizon under a safe backup control law. Implicit safety filtering is chosen for our application, for the following reasons:

- Less numerical complexity and requirement on the human model and input. In this formulation, we need to work with the closed-loop dynamics under the backup controller. That means we do not need to learn how to map the controller to the states. More importantly, we do not need to explicitly consider human inputs.
- Feasibility of finding a safe baseline controller. This baseline controller can be any controller that we know is safe to use within our safety set. For example in the case of assistance of healthy subjects, this controller can just be a zero-assistance controller, which means letting the user take full control of the motion. Any other controller that we have prior knowledge of its safety is also applicable.

6.2.1 Implicit Safety Filtering using a Backup Controller

The formulation of the implicit safety controller in this section is based on the work of Gurriet et al. 2020. Safe-known controllers (backup controllers) are used to design safety filters that can realize controllers around the neighborhood of the nominal controller, for the continuous-time control affine dynamical system.

$$\dot{x} = f(x) + g(x)u \tag{6.1}$$

f and g are defined on a compact set and are Lipschitz continuous and differentiable. The control policies are Lipschitz continuous functions in $x \in X \subset \mathbf{R}^n$ and piece-wise continuous in time.

A closed set $S \subset X$ is control invariant for (6.1) if there exists a control policy u such that if $x(t_0) \in S \Rightarrow x(t) \in S$, for all $t > t_0 \in \mathbf{R}^+$. This means the system trajectories will never leave S under u.

Now we can define the flow of the system under a controller u as the system trajectories corresponding to (6.1), starting from x_0 at $t = 0$ to $t = T$, by $\phi_u^\tau(x_0)$. Given a practical safety set $\bar{S}$, it can be characterized by n_s differentiable functions $h_i : \mathbf{R}^n \to \mathbf{R}$ such that:

$$\bar{S} = \{x \in \mathbf{R}^n | \forall i \in \{1, ...n_s\}, h_i(x) \geq 0\} \tag{6.2}$$

$$\partial\bar{S} = \{x \in \mathbf{R}^n | \exists i \in \{1, ...n_s\}, h_i(x) = 0\} \tag{6.3}$$

where $\partial\bar{S}$ is the boundary of $\bar{S}$. Given a backup policy u_b, we can define the invariance of $\bar{S}$ under u_b can be guaranteed by $h_T^{u_b}(x) \geq 0$, where

$$h_T^{u_b}(x) = \min_{\substack{\tau\in[0,T] \\ i\in\{1,...n_s\}}} h_i(\phi_{u_b}^\tau(x)) \tag{6.4}$$

The set characterized by $h_T^{u_b}(x)$ (which is $\bar{S}_T^{u_b}$) is itself a subset of $\bar{S}$ ($\bar{S}_T^{u_b} \subseteq \bar{S}$) if S is control invariant under u_b. This set can be used to find a new safe controller u_f, which is a continuous selection between a nominal controller u_n and a backup safe controller u_b:

$$u_f(x) = \alpha(t, u_N(x), x, h_T^{u_b}(x)) \tag{6.5}$$

$$x \in S_T^{u_b}, \alpha(t, u_N(t), x, 0) = u_b(x) \tag{6.6}$$

where α is a continuous function. If all the requirements are met, It is trivial to show $\bar{S}$ is the control invariant under $u_f(x)$.

These results (Gurriet et al. 2020) give us a powerful tool to form a safety filtering law for our nominal controller. We need to be able to predict the system trajectories

under the backup controller ($\phi_{u_b}^T(x)$) to find $h_T^{u_b}(x)$. Also, we need to properly design the switching function α.

In order to apply this safety filter for human-robot interaction applications, we need to make three main assumptions:

Assumption 1: The deterministic human-robot interaction dynamics can be modeled as a non-linear control-affine system.

Assumption 2: For the given safety set S, We know the control invariant set $\bar{S} \subseteq S$, where u_b is a safe controller for $\bar{S}$.

Assumption 3: For a given control policy $u(x)$, the steady-state closed-loop dynamics of human-robot interaction can be modeled as a Gaussian process $p(x_{k+1}|x_k) = \mathcal{N}(x_{k+1}|\mu_{k+1}, \sigma_{k+1}^2)$ We used multivariate GP with multi-step predictions, similar to the work of Deisenroth and Rasmussen 2011.

Therefore the flow of the system can also be described as a discrete random process:

$$\phi_{u_b}^T(x_k) = \{X_j\}_{j\in[1,\dots,n_T]} \tag{6.7}$$

$$X_j \sim \mathcal{N}(\mu_j, \sigma_j) \tag{6.8}$$

where n_T is the number of time steps to get to the time T.

6.2.2 Implicit Safety Filter with Prediction Uncertainty

Now that the flow of the system is formulated as a stochastic process, we can only ensure the safety of the system with a specific confidence level. For each prediction X_j, assuming it has a normal distribution, we can define a η-level confidence set ($\eta \in (0, 1)$)

which we call the uncertainty set:

$$D_j^\eta = \{x \in \mathbf{R}^n | \forall i \in \{1, ...n_s\} : (x - \mu_j)^T \Sigma_j^{-1} (x - \mu_j) - \chi^2_{n,\eta} \leq 0\} \tag{6.9}$$

where $\chi^2_{n,\eta}$ is the chi-squared distribution with n degree of freedom, evaluated at $1 - \eta$. D_j^η is a convex ellipsoid-shape set.

Thus we need to consider this uncertainty set in (6.4). we can do that in a 2-step optimization problem. First step, we find the minimum value of each $h_i(x)$ for each uncertainty set D_j^η:

$$\begin{aligned} h_{ij} &= \min_x h(x) \\ \text{s.t.} \quad & x \in D_j^\eta \end{aligned} \tag{6.10}$$

Then we find the minimum value of h_{ij}s and set that as $h_T^{u_b}$:

$$\begin{aligned} h_T^{u_b} &= \min_{i,j} h_{ij} \\ \text{s.t.} \quad & i \in \{1, \ldots, n_s\}, \quad j \in \{1, \ldots, n_T\} \end{aligned} \tag{6.11}$$

If $h_i(x)$ are convex (or concave) functions, then (6.10) is a convex optimization problem that can be solved using any standard convex optimization method. Therefore at each step, we need to solve $n_s \times n_T$ Convex optimization problem. Therefore we should try to represent the safety set with a minimum number of barrier functions.

6.2.3 Controller Design

The next step is to design the α function in (6.5). This function needs to be a continuous selection of $u_N(x)$ and $u_b(x)$, with the condition that at $h_T^{u_b}(x) = 0 \rightarrow$

$u_f(x) = u_b(x)$. We consider the following general form of switching function:

$$\alpha(u_N, u_b, x, h_T^{u_b}) = u_b + \lambda(h_T^{u_b})[u_N - u_b] \tag{6.12}$$

where $\lambda : \mathbf{R}^+ \to [0, 1]$ and $\lambda(0) = 0$. We also require λ to be a monotonic non-decreasing function. This will help us to regulate the filter behavior based on the magnitude of $h_T^{u_b}$: $h_T^{u_b}(x_1) \geq h_T^{u_b}(x_2) \to \lambda(h_T^{u_b}(x_1)) \geq \lambda(h_T^{u_b}(x_2))$.

One choice for λ can be $\lambda(h_T^{u_b}) = 1 - e^{-\mathbf{a}h_T^{u_b}}$. Here $\mathbf{a}$ is a design parameter that defines how fast (aggressive) our controller goes from u_b to u_N, based on the values of $h_T^{u_b}$. Ideally, we want this switch to be as fast as possible, so we can apply the nominal controller when we are far enough from the boundaries of $\bar{S}_T^{u_b}$.

6.2.4 Online Iterative Learning

One issue with the given safety filter is its inherent conservative behavior. u_f is always between the nominal and backup controller, regulated by the prediction of the flow of the system under the backup controller. However, ideally, we want to be able to apply the nominal controller, unless the nominal controller is not safe. In the given safety filter, the notation of safety is completely defined based on the backup controller, and not the nominal controller. This is because the safety filter regulates the nominal controller based on the closed-loop system with the backup controller.

Additionally, as our dynamic model is a GP model that estimates the future state based on previously observed state, in scenarios where we meet unobserved states within the safe set, the predictions come with high uncertainty. This high uncertainty can reduce the estimated value of $h_T^{u_b}$ and lead to conservative behavior as depicted in Fig. 6.1. We cannot update our GP with the new observations since we are applying

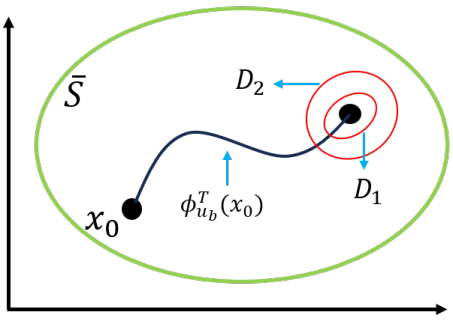

Figure 6.1. Graphical representation of how higher uncertainty in prediction can lead to a more conservative controller. In the case of a larger uncertainty set (D_2), the boundaries of D_2 are closer to the boundary of the safety set $\bar{S}$, so our safety filter will switch to a control input closer value to u_b.

u_f instead of u_b. Visiting unobserved states is also very likely to happen as we replace u_b with u_f, which can push the system to new unobserved states within the safe set.

To address the above-mentioned issues, here we propose an online iterative learning method in which, at each iteration, we can find a less conservative controller (if possible).

The idea is that after running a couple of cycles with the controller u_f, we use the collected data to learn a new GP to model the closed-loop system with u_f. Since by definition u_f is also a safe controller for our system, we can use that as the backup controller. This has two beneficial features:

- The newly collected trajectories contain the previously unobserved states, therefore in the new GP, the uncertainty for those states will reduce, resulting in a less conservative controller.
- We can show mathematically that at each step of the iteration, under some conditions, the filter can find control inputs closer to the nominal controller, and possibly converge to it.

6.2.4.1 Convergence Analysis

Let's denote u_k to the safety filter controller applied at the k_{th} state of the iteration. At each iteration, the backup controller is u_{k-1}, with $u_0 = u_b$ (u_b is the original backup controller). Thus for $k \geq 1$:

$$u_k = u_{k-1} + \lambda_{k-1}[u_N - u_{k-1}] = u_N + (1 - \lambda_{k-1})[u_{k-1} - u_N] \tag{6.13}$$

where $\lambda_k = \lambda(h_T^{u_k}(x))$. By induction, it is trivial to see that:

$$u_k = u_N + (1 - \lambda_{k-1})(1 - \lambda_{k-2}) \dots (1 - \lambda_0)[u_0 - u_N] \tag{6.14}$$

Corollary 1: At each step of the iteration, the safety filter is a less (or equally) conservative controller compared to the previous step: $|u_N - u_k| \leq |u_N - u_{k-1}|$

Proof: This results from (6.13) and the fact that $0 \leq 1 - \lambda_{k-1} \leq 1$:

$$u_k - u_N = (1 - \lambda_{k-1})[u_{k-1} - u_N] \Rightarrow |u_N - u_k| \leq |u_N - u_{k-1}| \tag{6.15}$$

Corollary 2: if $x \in \partial \bar{S}_T^{u_b}$ then for any $k \in N$, $u_k = u_b$.

Proof: We know that $x \in \partial \bar{S}_T^{u_b} \Rightarrow h_T^{u_b}(x) = 0 \Rightarrow \lambda_0 = 0 \Rightarrow u_1 = u_b$. By induction:

$$\begin{aligned} \lambda_1 = \lambda(h_T^{u_1}(x)) = 0 \Rightarrow u_2 = u_1 = u_b \\ \vdots \\ \lambda_{k-1} = \lambda(h_T^{u_{k-1}}(x)) = 0 \Rightarrow u_k = u_{k-1} = u_b \end{aligned} \tag{6.16}$$

Corollary 2 basically implies that the iterative safety filter is also limited to $\bar{S}_T^{u_b}$ ($\bar{S}_T^{u_k} = \bar{S}_T^{u_b}$) and the controller selection at the boundary of $\bar{S}_T^{u_b}$ is limited to u_b.

Theorem 1: if $x \in \bar{S}_T^{u_b} \setminus \partial \bar{S}_T^{u_b}$ (interior of $\bar{S}_T^{u_b}$), then for $k \to \infty$, u_k will converge to a known bounded value u_{k_f}

Proof: Let's assume that: $\exists \delta > 0, \forall k \in \mathbf{N} \mid \delta = \inf\{\lambda_k\}$. Then it is trivial to see that the sequence in (6.14) will converge to u_N. The existence of such lower-bound δ requires that all $h_T^{u_k}(x) > 0$. That also includes $h_T^{u_N}(x) > 0$. However, $h_T^{u_N}(x) > 0$ is a necessary but not sufficient condition for convergence to u_N. That is because if $\exists k_f \mid h_T^{u_{k_f}}(x) = 0$, then similar to proof in (6.16) we can show that for all $k > k_f$: $u_k = u_{k_f} = u_N + (1 - \lambda_{k_f})(1 - \lambda_{k_f - 1}) \dots (1 - \lambda_0)[u_0 - u_N]$. Therefore:

$$\lim_{k \to \infty} u_k = u_{k_f} \tag{6.17}$$

6.3 Simulation

In this section to show the effectiveness of our method in filtering a nominal controller, and iteratively learning a less conservative controller, we implemented the proposed safety filter on an inverted pendulum that resembles human gait.

6.3.1 Simulation Setup

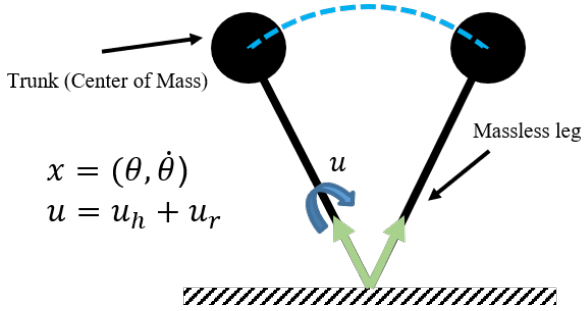

Figure 6.2. Inverted Pendulum with separate human and robot (u_h and u_r) input.

Inverted pendulums are commonly used as a reduced-order model of human gait (Kuo 2007). As depicted in Fig. 6.2 the states of the system are the angle and angular velocity of the pendulum. The input to the pendulum is a torque which is a sum of human and robot torque. For human torque, we considered a stiffness-damper model, where its parameters (k and b) have zero mean Gaussian noise component:

$$u_h = k(\theta - \theta_0) + b\dot{\theta} \tag{6.18}$$

$$k = k_n + w_k,\ w_k \sim \mathcal{N}(0, \sigma_k), \quad b = b_n + w_b,\ w_b \sim \mathcal{N}(0, \sigma_b) \tag{6.19}$$

Noise components were added to make the system resemble the stochastic behavior of human gait.

6.3.2 Safety Filter Controller

At each iteration step, we applied the controller for a fixed period of time $T_L = 2\ Sec$, for $m = 5$ cycles. Each cycle was started at $x_0 = [0, 0]^T + w_0$ where w_0 is a white Gaussian noise. Data was sampled at 50 Hz, and the prediction horizon for the safety filter was $T = 0.06 Sec$. The switching law is chosen as $\lambda(h_T^{u_b}) = 1 - e^{-\mathbf{a}h_T^{u_b}}$.

In total, we ran three iterations. The pseudocode of the total process is given in Alg. 2. The backup controller was set to $u_b = 0$, meaning the pendulum was run by the human controller u_h. The safety set was chosen to be an ellipsoid, and its control invariance under u_b was confirmed through simulation. For the nominal controller, we considered two cases of a safe and unsafe controller.

Algorithm 2 Safety Filter with Online Iterative Learning

Apply $u_r = u_b$ →Collect Data $\mathbf{X_0}^{n\times m\times l}$
for $k = 1, 2, 3$ **do**
  Train GP_{k-1} with $\mathbf{X_{k-1}}$
  for $i = 1, 2, \dots m$ **do**
    Initialize $x_0 = [\theta_0,\ \dot{\theta_0}]^T + w_0$
    for $j = 1, 2, \dots l$ **do**
      $[\phi_T^{u_0}(x_j) \dots \phi_T^{u_{k-1}}(x_j)] = [GP_0(x_j) \dots GP_{k-1}(x_j)]$
      Calculate $[h_T^{u_0} \dots h_T^{u_{k-1}}]$ using (6.9), (6.10) and (6.11)
      Apply $u_r = u_N + (1-\lambda_{k-1})(1-\lambda_{k-2})\dots(1-\lambda_0)[u_0 - u_N]$
      $x_j \to x_{j+1}$
    end for
    $\mathbf{X}_K^i = [x_0, x_1 \dots x_l]$
  end for
  $\mathbf{X}_K = \mathbf{X}_K^{1:m}$
end for

6.3.3 Results

Here we present the results of the simulation for the two cases.

6.3.3.1 Case Study 1: Safe Nominal Controller

The simulated flow of the system under the backup and nominal controller is shown in Fig. 6.3. It must be noted that we took the average flow of the system, given the stochasticity in trajectories. System trajectories for the three steps of iterations are also shown, as well as the control inputs. We can observe clearly that through iterations, the system trajectories get closer to the nominal controller, as well as the control inputs.

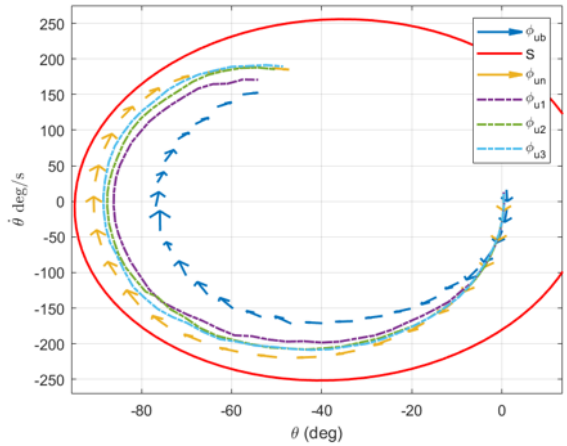

(a) Average System Trejectories

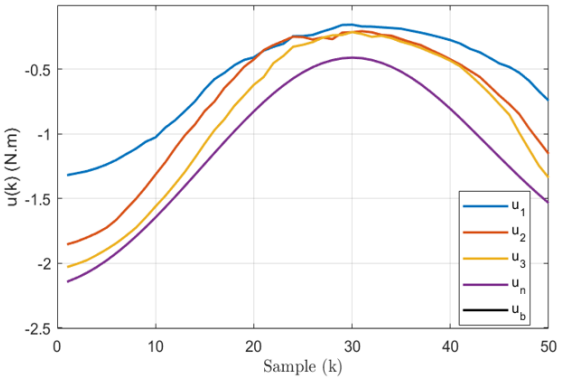

(b) Average Control Efforts

Figure 6.3. Simulation with a safe nominal controller. ϕ_{u_k} refers to the closed loop system trajectories with the controller u_k, at the k_{th} iteration of the filter.

6.3.3.2 Case Study 2: Unsafe Nominal Controller

In this case, we observe that the trajectories of the system under the iterative safety filter gradually converge to the boundary of the set, without existing the safety set (Fig. 6.4). We also observe that for the first half of the cycle, at each step of the iteration of the safety filter, we get a controller that is closer to the nominal controller. However, towards the end of the cycle, since the safety filter is pushing the system

towards the boundary of the safety set, u_3 is switching back to u_1 (as is shown in Fig. 6.4-b), in order to keep the trajectories safe.

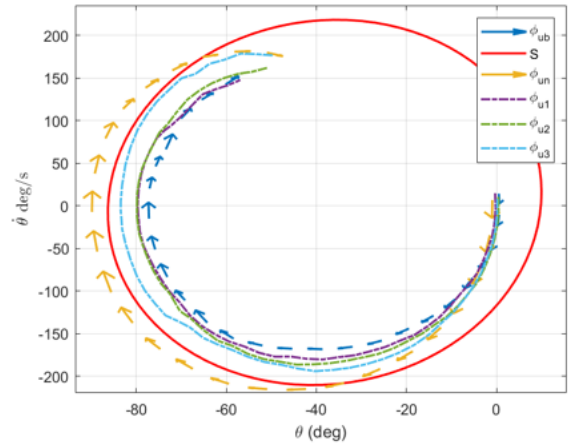

(a) Average System Trejectories

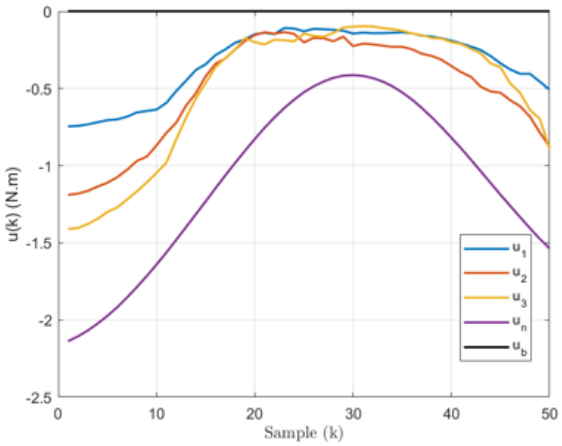

(b) Average Control Efforts

Figure 6.4. Simulation with an unsafe nominal controller. ϕ_{u_k} refers to the closed loop system trajectories with the controller u_k, at the k_{th} iteration of the filter.

6.4 Discussion

6.4.1 Applicability of the Proposed Safety Filter for Gait Robotic Application

Besides the three main assumptions that we made in Sec.6.2, we also need to address the problem of under-actuation for many robotic gait applications. Considering a biped model, all the joints are dynamically coupled and therefore will affect each other. When we only need to assist one joint, technically we still need to consider all the joint angles and velocities in the model (full-order model), which will significantly increase the computational cost of the filter. However, if through experimental data we can show that by just considering the states of the targeted joint (reduced order model), our GP can still predict the closed-loop system trajectories (for the given filter time horizon) within the desired confidence level, then the safety filter will be robust to using the reduced-order model.

6.4.2 Limitations

One main limitation of the proposed safety filter is its reliance on the backup controller. First of all, finding a proper safety filter in some scenarios can be challenging. While for assistance applications with healthy individuals, the zero-assistance controller can be a proper and intuitive choice, for gait training applications with patients with gait disorder we might not be able to use such a controller as a safe controller. In other words, using this safety filter requires a prior known backup controller instead of a dynamic model, which is also not always easily available. Another issue is the performance of the safety filter inherently relies on the backup controller. While the

proposed iterative learning component can find more optimal controllers, we are still limited to the backup controller at the boundary of the safe set.

6.5 Conclusion

In this study, we introduce a safety filter incorporating an online iterative learning component designed for application in robotic gait assistance. This innovative approach offers robust safety guarantees for system trajectories, addressing challenges such as stochasticity and the absence of a known prior dynamic model. These challenges represent the fundamental obstacles in human-robot interaction within gait assistance and rehabilitation applications. The online iterative learning components ensure finding less intrusive controllers (in relation to the nominal controller) at each step of the iteration.

Chapter 7

CONCLUSION

In this thesis, we employed different techniques in wearable sensor design, state estimation, and control theories, as well as biomechanical characterization and statistical learning, to provide novel and useful insight toward safer and more intelligent robot-aided gait training and assistance strategies.

In Chapter 3, a damped harmonic oscillator model was proposed based on a previously developed harmonic oscillator model for EMG signals, to account for the change in energy level of EMG signals due to gait activity changes. The root means square (RMS) and energy of the EMG signals are the features adopted in this method. The energy of the EMG signal is extracted using the energy kernel method. The proposed approach uses a low number of sensors and features, online unsupervised classification, and is generalizable to different lower-limb muscle groups.

In another study, we introduced a new invariant extended Kalman filter design in chapter 4, that produces real-time and rapid error convergence for the estimation of the human body movement even in the presence of sensor misalignment and initial state estimation errors. The filter fuses the data returned by an inertial measurement unit (IMU) attached to the body (e.g., pelvis or chest) and a virtual measurement of zero stance-foot velocity (i.e., leg odometry). The key novelty of the proposed filter lies in that its process model meets the group affine property while the filter explicitly addresses the IMU placement error by formulating its stochastic process model as Brownian motions and incorporating the error in the leg odometry.

In Chapter 5, by employing a novel custom-made wearable sensor, we collected the

haptic interaction in gait therapy sessions. The patient's impairment and therapist assistance were characterized. Preliminary analysis shows that knee extension and weight-shifting are the most important features that shape a therapist's assistance strategies. These key features are then integrated into a virtual impedance model to predict the therapist's assistive torque. Our model was able to capture high-level strategies of the therapist assistance, which in the future can be used to encode therapist strategies into a robot controller.

And lastly, in Chapter 6, we introduced a safety filter to regulate any nominal controller, to provide probable safety guarantees for gait robotic applications in the absence of a human dynamic model and inputs. An online iterative learning component was introduced to the safety filter to ensure the finding of less conservative controllers. Simulations with an inverted pendulum that resembled human gait showed the efficacy of the proposed method.

The research conducted in this dissertation lays the groundwork for more robust and efficient lower-limb robotic assistance. Moving forward, the precise estimation of human states and activities through wearable sensors holds the potential to extend the applications of gait wearable robots beyond controlled laboratory conditions. This advancement marks a pivotal step toward the clinical deployment of wearable robots.

Moreover, the incorporation of human motion states into the safety filter is a promising avenue. For instance, constraining the motion of the Center of Mass (CoM) can be a notion of safety for gait wearable robots. By utilizing reduced-order models, such as an inverted pendulum to relate CoM states to joint states, it becomes possible to construct a safety filter that can complement various controllers. This approach broadens the spectrum of controllers applicable for training and assistance, ensuring the safety of the controller through the integration of the safety filter.

To translate the insights and intelligent decision-making behaviors acquired from manual therapy into practical applications, a thorough evaluation of the controller in diverse cases is essential. Additionally, further data collection efforts can help determine if Gaussian Mixture Models (GMMs) can effectively capture a broader range of gait behaviors and the corresponding gait training strategies. The integration of the safety filter enhances the generalizability and autonomy of the controller which are necessary steps towards clinical deployment and expansion of gait wearable robot applications.

REFERENCES

Abu-Dakka, Fares J, and Matteo Saveriano. 2020. 'Variable Impedance Control and Learning—A Review.' *Frontiers in Robotics and AI* 7.

Akaike, Hirotogu. 1998. 'Information theory and an extension of the maximum likelihood principle.' In *Selected papers of hirotugu akaike,* 199–213. Springer.

Akametalu, Anayo K, Jaime F Fisac, Jeremy H Gillula, Shahab Kaynama, Melanie N Zeilinger, and Claire J Tomlin. 2014. 'Reachability-based safe learning with Gaussian processes.' In *53rd IEEE Conference on Decision and Control,* 1424–1431. IEEE.

Ames, Aaron D, Samuel Coogan, Magnus Egerstedt, Gennaro Notomista, Koushil Sreenath, and Paulo Tabuada. 2019. 'Control barrier functions: Theory and applications.' In *2019 18th European control conference (ECC),* 3420–3431. IEEE.

Andersson, Pontus, and Erika Franzén. 2015. 'Effects of weight-shift training on walking ability, ambulation, and weight distribution in individuals with chronic stroke: a pilot study.' *Topics in stroke rehabilitation* 22 (6): 437–443.

Bamberg, Stacy J Morris, Ari Y Benbasat, Donna Moxley Scarborough, David E Krebs, and Joseph A Paradiso. 2008. 'Gait analysis using a shoe-integrated wireless sensor system.' *IEEE transactions on information technology in biomedicine* 12 (4): 413–423.

Barrau, Axel, and Silvère Bonnabel. 2016. 'The invariant extended Kalman filter as a stable observer.' *IEEE Transactions on Automatic Control* 62 (4): 1797–1812.

Benjamin, Emelia J, Salim S Virani, Clifton W Callaway, Alanna M Chamberlain, Alexander R Chang, Susan Cheng, Stephanie E Chiuve, Mary Cushman, Francesca N Delling, Rajat Deo, et al. 2018. 'Heart disease and stroke statistics—2018 update: a report from the American Heart Association.' *Circulation* 137 (12): e67–e492.

Berger, Alisa, Fabian Horst, Fabian Steinberg, Fabian Thomas, Claudia Müller-Eising, Wolfgang I Schöllhorn, and Michael Doppelmayr. 2019. 'Increased gait variability during robot-assisted walking is accompanied by increased sensorimotor brain activity in healthy people.' *Journal of neuroengineering and rehabilitation* 16 (1): 1–13.

Brach, Jennifer S, and Jessie M VanSwearingen. 2013. 'Interventions to improve walking in older adults.' *Current translational geriatrics and experimental gerontology reports* 2 (4): 230–238.

Brossard, Martin, Axel Barrau, and Silvère Bonnabel. 2020. 'AI-IMU dead-reckoning.' *IEEE Transactions on Intelligent Vehicles* 5 (4): 585–595.

Brunke, Lukas, Melissa Greeff, Adam W Hall, Zhaocong Yuan, Siqi Zhou, Jacopo Panerati, and Angela P Schoellig. 2022. 'Safe learning in robotics: From learning-based control to safe reinforcement learning.' *Annual Review of Control, Robotics, and Autonomous Systems* 5:411–444.

Bryan, Gwendolyn M, Patrick W Franks, Seungmoon Song, Ricardo Reyes, Meghan P O'Donovan, Karen N Gregorczyk, and Steven H Collins. 2021. 'Optimized hip-knee-ankle exoskeleton assistance reduces the metabolic cost of walking with worn loads.' *Journal of neuroengineering and rehabilitation* 18 (1): 1–13.

Buchli, Jonas, Freek Stulp, Evangelos Theodorou, and Stefan Schaal. 2011. 'Learning variable impedance control.' *International Journal of Robotics Research* 30 (7): 820–833. https://doi.org/10.1177/0278364911402527.

Cai, Lance L, Andy J Fong, Yongqiang Liang, Joel Burdick, and V Reggie Edgerton. 2006. 'Assist-as-needed training paradigms for robotic rehabilitation of spinal cord injuries.' In *Proceedings 2006 IEEE International Conference on Robotics and Automation, 2006. ICRA 2006.* 3504–3511. IEEE.

Chen, Xing, Yuehong Yin, and Yuanjie Fan. 2014. 'EMG oscillator model-based energy kernel method for characterizing muscle intrinsic property under isometric contraction.' *Chinese science bulletin* 59 (14): 1556–1567.

Chen, Xing, Yan Zeng, and Yuehong Yin. 2017. 'Improving the transparency of an exoskeleton knee joint based on the understanding of motor intent using energy kernel method of EMG.' *IEEE Transactions on Neural Systems and Rehabilitation Engineering* 25 (6): 577–588.

Christie, Anita, J Greig Inglis, Gary Kamen, and David A Gabriel. 2009. 'Relationships between surface EMG variables and motor unit firing rates.' *European journal of applied physiology* 107 (2): 177–185.

Ciesla, Nancy, Victor Dinglas, Eddy Fan, Michelle Kho, Jill Kuramoto, and Dale Needham. 2011. 'Manual muscle testing: a method of measuring extremity muscle strength applied to critically ill patients.' *JoVE (Journal of Visualized Experiments),* no. 50, e2632.

Deane, N., Y. Gu, P.-C. Kao, Y.-N. Wu, M. Zielinski, and M. Inalpolat. 2021. 'Pressure monitoring based identification of the EOD suit–human interface load distribution.' *International Journal of Intelligent Robotics and Applications* 5 (1): 410–423.

Deisenroth, Marc, and Carl E Rasmussen. 2011. 'PILCO: A model-based and data-efficient approach to policy search.' In *Proceedings of the 28th International Conference on machine learning (ICML-11),* 465–472.

Duncan, Pamela W, Richard Zorowitz, Barbara Bates, John Y Choi, Jonathan J Glasberg, Glenn D Graham, Richard C Katz, Kerri Lamberty, and Dean Reker. 2005. 'Management of adult stroke rehabilitation care: a clinical practice guideline.' *stroke* 36 (9): e100–e143.

Eilenberg, Michael F, Hartmut Geyer, and Hugh Herr. 2010. 'Control of a powered ankle–foot prosthesis based on a neuromuscular model.' *IEEE transactions on neural systems and rehabilitation engineering* 18 (2): 164–173.

Embry, Kyle R, Dario J Villarreal, Rebecca L Macaluso, and Robert D Gregg. 2018. 'Modeling the Kinematics of Human Locomotion over Continuously Varying Speeds and Inclines.' *IEEE Transactions on Neural Systems and Rehabilitation Engineering.*

Flansbjer, Ulla-Britt, David Downham, and Jan Lexell. 2006. 'Knee muscle strength, gait performance, and perceived participation after stroke.' *Archives of physical medicine and rehabilitation* 87 (7): 974–980.

Fong, Jason, Hossein Rouhani, and Mahdi Tavakoli. 2019. 'A therapist-taught robotic system for assistance during gait therapy targeting foot drop.' *IEEE Robotics and Automation Letters* 4 (2): 407–413.

Galvez, Jose A, Grigor Kerdanyan, Somboon Maneekobkunwong, Roger Weber, Michael Scott, Susan J Harkema, and David J Reinkensmeyer. 2005. 'Measuring human trainers' skill for the design of better robot control algorithms for gait training after spinal cord injury.' In *9th International Conference on Rehabilitation Robotics, 2005. ICORR 2005.* 231–234. IEEE.

Gancet, Jeremi, M Ilzkovitz, G Cheron, Y Ivanenko, H Van Der Kooij, F Van Der Helm, F Zanow, and F Thorsteinsson. 2011. 'MINDWALKER: a brain controlled lower limbs exoskeleton for rehabilitation. Potential applications to space.' In *11th Symposium on advanced space technologies in robotics and automation,* 12–14.

Gao, Y., C. Yuan, and Y. Gu. 2021 (in press). 'Invariant Extended Kalman Filtering for Hybrid Models of Bipedal Robot Walking.' In *Proc. of IFAC Modeling, Estimation and Control Conference.*

Gillen, Glen. 2015. *Stroke rehabilitation: a function-based approach.* Elsevier Health Sciences.

Glackin, Cornelius, Christoph Salge, Martin Greaves, Daniel Polani, Siniša Slavnić, Danijela Ristić-Durrant, Adrian Leu, and Zlatko Matjačić. 2015. 'Gait trajectory prediction using Gaussian process ensembles.' *IEEE-RAS International Conference on Humanoid Robots* 2015-Febru:628–633. https://doi.org/10.1109/HUMANOIDS.2014.7041428.

Goršič, Maja, Roman Kamnik, Luka Ambrožič, Nicola Vitiello, Dirk Lefeber, Guido Pasquini, and Marko Munih. 2014. 'Online phase detection using wearable sensors for walking with a robotic prosthesis.' *Sensors* 14 (2): 2776–2794.

Gregg, Robert D, Tommaso Lenzi, Levi J Hargrove, and Jonathon W Sensinger. 2014. 'Virtual constraint control of a powered prosthetic leg: From simulation to experiments with transfemoral amputees.' *IEEE Transactions on Robotics* 30 (6): 1455–1471.

Gurriet, Thomas, Mark Mote, Andrew Singletary, Petter Nilsson, Eric Feron, and Aaron D Ames. 2020. 'A scalable safety critical control framework for nonlinear systems.' *IEEE Access* 8:187249–187275.

Gurriet, Thomas, Maegan Tucker, Alexis Duburcq, Guilhem Boeris, and Aaron D Ames. 2019. 'Towards variable assistance for lower body exoskeletons.' *IEEE Robotics and Automation Letters* 5 (1): 266–273.

Hartley, Ross, Maani Ghaffari, Ryan M Eustice, and Jessy W Grizzle. 2020. 'Contact-aided invariant extended Kalman filtering for robot state estimation.' *Int. J. Rob. Res.* 39 (4): 402–430.

———. 2019. 'Contact-Aided Invariant Extended Kalman Filtering for Robot State Estimation.' *arXiv e-prints* (April): arXiv:1904.09251. arXiv: 1904.09251 [cs.RO].

Hermens, HJ, and B Freriks. 1997. 'The state of the art on sensors and sensor placement procedures for surface electromyography: a proposal for sensor placement procedures.' *Deliverable of the SENIAM Project.*

Herr, Hugh. 2009. 'Exoskeletons and orthoses: classification, design challenges and future directions.' *Journal of neuroengineering and rehabilitation* 6 (1): 21.

Howe, Roger. 1983. 'Very basic Lie theory.' *The American Mathematical Monthly* 90 (9): 600–623.

Huang, Guoquan P, Anastasios I Mourikis, and Stergios I Roumeliotis. 2010. 'Observability-based rules for designing consistent EKF SLAM estimators.' *The International Journal of Robotics Research* 29 (5): 502–528.

Huang, He, Todd A Kuiken, Robert D Lipschutz, et al. 2009. 'A strategy for identifying locomotion modes using surface electromyography.' *IEEE Transactions on Biomedical Engineering* 56 (1): 65–73.

Islam, Mazharul, and Elizabeth T Hsiao-Wecksler. 2016. 'Detection of gait modes using an artificial neural network during walking with a powered ankle-foot orthosis.' *Journal of Biophysics* 2016.

Ivanenko, Yuri P, Richard E Poppele, and Francesco Lacquaniti. 2004. 'Five basic muscle activation patterns account for muscle activity during human locomotion.' *The Journal of physiology* 556 (1): 267–282.

Jaffer, Hayder, Viola B Morris, Desiree Stewart, and Vinod Labhasetwar. 2011. 'Advances in stroke therapy.' *Drug delivery and translational research* 1 (6): 409–419.

Jin, Dewen, Jiankun Yang, Ruihong Zhang, Rencheng Wang, and Jichuan Zhang. 2006. 'Terrain identification for prosthetic knees based on electromyographic signal features.' *Tsinghua Science and Technology* 11 (1): 74–79.

Joshi, Deepak, Bryson H Nakamura, and Michael E Hahn. 2015. 'High energy spectrogram with integrated prior knowledge for EMG-based locomotion classification.' *Medical engineering & physics* 37 (5): 518–524.

Karavas, Nikos, Arash Ajoudani, Nikos Tsagarakis, Jody Saglia, Antonio Bicchi, and Darwin Caldwell. 2015. 'Tele-impedance based assistive control for a compliant knee exoskeleton.' *Robotics and Autonomous Systems* 73:78–90.

Kelly-Hayes, Margaret, Alexa Beiser, Carlos S Kase, Amy Scaramucci, Ralph B D'Agostino, and Philip A Wolf. 2003. 'The influence of gender and age on disability following ischemic stroke: the Framingham study.' *Journal of Stroke and Cerebrovascular Diseases* 12 (3): 119–126.

Khan, S. G., M. Tufail, S. H. Shah, and I. Ullah. 2019. 'Real-Time Impedance Control Based on Learned Inverse Dynamics.' *Advanced Robotics* 33 (24): 1281–1292. https://doi.org/10.1080/01691864.2019.1690574.

Kilicarslan, Atilla, Saurabh Prasad, Robert G Grossman, and Jose L Contreras-Vidal. 2013. 'High accuracy decoding of user intentions using EEG to control a lower-body exoskeleton.' In *2013 35th annual international conference of the IEEE Engineering in Medicine and Biology Society (EMBC),* 5606–5609. IEEE.

Kim, Kanghyun, Sungwon Shin, and Kyoungchul Kong. 2018. 'An air-filled pad with elastomeric pillar array designed for a force-sensing insole.' *IEEE Sensors Journal* 18 (10): 3968–3976.

Kong, Kyoungchul, and Masayoshi Tomizuka. 2009. 'A gait monitoring system based on air pressure sensors embedded in a shoe.' *IEEE/ASME Transactions on mechatronics* 14 (3): 358–370.

Kuo, Arthur D. 2007. 'The six determinants of gait and the inverted pendulum analogy: A dynamic walking perspective.' *Human movement science* 26 (4): 617–656.

Laparidou, Despina, Ffion Curtis, Joseph Akanuwe, Khaled Goher, A Niroshan Siriwardena, and Ayse Kucukyilmaz. 2021. 'Patient, carer, and staff perceptions of robotics in motor rehabilitation: a systematic review and qualitative meta-synthesis.' *Journal of neuroengineering and rehabilitation* 18 (1): 1–24.

Lauziere, Selena, Martina Betschart, Rachid Aissaoui, and Sylvie Nadeau. 2014. 'Understanding spatial and temporal gait asymmetries in individuals post stroke.' *Int J Phys Med Rehabil* 2 (3): 201.

Lazaro, Rolando T, Sandra G Reina-Guerra, and Myla Quiben. 2019. *Umphred's Neurological Rehabilitation-E-Book.* Elsevier Health Sciences.

Lee, Suwoong, and Yoshiyuki Sankai. 2002. 'Power assist control for walking aid with HAL-3 based on EMG and impedance adjustment around knee joint.' In *Intelligent Robots and Systems, 2002. IEEE/RSJ International Conference on,* 2:1499–1504. IEEE.

Lencioni, Tiziana, Ilaria Carpinella, Marco Rabuffetti, Alberto Marzegan, and Maurizio Ferrarin. 2019. 'Human kinematic, kinetic and EMG data during different walking and stair ascending and descending tasks.' *Scientific data* 6 (1): 309.

Lennon, Sheila. 2001. 'Gait re-education based on the Bobath concept in two patients with hemiplegia following stroke.' *Physical therapy* 81 (3): 924–935.

Li, Sheng, Gerard E Francisco, and Ping Zhou. 2018. 'Post-stroke hemiplegic gait: new perspective and insights.' *Frontiers in physiology* 9:1021.

Li, Yifan David, and Elizabeth T Hsiao-Wecksler. 2013. 'Gait mode recognition and control for a portable-powered ankle-foot orthosis.' In *2013 IEEE 13th International Conference on Rehabilitation Robotics (ICORR),* 1–8. IEEE.

Lin, Tzu-Yuan, Ray Zhang, Justin Yu, and Maani Ghaffari. 2021. 'Deep Multi-Modal Contact Estimation for Invariant Observer Design on Quadruped Robots.' *arXiv preprint arXiv:2106.15713.*

Liu, Tao, Yoshio Inoue, Kyoko Shibata, and K Shiojima. 2011. 'A mobile force plate and three-dimensional motion analysis system for three-dimensional gait assessment.' *IEEE Sensors Journal* 12 (5): 1461–1467.

Lv, Ge. 2018. 'Energy Shaping Control of Powered Lower-Limb Exoskeletons for Assistance of Human Locomotion.' PhD diss.

Maciejasz, Paweł, Jörg Eschweiler, Kurt Gerlach-Hahn, Arne Jansen-Troy, and Steffen Leonhardt. 2014. 'A survey on robotic devices for upper limb rehabilitation.' *Journal of neuroengineering and rehabilitation* 11 (1): 1–29.

Marchal-Crespo, Laura, and David J Reinkensmeyer. 2009. 'Review of control strategies for robotic movement training after neurologic injury.' *Journal of neuroengineering and rehabilitation* 6 (1): 1–15.

Mauritz, K-H. 2002. 'Gait training in hemiplegia.' *European journal of Neurology* 9:23–29.

Maybeck, Peter S. 1982. *Stochastic models, estimation, and control.* Academic press.

Md Alias, MF, Ashwin Needham, Abbas A Dehghani-Sanij, Ravi Vaidyanathan, Uriel Martinez-Hernandez, and Charles Weston. 2018. 'Walking Activity Recognition with sEMG Sensor Array on Thigh Circumference using Convolutional Neural Network.' In *2018 International Conference on Intelligent Systems Engineering (ICISE).* IEEE.

Merlo, Andrea, Dario Farina, and Roberto Merletti. 2003. 'A fast and reliable technique for muscle activity detection from surface EMG signals.' *IEEE Transactions on Biomedical Engineering* 50 (3): 316–323.

O'Connor, Joanne, Dorothy McCaughan, Catriona McDaid, Alison Booth, Debra Fayter, Roccio Rodriguez-Lopez, Roy Bowers, Lisa Dyson, Cynthia Paola Iglesias Urrutia, Simon Lalor, et al. 2016. 'Orthotic management of instability of the knee related to neuromuscular and central nervous system disorders: systematic review,

qualitative study, survey and costing analysis.' *Health technology assessment,* 1–262.

Ojeda, L., and J. Borenstein. 2007. 'Personal dead-reckoning system for GPS-denied environments.' In *2007 IEEE International Workshop on Safety, Security and Rescue Robotics,* 1–6.

Paliwal, Kuldip K, Anant Agarwal, and Sarvajit S Sinha. 1982. 'A modification over Sakoe and Chiba's dynamic time warping algorithm for isolated word recognition.' *Signal Processing* 4 (4): 329–333.

Perry, Jacquelin, Jon R Davids, et al. 1992. 'Gait analysis: normal and pathological function.' *Journal of Pediatric Orthopaedics* 12 (6): 815.

Perry, Milly. 2015. 'Science and Innovation Strategic Policy Plans for the 2020s (EU, AU, UK): Will They Prepare Us for the World in 2050?' *Applied Economics and Finance* 2 (3): 76–84.

Potokar, E., K. Norman, and J. Mangelson. 2021. 'Invariant Extended Kalman Filtering for Underwater Navigation.' *IEEE Robotics and Automation Letters* 6 (3): 5792–5799.

Rodrıguez-Fernández, Antonio, Joan Lobo-Prat, and Josep M Font-Llagunes. 2021. 'Systematic review on wearable lower-limb exoskeletons for gait training in neuromuscular impairments.' *Journal of neuroengineering and rehabilitation* 18 (1): 1–21.

Rouse, Elliott J, Luke M Mooney, and Hugh M Herr. 2014. 'Clutchable series-elastic actuator: Implications for prosthetic knee design.' *The International Journal of Robotics Research* 33 (13): 1611–1625.

Rozo, Leonel, Sylvain Calinon, Darwin G. Caldwell, Pablo Jiménez, and Carme Torras. 2016. 'Learning Physical Collaborative Robot Behaviors From Human Demonstrations.' *IEEE Transactions on Robotics* 32 (3): 513–527. https://doi.org/10.1109/TRO.2016.2540623.

Ruiz, A. R. J., F. S. Granja, J. C. P. Honorato, and J. I. G. Rosas. 2011. 'Accurate pedestrian indoor navigation by tightly coupling foot-mounted IMU and RFID measurements.' *IEEE Transactions on Instrumentation and Measurement* 61 (1): 178–189.

Sawers, Andrew, and Lena H Ting. 2014. 'Perspectives on human-human sensorimotor interactions for the design of rehabilitation robots.' *Journal of neuroengineering and rehabilitation* 11 (1): 142.

Slade, Patrick, Mykel J Kochenderfer, Scott L Delp, and Steven H Collins. 2022. 'Personalizing exoskeleton assistance while walking in the real world.' *Nature* 610 (7931): 277–282.

Sola, Joan, Jeremie Deray, and Dinesh Atchuthan. 2018. 'A micro Lie theory for state estimation in robotics.' *arXiv preprint arXiv:1812.01537.*

Sup, Frank, Huseyin Atakan Varol, and Michael Goldfarb. 2010. 'Upslope walking with a powered knee and ankle prosthesis: initial results with an amputee subject.' *IEEE transactions on neural systems and rehabilitation engineering* 19 (1): 71–78.

Teng, S., M. W. Mueller, and K. Sreenath. 2021. 'Legged Robot State Estimation in Slippery Environments Using Invariant Extended Kalman Filter with Velocity Update.' *arXiv preprint arXiv:2104.04238.*

Tucker, Maegan, Kejun Li, and Aaron D Ames. 2023. 'Synthesizing Robust Walking Gaits via Discrete-Time Barrier Functions with Application to Multi-Contact Exoskeleton Locomotion.' *arXiv preprint arXiv:2310.06169.*

Tucker, Michael R, Jeremy Olivier, Anna Pagel, Hannes Bleuler, Mohamed Bouri, Olivier Lambercy, José del R Millán, Robert Riener, Heike Vallery, and Roger Gassert. 2015. 'Control strategies for active lower extremity prosthetics and orthotics: a review.' *Journal of neuroengineering and rehabilitation* 12 (1): 1–30.

Van Nguyen, L., and H. M. La. 2016. 'Real-time human foot motion localization algorithm with dynamic speed.' *IEEE Transactions on Human-Machine Systems* 46 (6): 822–833.

Xi, Xugang, Minyan Tang, Seyed M Miran, and Zhizeng Luo. 2017. 'Evaluation of feature extraction and recognition for activity monitoring and fall detection based on wearable sEMG sensors.' *Sensors* 17 (6): 1229.

Young, Aaron J, and Daniel P Ferris. 2017. 'State of the art and future directions for lower limb robotic exoskeletons.' *IEEE Transactions on Neural Systems and Rehabilitation Engineering* 25 (2): 171–182.

Yuan, Q., and I.-M. Chen. 2013. '3-D localization of human based on an inertial capture system.' *IEEE Transactions on Robotics* 29 (3): 806–812.

Yuan, Q., and I.-M. Chen. 2014. 'Localization and velocity tracking of human via 3 IMU sensors.' *Sensors and Actuators A: Physical* 212:25–33.

Zanatta, Francesco, Anna Giardini, Antonia Pierobon, Marco D'Addario, and Patrizia Steca. 2022. 'A systematic review on the usability of robotic and virtual reality devices in neuromotor rehabilitation: patients' and healthcare professionals' perspective.' *BMC health services research* 22 (1): 523.

Zhang, Juanjuan, Pieter Fiers, Kirby A Witte, Rachel W Jackson, Katherine L Poggensee, Christopher G Atkeson, and Steven H Collins. 2017. 'Human-in-the-loop optimization of exoskeleton assistance during walking.' *Science* 356 (6344): 1280–1284.

Zhang, Qiang, Varun Nalam, Xikai Tu, Minhan Li, Jennie Si, Michael D Lewek, and He Helen Huang. 2022. 'Imposing Healthy Hip Motion Pattern and Range by Exoskeleton Control for Individualized Assistance.' *IEEE Robotics and Automation Letters* 7 (4): 11126–11133.

Zhang, Wenlong, Masayoshi Tomizuka, and Nancy Byl. 2016. 'A wireless human motion monitoring system for smart rehabilitation.' *Journal of Dynamic Systems, Measurement, and Control* 138 (11): 111004.

Zhang, Y., K. Chen, and J. Yi. 2013. 'Rider trunk and bicycle pose estimation with fusion of force/inertial sensors.' *IEEE Transactions on Biomedical Engineering* 60 (9): 2541–2551.

Zhang, Y., K. Chen, J. Yi, T. Liu, and Q. Pan. 2015. 'Whole-body pose estimation in human bicycle riding using a small set of wearable sensors.' *IEEE/ASME Transactions on Mechatronics* 21 (1): 163–174.

Ziegier, Jakob, Hubert Gattringer, and Andreas Mueller. 2018. 'Classification of Gait Phases Based on Bilateral EMG Data Using Support Vector Machines.' In *2018 7th IEEE International Conference on Biomedical Robotics and Biomechatronics (Biorob),* 978–983. IEEE.

Zihajehzadeh, Shaghayegh, and Edward J Park. 2016. 'Regression model-based walking speed estimation using wrist-worn inertial sensor.' *PloS one* 11 (10): e0165211.

APPENDIX A

STATEMENT FOR AUTHORSHIP

This is to certify that all co-authors have granted their permission to include the collaborative works in this thesis.

APPENDIX B

SUPPLEMENTARY MATERIALS FOR INEKF DESIGN AND OBSERVABILITY ANALYSIS

The Lie group G introduced in chapter 4 is a combination of an extended $SE(3)$ (group of double direct spatial isometrie $SE_2(3)$ Barrau and Bonnabel 2016) and another $SE(3)$. It is clear that G is a set of $m \times m$ invertible square matrices. Yet, for G to be a valid matrix Lie group, it should also possess the following three properties: $\forall X \in G, \mathbf{X}^{-1} \in G$; $\forall \mathbf{X}_1, \mathbf{X}_2 \in G, \mathbf{X}_1\mathbf{X}_2 \in G$; and $\mathbf{E} \in G$.

Given the definition of $\mathbf{X}$ in (4.8), we have:

$$\mathbf{X}^{-1} = \begin{bmatrix} \mathbf{R}^T & -\mathbf{R}^T\mathbf{v} & -\mathbf{R}^T\mathbf{p} & \mathbf{0}_{3,3} & \mathbf{0}_{3,1} \\ \mathbf{0}_{1,3} & 1 & 0 & \mathbf{0}_{1,3} & \mathbf{0}_{3,1} \\ \mathbf{0}_{1,3} & 0 & 1 & \mathbf{0}_{1,3} & \mathbf{0}_{3,1} \\ \mathbf{0}_{3,3} & \mathbf{0}_{3,3} & \mathbf{0}_{3,3} & \Delta\mathbf{R}^T & -\Delta\mathbf{R}^T\Delta\mathbf{p} \\ \mathbf{0}_{1,3} & 0 & 0 & \mathbf{0}_{1,3} & 1 \end{bmatrix};$$

$$\mathbf{X}_1\mathbf{X}_2 = \begin{bmatrix} \mathbf{R}_1\mathbf{R}_2 & \mathbf{R}_1\mathbf{v}_2 + \mathbf{v}_1 & \mathbf{R}_1\mathbf{p}_2 + \mathbf{p}_1 & \mathbf{0}_{3,3} & \mathbf{0}_{3,1} \\ \mathbf{0}_{1,3} & 1 & 0 & \mathbf{0}_{1,3} & \mathbf{0}_{3,1} \\ \mathbf{0}_{1,3} & 0 & 1 & \mathbf{0}_{1,3} & \mathbf{0}_{3,1} \\ \mathbf{0}_{3,3} & \mathbf{0}_{3,3} & \mathbf{0}_{3,3} & \Delta\mathbf{R}_1\Delta\mathbf{R}_2 & \Delta\mathbf{R}_1\Delta\mathbf{p}_2 + \Delta\mathbf{p}_1 \\ \mathbf{0}_{1,3} & 0 & 0 & \mathbf{0}_{1,3} & 1 \end{bmatrix}$$

Then, it is trivial to see that $\mathbf{X}^{-1} \in G$ and $\mathbf{X}_1\mathbf{X}_2 \in G$. It is also trivial to see that $\mathbf{E} = \mathbf{X}\mathbf{X}^{-1} = \mathbf{I}_9 \in G$.

Group Affine Property of f_{u_t}: We need to show that $f_{u_t}(\mathbf{X})$ defined in (6.1) has the group affine property in (4.13). Here we show the expressions of $f_{u_t}(\mathbf{X}_1)$, $f_{u_t}(\mathbf{X}_1\mathbf{X}_2)$, and $f_{u_t}(\mathbf{E})$, which are used to define the property in (4.13) ($\mathbf{X}_1, \mathbf{X}_2 \in G$):

$$f_{u_t}(\mathbf{X}_1) = \begin{bmatrix} \mathbf{R}_1(\tilde{\boldsymbol{\omega}})_\times & \mathbf{R}_1\tilde{\mathbf{a}} + \mathbf{g} & \mathbf{v}_1 & \mathbf{0}_{3,4} \\ \mathbf{0}_{6,3} & \mathbf{0}_{6,1} & \mathbf{0}_{6,1} & \mathbf{0}_{6,4} \end{bmatrix};$$

$$f_{u_t}(\mathbf{X}_1\mathbf{X}_2) = \begin{bmatrix} \mathbf{R}_1\mathbf{R}_2(\tilde{\boldsymbol{\omega}})_\times & \mathbf{R}_1\mathbf{R}_2\tilde{\mathbf{a}} + \mathbf{g} & \mathbf{R}_1\mathbf{v}_2 + \mathbf{v}_1 & \mathbf{0}_{3,4} \\ \mathbf{0}_{6,3} & \mathbf{0}_{6,1} & \mathbf{0}_{6,1} & \mathbf{0}_{6,4} \end{bmatrix};$$

$$f_{ut}(\mathbf{E}) = \begin{bmatrix} (\tilde{\boldsymbol{\omega}})_\times & \tilde{\mathbf{a}} + \mathbf{g} & \mathbf{0}_{3,1} & \mathbf{0}_{3,4} \\ \mathbf{0}_{6,3} & \mathbf{0}_{6,1} & \mathbf{0}_{6,1} & \mathbf{0}_{6,4} \end{bmatrix}.$$

Using these matrices and basic matrix operation, it is trivial to see the group affine property holds for $f_{u_t}(.)$.

Discrete Filter Propagation Equations: As discussed in Sec.4.1.3, the propagation equations in discrete time are obtained via Euler integration from t_k to t_{k+1} ($\Delta t = t_{k+1} - t_k$):

$$\bar{\mathbf{R}}_{k+1}^- = \bar{\mathbf{R}}_k^+ \exp(\tilde{\boldsymbol{\omega}}_k \Delta t), \quad \bar{\mathbf{v}}_{k+1}^- = \bar{\mathbf{v}}_k^+ + \bar{\mathbf{R}}_k^+ \exp(\tilde{\mathbf{a}}_k \Delta t) + \mathbf{g}\Delta t,$$

$$\bar{\mathbf{p}}_{k+1}^- = \bar{\mathbf{p}}_k^+ + \bar{\mathbf{v}}_k^+ \Delta t + \frac{1}{2}\bar{\mathbf{R}}_k^+ \exp(\tilde{\mathbf{a}}_k \Delta t^2) + \frac{1}{2}\mathbf{g}\Delta t^2,$$

$$\Delta\bar{\mathbf{R}}_{k+1}^- = \Delta\bar{\mathbf{R}}_k^+, \quad \overline{\Delta\mathbf{p}}_{k+1}^- = \overline{\Delta\mathbf{p}}_k^+.$$

Given the system discrete state transition matrix $\mathbf{\Phi}_k$, we can write down the discrete covariance propagation:

$$\mathbf{P}_{k+1} = \mathbf{\Phi}_k \mathbf{P}_k \mathbf{\Phi}_k^T + \bar{\mathbf{Q}}_k, \quad \bar{\mathbf{Q}}_k \approx \mathbf{\Phi}_k \bar{\mathbf{Q}}_k \mathbf{\Phi}_k^T \Delta t,$$

where $\mathbf{Q}_k$ comes from Sec. (4.1.3). More details on the system discretization can be found at Hartley et al. 2019.

Observability of $\Delta\mathbf{p}$ and $\Delta\mathbf{R}$: Here we can show that if direction of $\boldsymbol{\omega}$ remains constant, then the block matrix in $\mathbf{O}$ corresponding to observability of $\Delta\mathbf{p}$ (we denote it as $\mathbf{O}_{\Delta p}$) will lose one column rank. Let us assume $\boldsymbol{\omega}_k = \| \boldsymbol{\omega}_k \| \mathbf{b}$, where $\mathbf{b} \in \mathbb{R}^3$ is a constant unit vector. Knowing that $\Delta\mathbf{R}$ is constant, then according to (4.28) we have:

$$\mathbf{O}_{\Delta p} = \begin{bmatrix} (\Delta\bar{\mathbf{R}}_k \boldsymbol{\omega}_k)_\times \\ (\Delta\bar{\mathbf{R}}_{k+1} \boldsymbol{\omega}_{k+1})_\times \\ \vdots \\ (\Delta\bar{\mathbf{R}}_{k+4} \boldsymbol{\omega}_{k+4})_\times \end{bmatrix} = \begin{bmatrix} \| \boldsymbol{\omega}_k \| (\Delta\bar{\mathbf{R}}_k)_\times \\ \| \boldsymbol{\omega}_{k+1} \| (\Delta\bar{\mathbf{R}}_k)_\times \\ \vdots \\ \| \boldsymbol{\omega}_{k+4} \| (\Delta\bar{\mathbf{R}}_k)_\times \end{bmatrix}$$

Knowing that $\| (\Delta\bar{\mathbf{R}}_k b)_\times$ has column rank two (property of any 3×3 skew-symmetric matrix), it is trivial to see that the whole $\mathbf{O}_{\Delta p}$ has column rank 2. If $\mathbf{b}$ is time-varying however, $\mathbf{O}_{\Delta p}$ will have full column rank.

For $\Delta\mathbf{R}$, the observability also depends on the measured contact point movement ($FK(\boldsymbol{\alpha})$) and the linear IMU velocity $\mathbf{v}$, and therefore it could still be fully observable if those parameters have time-varying directions.

APPENDIX C

ASU IRB APPROVAL

APPROVAL: EXPEDITED REVIEW

Wenlong Zhang
IAFSE-PS: Polytechnic Engineering Programs (EGR)
-
Wenlong.Zhang@asu.edu

Dear Wenlong Zhang:

On 1/1/2020 the ASU IRB reviewed the following protocol:

Type of Review:	Initial Study
Title:	Communication through Interaction: Intent Inference and Signaling to Facilitate Human Learning in Assistive Robots
Investigator:	Wenlong Zhang
IRB ID:	STUDY00011266
Category of review:	
Funding:	Name: National Science Foundation (NSF), Grant Office ID: FP00020725, Funding Source ID: 1944833
Grant Title:	FP00020725;
Grant ID:	FP00020725;
Documents Reviewed:	• FP20725-Zhang-FP.pdf, Category: Sponsor Attachment; • Protocol_pHRI.docx, Category: IRB Protocol; • Recruitment flyer_pHRI.pdf, Category: Recruitment Materials; • short-consent_pHRI.pdf, Category: Consent Form;

The IRB approved the protocol from 1/1/2020 to 12/31/2020 inclusive. Three weeks before 12/31/2020 you are to submit a completed Continuing Review application and required attachments to request continuing approval or closure.

If continuing review approval is not granted before the expiration date of 12/31/2020 approval of this protocol expires on that date. When consent is appropriate, you must use final, watermarked versions available under the “Documents” tab in ERA-IRB.

In conducting this protocol you are required to follow the requirements listed in the INVESTIGATOR MANUAL (HRP-103).

Sincerely,

IRB Administrator

cc:
Emiliano Quinones Yumbla
Seyed Mostafa Rezayat Sorkhabadi
Wenlong Zhang